

**The Venus plasma environment:
a comparison of Venus Express
ASPERA-4 measurements with
3D hybrid simulations**

Von der Fakultät für Elektrotechnik, Informationstechnik, Physik
der Technischen Universität Carolo-Wilhelmina
zu Braunschweig
zur Erlangung des Grades einer
Doktorin der Naturwissenschaften
(Dr.rer.nat.)
genehmigte
Dissertation

von Cornelia Martinecz
aus Bad Radkersburg, Österreich

Bibliografische Information Der Deutschen Bibliothek

Die Deutsche Bibliothek verzeichnet diese Publikation in der Deutschen Nationalbibliografie; detaillierte bibliografische Daten sind im Internet über <http://dnb.ddb.de> abrufbar.

1. Referentin oder Referent: Prof. Dr. Uwe Motschmann
 2. Referentin oder Referent: Prof. Dr. Eckart Marsch
- eingereicht am: 2. Oktober 2008
mündliche Prüfung (Disputation) am: 26. November 2008

ISBN 978-3-936586-90-9

Cover Image: ESA

Copernicus Publications 2008

<http://publications.copernicus.org>

© Cornelia Martinecz

Printed in Germany

Vorveröffentlichungen aus der Dissertation

Teilergebnisse aus dieser Arbeit wurden mit Genehmigung der Fakultät für Elektrotechnik, Informationstechnik, Physik, vertreten durch den Mentor oder den Betreuer der Arbeit, in folgenden Beiträgen vorab veröffentlicht:

Publikationen

C. Martinecz, M. Fränz, J. Woch, N. Krupp, E. Roussos, E. Dubinin, U. Motschmann, S. Barabash, R. Lundin, M. Holmström, H. Andersson, M. Yamauchi, A. Grigoriev, Y. Futana, K. Brinkfeldt, H. Gunell, R. A. Frahm, J. D. Wittingham, J. R. Sharber, J. Scherrer, A. J. Coates, D. R. Linder, D. O. Kataria, E. Kallio, T. Sales, W. Schmidt, P. Riihela, H. E. J. Koskinen, J. U. Kozyra, J. Luhmann, C. T. Russell, E. C. Roelof, P. Brandt, C. C. Curtis, K. C. Hsieh, B. R. Sandel, M. Grande, J.-A. Sauvaud, A. Fedorov, J.-J. Thocaven, C. Mazelle, S. McKenna-Lawler, S. Orsini, R. Cerulli-Irelli, M. Maggi, A. Mura, A. Milillo, P. Wurz, A. Galli, P. Bochslers, K. Asamura, K. Szego, W. Baumjohann, T. L. Zhang, H. Lammer, 2008, Venus bow shock and ion composition boundary located by Venus Express ASPERA-4, *Planet. Space Sci.*, 56, 780-784, doi:10.1016/j.pss.2007.01.014

C. Martinecz, A. Bößwetter, M. Fränz, E. Roussos, J. Woch, N. Krupp, E. Dubinin, U. Motschmann, S. Wiehle, S. Simon, S. Barabash, R. Lundin, T. L. Zhang, H. Lammer, H. Lichtenegger, and Y. Kulikov, 2008, The plasma environment of Venus: comparison of Venus Express ASPERA-4 measurements with 3D hybrid simulations, *J. Geophys. Res.*, submitted

Tagungsbeiträge

C. Martinecz, M. Fränz, J. Woch, E. Roussos, E. Dubinin and the ASPERA-4 team, Plasma boundaries at Mars and Venus, Kiruna Mars Workshop: Solar wind interaction and atmospheric evolution, Swedish Institute for Space Physics (IRF), Kiruna, Sweden, February 27 - March 1, 2006. (Poster).

C. Martinecz, Comparison of the ionosphere of Mars and Venus, Europlanet Personnel Exchange Program, Swedish Institute for Space Physics (IRF), Kiruna, Sweden, August 20-26, 2006.

C. Martinecz, M. Fränz, J. Woch, N. Krupp, E. Roussos, E. Dubinin, U. Motschmann, S. Barabash, R. Lundin and the ASPERA-4 Team, Plasma boundaries around Venus, European Planetary Science Congress (EPSC), Berlin, Germany, September 18-22, 2006. (Vortrag).

C. Martinecz, M. Fränz, J. Woch, N. Krupp, E. Roussos, E. Dubinin, U. Motschmann, S. Barabash, R. Lundin and the ASPERA-4 Team, Bow Shock and Ion Composition Boundary fits at Venus, 15th ASPERA-3 and 5th ASPERA -4 project meeting, Swedish Institute for Space Physics (IRF), Kiruna, Sweden, October 8-10, 2006. (Vortrag).

C. Martinecz, Solar wind interactions with magnetized and unmagnetized bodies, Solar System Seminar, Max Planck Institute for Solar System Research (MPS), Katlenburg-Lindau, Germany, November 15, 2006. (Vortrag).

C. Martinecz, M. Fränz, J. Woch, N. Krupp, E. Roussos, E. Dubinin, U. Motschmann, S. Barabash, R. Lundin and the ASPERA-4 Team, Location of the bow shock and the ion composition boundary at Venus - initial determinations from Venus Express ASPERA-4, Venus Express Workshop, La Thuile, Italy, March 18-24, 2007. (Vortrag).

C. Martinecz, M. Fränz, J. Woch, N. Krupp, E. Roussos, E. Dubinin, U. Motschmann, A. Bößwetter, S. Simon, S. Barabash, R. Lundin and the ASPERA-4 Team, Location of the bow shock and the ion composition boundary at Venus and initial 3D hybrid simulation results of the plasma environment of Venus, European Geosciences Union (EGU) General Assembly 2007, Vienna, Austria, April 15-20, 2007. (Poster).

C. Martinecz, M. Fränz, J. Woch, N. Krupp, E. Roussos, E. Dubinin, U. Motschmann, S. Barabash, R. Lundin and the ASPERA-4 Team, Location of the bow shock and the ion composition boundary at Venus - initial determinations from Venus Express ASPERA-4, 16th ASPERA-3 and 6th ASPERA-4 project meeting, Stockholm, Sweden, May 9-11, 2007. (Vortrag).

C. Martinecz, M. Fränz, J. Woch, N. Krupp, E. Roussos, E. Dubinin, U. Motschmann, A. Bößwetter, S. Simon, S. Barabash, R. Lundin and the ASPERA-4 Team, The plasma environment of Venus: comparison of Venus Express ASPERA-4 measurements with 3D hybrid simulations, European Planetary Science Congress (EPSC), Potsdam, Germany, August 20-24, 2007. (Poster).

C. Martinecz, M. Fränz, J. Woch, N. Krupp, E. Roussos, E. Dubinin, U. Motschmann, A. Bößwetter, S. Simon, S. Barabash, R. Lundin and the ASPERA-4 Team, The plasma environment of Venus: a 3D simulation study, Solar System Seminar, Max Planck Institute for Solar System Research (MPS), Katlenburg-Lindau, Germany, November 28, 2007. (Vortrag).

C. Martinecz, M. Fränz, J. Woch, N. Krupp, E. Roussos, E. Dubinin, U. Motschmann, A. Bößwetter, S. Simon, S. Barabash, R. Lundin and the ASPERA-4 Team, Plasma environment of Venus: a 3D simulation study, American Geophysical Union (AGU) Fall Meeting, San Francisco, USA, December 10-14, 2007. (Poster)

C. Martinecz, M. Fränz, J. Woch, N. Krupp, E. Roussos, E. Dubinin, U. Motschmann, A. Bößwetter, S. Simon, S. Barabash, R. Lundin and the ASPERA-4 Team, The plasma environment of Venus: direct comparison of ASPERA-4 measurements with simulation studies, Oberseminar, Institute of Theoretical Physics, Technical University of Braunschweig, Braunschweig, Germany, January 24, 2008. (Vortrag).

C. Martinecz, A. Bößwetter, M. Fränz, E. Roussos, J. Woch, N. Krupp, E. Dubinin, U. Motschmann, S. Wiehle, S. Simon, S. Barabash, R. Lundin, T. L. Zhang, H. Lammer, H.

Lichtenegger and Y. Kulikov, The plasma environment of Venus: comparison of Venus Express ASPERA-4 measurements with 3D hybrid simulations, European Geosciences Union (EGU) General Assembly 2008, Vienna, Austria, April 13-18, 2008. (Poster).

Contents

Abstract	11
1 Introduction	13
1.1 The Planet Venus	15
1.1.1 General properties	15
1.1.2 The interior	17
1.1.3 The lack of a magnetic field	17
1.1.4 The surface	19
1.1.5 The atmosphere and its evolution	20
1.1.6 Ionosphere	24
1.1.7 Escape of atoms and ions	25
1.1.8 What are the similarities and differences between Venus and Earth?	26
1.1.9 Replace Venus with an Earth-like planet – what happens?	27
1.2 Types of plasma interaction with magnetized and unmagnetized bodies	27
1.2.1 Earth’s Moon	28
1.2.2 Earth	29
1.2.3 Mercury	30
1.2.4 Venus	31
1.3 Observational history	33
1.4 Venus Express mission	36
1.5 Motivation and open questions	39
2 Method	41
2.1 The ASPERA-4 instrument	41
2.1.1 Electron Spectrometer (ELS)	43
2.1.2 Ion Mass Analyser (IMA)	44
2.2 Simulation code	45
2.2.1 Basic equations	46
2.2.2 Basic scheme	47
2.2.3 Curvilinear Grid	47
2.2.4 Boundary conditions	49
2.2.5 Simulation geometry	50
2.2.6 Modeling the atmosphere of Venus	52

3	Results	55
3.1	Location of Plasma Boundaries	55
3.1.1	VSO coordinate system	56
3.1.2	Observations	58
3.1.3	Plasma boundary fits	60
3.1.3.1	Solar wind dynamic pressure vs. terminator shock distance	62
3.1.3.2	Solar EUV flux vs. terminator shock distance	63
3.1.4	Influence of data accuracy on the boundary determinations	64
3.1.5	Discussion and Conclusions	64
3.2	Hybrid Simulations	67
3.2.1	Simulation results for low and high solar activity	69
3.2.1.1	Run 1: VEX orbit 85 – Polar angle = 90	69
3.2.1.2	Run 2: VEX orbit 85 – Polar angle \neq 90	76
3.2.2	Comparison of simulation results: solar minimum (Run 1) vs. solar maximum (Run 3)	81
4	Comparison of observations and simulations	89
4.1	VEX orbit 85 vs. Run 1	89
4.2	VEX orbit 85 vs. Run 2	98
4.3	Critical review of the accuracy of the observational parameters	104
4.4	Atmospheric escape rates for oxygen	104
5	Summary and conclusions	109
	Outlook	113
	Bibliography	115
	Acknowledgements	121
	Curriculum Vitae	123

List of Figures

1.1	Divine personification of the planet Venus in the ancient world.	13
1.2	Venus as a subject in classical and prehistoric art.	14
1.3	A cutaway of the six regions of the Earth - the core, mantle, crust, hydro- sphere, atmosphere and magnetosphere.	18
1.4	A cutaway view of a possible internal structure of Venus.	19
1.5	Map of Venus obtained by Magellan illustrating its topography.	20
1.6	The temperature gradients of the Earth's and Venusian atmosphere.	23
1.7	The solar wind - atmosphere interaction at Venus.	26
1.8	Different types of solar wind interactions in our solar system.	28
1.9	Schematics of the solar wind interaction with Earth's moon.	28
1.10	The global structure of the Earth's magnetosphere.	29
1.11	The formation of an induced magnetosphere of an unmagnetized planet.	31
1.12	Schematic of the magnetosheath and magnetic barrier of Venus.	32
1.13	Overview of spacecraft missions to the planet Venus.	33
1.14	Venus Express orbit around Venus and its different observation modes.	37
1.15	The locations of the seven scientific instruments on the Venus Express spacecraft.	37
2.1	The accomodation of the Main Unit and Ion Mass Analyser on the space- craft.	42
2.2	The overall configuration of the ASPERA-4 experiment.	43
2.3	A cross section of the Electron Spectrometer.	44
2.4	A cross section of the Ion Mass Analyser and magnetic separator.	45
2.5	Sketch of the Particle-in-cell method.	48
2.6	The basic steps of each computational cycle.	48
2.7	The curvilinear simulation grid.	49
2.8	Cross sections of the simulation box.	51
2.9	The simulation coordinate system in comparison with the Venus-Sun- Orbit coordinate system.	51
2.10	Cold O and hot O* number densities at solar minimum as a function of altitude.	53
2.11	The neutral number density and ion production rates of oxygen as a func- tion of altitude at solar minimum.	54
3.1	A typical 24h-orbit of Venus Express.	57
3.2	ASPERA-4 data recorded on July 15, 2006.	59

3.3	The plasma boundary fits determined from ASPERA-4 observations. . . .	61
3.4	The terminator shock distance as a function of the ram pressure.	62
3.5	The terminator shock distance as a function of the solar EUV flux.	63
3.6	The VEX bow shock fit in comparison with other shock models based on different data sets at solar minimum.	65
3.7	Projections of the trajectory of the VEX orbit 85 on the equatorial, polar and terminator plane of our hybrid simulation.	70
3.8	Global 3D view of simulation results showing the magnetic field strength.	71
3.9	Global 3D view of simulation results showing the heavy ion density. . . .	72
3.10	Simulation results of Run 1 in the terminator plane	72
3.11	Simulation results of Run 1 in the polar plane.	74
3.12	Simulation results of Run 1 in the equatorial plane.	75
3.13	Simulation results of Run 2 in the terminator plane.	78
3.14	Simulation results of Run 2 in the polar plane.	79
3.15	Simulation results of Run 2 in the equatorial plane.	80
3.16	Cold O and hot O ⁺ number densities at solar maximum as a function of altitude.	82
3.17	The neutral number density and ion production rates of oxygen as a function of altitude at solar maximum.	83
3.18	Simulation results of Run 3 in the terminator plane.	85
3.19	Simulation results of Run 3 in the polar plane.	86
3.20	Simulation results of Run 3 in the equatorial plane.	87
4.1	Comparison of the solar wind bulk velocity from simulation Run 1 with IMA data.	92
4.2	Comparison of the heavy ion velocity from simulation Run 1 with IMA data.	93
4.3	IMA data recorded on 15 July 2006 between 00:47 – 03:21 UT.	94
4.4	Comparison of the heavy ion density and solar wind density from the simulation Run 1 with IMA and ELS measurements.	95
4.5	Comparison of the interplanetary magnetic field derived from simulation Run 1 with MAG measurements.	96
4.6	Comparison of the motional electric field obtained by the model (Run 1) with VEX observations.	97
4.7	Comparison of the solar wind density from the simulation Run 2 with ELS data.	99
4.8	Comparison of the solar wind bulk velocity from simulation Run 2 with IMA data.	101
4.9	Comparison of the magnetic field from the simulation Run 2 with MAG data.	102
4.10	Comparison of the electric field from simulation Run 2 with VEX observations.	103
4.11	Atmospheric escape fluxes at solar minimum as a function of the timestep of simulation obtained by Run 1 and Run 2 based on VEX input parameters.	105
4.12	Atmospheric escape fluxes at solar maximum as a function of the timestep of simulation obtained by Run 3 based on PVO input parameters.	106

List of Tables

1.1	Table comparing the orbital parameters of the terrestrial planets.	16
1.2	Table comparing some physical parameters of the terrestrial planets.	16
1.3	Table comparing the atmospheric parameters of the terrestrial planets.	21
2.1	The performance of the Electron Spectrometer and Ion Mass Analyzer.	42
3.1	Venusian bow shock fit parameters from ASPERA-4/VEX in comparison with earlier studies.	60
3.2	Upper and lower mantle boundary fit parameters from ASPERA-4/VEX.	60
3.3	List of simulation parameters used for Run 1.	69
3.4	List of simulation parameters used for Run 2.	77
3.5	List of simulation parameters used for Run 3.	84

Abstract

The thesis deals with the investigation of the plasma environment of Venus using data of the ASPERA-4 (Analyzer of Space Plasmas and Energetic Atoms) experiment onboard the Venus Express (VEX) spacecraft as well as a 3D hybrid code in order to study the solar wind - atmosphere interaction of an unmagnetized planet.

(1) Data Analysis: By using data from the ion and electron spectrometers, the shapes and average locations of the plasma boundaries (bow shock, upper and lower boundary of the mantle region) around the planet are determined. Additionally, the variation of the terminator bow shock position is analyzed as a function of the solar wind dynamic pressure and solar EUV flux. It is demonstrated that the shock location is insensitive to the upstream ram pressure and that the changes in the solar EUV radiation are too small over the period of the VEX observations to analyze solar activity dependence.

(2) Discussion of simulation results: The results of this data analysis and earlier studies are qualitatively compared with three-dimensional hybrid simulations which are based on VEX observations during low solar activity. But also simulations with PVO input parameters typical for solar maximum conditions are performed and compared with the VEX simulation results. In the hybrid model, ions are treated as individual particles moving in self-consistently generated electromagnetic fields and electrons are modeled as a massless charge neutralizing fluid. The planetary heavy ion plasma is generated by an oxygen ionosphere and exosphere adapted to a profile, which depends on the altitude above the surface and solar zenith angle (Chapman layer).

(3) Comparison between model and data: The main focus of this study is the comparison of the plasma and magnetic field measurements provided by VEX with the results of three-dimensional hybrid simulations. The hybrid model is able to produce an adequate picture of the global plasma dynamics and processes at Venus. The positions of the plasma boundaries are well reproduced by the model and the simulated parameters are in fairly good agreement with the values measured by the ASPERA-4 and Magnetometer instruments. Moreover, the hybrid simulations demonstrate that the orientation of the interplanetary magnetic field determining the direction of the solar wind electric field plays an important role for the pickup and escape processes. Since Venus does not possess an intrinsic magnetic field its atmosphere becomes eroded by the solar wind. The simulated atmospheric escape rates are within the limits of theoretical and observed loss rates showing that the hybrid code is able to provide an insight into the loss processes of oxygen at Venus induced by the solar wind.

Future aspects: It is expected that the accuracy of the model can be significantly increased by the comparison of model data with measurements which then can be used to estimate boundary positions and escape fluxes under conditions different from today.

1 Introduction

Our neighboring planet Venus is already anchored in the human consciousness for a long time and was known in many cultures having different names: *Venus* (Roman), *Aphrodite* (Greek), *Inanna* (Sumerian), *Ishtar* (Babylonian), *Nephtys* (Egyptian) and *Astarte* (Syro-Palestinian). In general, Venus was associated with the female gender, except in ancient India, where the planet was called *Shukra* (the Sanskrit for “clear, pure” or “brightness, clearness”) who was the son of Bhrigu and Ushana (Figure 1.1).

Mythology. Venus received the name of the Roman goddess of love and beauty, daughter of Jupiter and wife of Vulcan. The goddess Venus is said to be the ancestress of the Roman people because of Aeneas, who was believed to be the founding father of Rome, and the son of Venus and the mortal Anchises. Consequently, Venus played an important role in many Roman religious festivals and myths. She had several epithets like other major Roman gods which were associated with the different roles of the goddess. For example, Julius Caesar introduced the cult “Venus Genetrix” (“Mother Venus”), worshipping Venus as the goddess of motherhood and domesticity because she was thought to be the mother of the Julian gens. In other words, the Julians claimed to have been descended from Venus’ grandson Iulus, a son of Aeneas.



Figure 1.1: Left: Shukra, the divine personification of the planet Venus in the ancient Indian system of astronomy and astrology. Right: Ishtar, the goddess of fertility, love, and war who is the Babylonian counterpart of Venus.

Classical and prehistoric art. Besides mythology, Venus also played an important role in the history of art. During the Renaissance period in Europe, Venus became a popular subject of many sculptors and painters. Here, the term Venus stands for the

depiction of nude female bodies who are not necessarily associated with the goddess. Famous artworks (Figure 1.2) are for instance, the painting “*The Birth of Venus*” by Sandro Botticelli (1485) or the “*Venus of Milo*” which is one of the most famous ancient Greek sculptures, thought to be the work of Alexandros of Antioch (100 A.C.). But we also find the name Venus in the field of prehistoric art. “Venus figurines” is a collective term for small sculptures of rounded female forms, originating from the upper Paleolithic. A well-known example is the “*Venus of Willendorf*” (24000 B.C. – 22000 B.C.), a small statue (11.1 cm) made of limestone which was found in Lower Austria in 1908.



Figure 1.2: Left: *The Birth of Venus* painted by Sandro Botticelli (1485). Middle: *Venus of Milo*, a famous ancient Greek statue (100 A.C.). Right: *Venus of Willendorf*, a small statuette of a female figure (24000 B.C. – 22000 B.C.).

Thus, the name Venus is not only associated with the planet but occurs in human culture in different forms for a long time already. But in order to introduce the topic of this thesis, I would like to summarize the earliest observations of the planet Venus, before the time of the spaceflight era. It is only an abridgement of discoveries regarding the planet Venus by means of ground-based observations and should give an idea about what was possible before the era of space exploration of planets in the solar system.

General survey on Venus. Since Venus is the brightest natural object in the sky after the Sun and the Moon, it was the first luminary that humans learned to recognize among the thousands of stars in the night sky. Most likely, the Babylonians were the first people who put their Venus observations on record, namely on the so-called “*Venus tablet of Ammisaduqa*” (~ 1700 B.C.) now at in the British Museum in London. It is a cuneiform tablet containing records of the first and last visibility of Venus on the horizon during dawn and dusk. Before the invention of the telescope, Venus was known as a “wandering star” like Mercury, Earth, Mars, Jupiter and Saturn. The ancient Greek were maybe the first culture who thought Venus being two objects - a morning star (“*Heosphoros*”) and an evening star (“*Hesperos*”) (Luhmann et al. 1992). In 6 B.C., Phythagoras realized that they were the same object, the planet Venus.

The study of the planet’s nature began in the early 17th century. Around 1610 Galileo made the first telescopical observations of Venus and established its phases, analogous to the well-known phases of the Moon, namely varying from crescent to gibbous to full

and vice versa. But these phases were only possible if Venus is orbiting the Sun. Therefore, this discovery supported the heliocentric system of Nicholas Copernicus and was in disagreement with the Ptolemean geocentric system.

In 1761, the Russian scholar Mikhail V. Lomonosov at the Saint Petersburg Observatory proved that Venus has an atmosphere. Lomonosov observed the transit of Venus across the disk of the Sun, determined the refraction of solar rays and concluded that Venus possesses an atmosphere. 30 years later Lomonosov's finding was confirmed by the German astronomer Johann Schröter and the English astronomer William Herschel. They observed the crepuscular phenomena on Venus which are the result of scattered solar rays in the upper portion of the planet's atmosphere (Marov and Grinspoon 1998).

Spectroscopic observations provided the first information on the chemical composition of the Venusian atmosphere. Infrared spectroscopy carried out in 1932 suggested for the first time that the planet's atmosphere has a quite high carbon dioxide (CO₂) content. Around 20 years later, it seemed that CO₂ is a relatively small component in the atmosphere, based on theoretical and laboratory research correlated with spectroscopic measurement data. In 1968, after interpreting new, higher-quality spectra of Venus it was shown that the previous estimates of CO₂ content were much too low. The analysis of high-resolution Fourier spectroscopy of Venus arrived at the same conclusion and CO₂ was identified as the main constituent in the Venusian atmosphere (see Marov and Grinspoon (1998) for a review).

Progress in the scope of ground-based observations has been made in the middle of the 20th century, after the invention of radars and the radio astronomy. Radar is a very useful tool in determining planetary distances, size and rotational elements as well as surface properties.

In the mid-1950s the first reliably radio emission from Venus were recorded and microwave observations indicated for the first time that Venus has a very hot surface temperature of at least 600 K (Marov and Grinspoon 1998).

The first successful measurements regarding the rotational period of the planet were carried out near the inferior conjunction of Venus in 1961, in the United States at the Millstone-Hill and Goldstone Observatories, and in the USSR with the large antenna of the Deep Space Network Center in the Crimea, using radiowaves in the decimeter range (Marov and Grinspoon 1998). Based on these observations one could prove by the end of the 1960s that Venus rotates very slowly in a retrograde direction exhibiting a rotational period of about 243.0 days.

The later discoveries on the plasma environment made by satellite missions are discussed in section 1.3.

1.1 The Planet Venus

1.1.1 General properties

Venus is the second planet from the Sun and orbits it almost circularly at a mean distance of about 108.21 million kilometers (0.72 AU ... Astronomical Units) (see Table 1.1). Among all other major planets, Venus has by far the slowest rotation period of 243.696 Earth days while the orbital period is only 224.7 Earth days and thus, the year is shorter

Orbital Parameters	Mercury	Venus	Earth	Mars
Orbital distance (10^6 km)	57.91 0.39 AU	108.21 0.72 AU	149.6 1.0 AU	227.92 1.52 AU
Sidereal orbit period (days)	87.969	224.701	365.256	686.980
Tropical orbit period (days)	87.968	224.695	365.242	686.973
Perihelion (10^6 km)	46.00	107.48	147.09	206.62
Aphelion (10^6 km)	69.82	108.94	152.1	249.23
Mean orbital velocity (km/s)	47.87	35.02	29.78	24.13
Orbit Inclination (deg)	7.0	3.39	0.0	1.850
Orbit eccentricity	0.2056	0.0067	0.0167	0.0935
Obliquity to orbit (deg)	0	177.36	23.45	25.19
Sidereal rotation period (hrs)	1407.6	- 5832.5	23.9345	24.6229
Length of day (hrs)	4222.6	2802.0	24.0	24.6597
Number of moons	0	0	1	2
Global magnetic field?	Yes	No	Yes	No

Table 1.1: Table comparing the orbital parameters of the terrestrial planets Mercury, Venus, Earth and Mars (Williams 2005).

Bulk Parameters	Mercury	Venus	Earth	Mars
Mass (10^{24} kg)	0.3302	4.8685	5.9736	0.64185
Volume (10^{10} km ⁻³)	6.083	92.843	108.321	16.318
Equatorial radius (km)	2439.7	6051.8	6378.1	3396.2
Polar radius (km)	2439.7	6051.8	6356.8	3376.2
Ellipticity (Flattening)	0.0	0.0	0.00335	0.00648
Mean density (kg/m ⁻³)	5427	5243	5515	3933
Surface gravity (eq.) (m/s ²)	3.7	8.87	9.8	3.71
Escape velocity (km/s)	4.3	10.36	11.19	5.03
Planetary albedo	0.119	0.750	0.306	0.250
Solar irradiance (W/m ²)	9126.6	2613.9	1367.6	589.2

Table 1.2: Table comparing some physical parameters of the terrestrial planets Mercury, Venus, Earth and Mars (Williams 2005).

than the day on Venus. Additionally, the planet rotates retrograde (clockwise), like Uranus, whereas all other planets rotate prograde (counter-clockwise). That means, for an observer on Venus the Sun would rise in the west and set in the east. This very slow and

retrograde rotation is one of the major questions which scientist try to answer since its discovery but the puzzle has not been solved yet. However, there are two possible explanations why Venus rotates backwards. One theory is that Venus collided with a planet-sized object early in the planetary formation process. Another theory says that the tidal effects from its dense atmosphere could have slowed its initial rotation on the value seen today.

The radius of the planet Venus is 6051.8 km (0.95 Earth radius) and its mass is around 4.9×10^{24} kg (0.82 Earth masses) with a mean density of 5243 kg m^{-3} (0.951 Earth density) (see Table 1.2). The average temperature and pressure at the surface are $\sim 737 \text{ K}$ (464°C) (Earth: 288K or 15°C) and 92 bar (Earth: 1bar), respectively (see Table 1.3). The Venusian atmosphere is 94 times as massive as the Earth's atmosphere with the main constituents carbon dioxide (96.5 %) and nitrogen (3.5 %) and very little water (20 ppm ... parts per million). The surface of Venus is isothermal with a constant temperature between day and night as well as between the equator and the poles. The values presented in this section are taken from Williams (2005) where further sources are given.

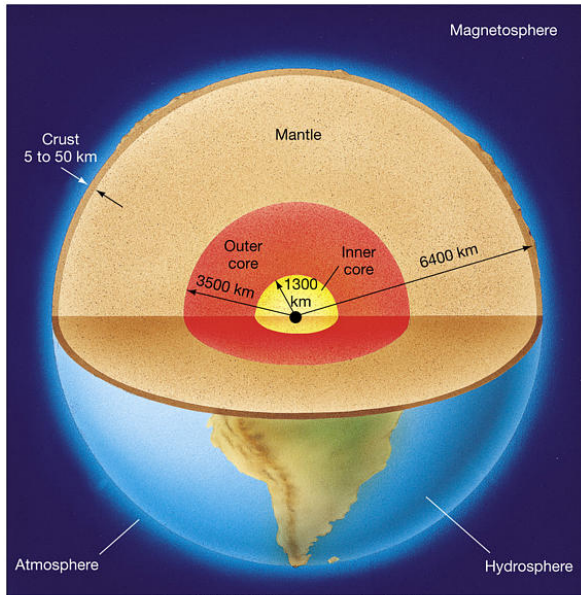
1.1.2 The interior

All terrestrial planets accreted from iron and silicate-bearing planetesimals around 4.5 billion years ago and most likely, differentiated in a similar manner (Luhmann and Russell 1997). Therefore, they possess the common feature of a molten-iron rich core about half the planet's radius, which is covered by a crust of the remaining material (mainly silicate). It is difficult to investigate the interiors of those planets but based on seismic measurements of Earth, we are able to draw plausible conclusions about the interiors of Venus, Mars and Mercury.

Since Venus and Earth are similar in size and density, it is reasonable to assume that Venus has a similar internal structure like Earth (see Figure 1.3), namely a core (at least partially liquid), mantle and crust (see Figure 1.4). The mean density of Venus is slightly smaller than that of Earth so that we can expect compositional differences. The slightly smaller radius of Venus suggests that the pressures are significantly lower in its deep interior. The interior of Venus is modeled by different approaches which are all based on Earth-like planets taking into account the internal temperatures and pressures of Venus. These models lead to different hypotheses. One possibility is that the core is completely solid or "frozen" today. The other possibility is that the solidification has not yet commenced or has stopped at some time in the past. (Luhmann and Russell 1997)

1.1.3 The lack of a magnetic field

One of the main differences between Earth and Venus is the absence of an intrinsic magnetic field at Venus. Most probably, Venus once had an intrinsic magnetic field, namely in the first billion years of its life due to a dynamo which was operating in the liquid core of a newly accreted terrestrial planet. This dynamo was driven by thermal convection caused by the heat which was left over from the accretion phase (Luhmann and Russell 1997). Thus, a dynamo requires a conducting liquid, rotation and convection. But after some time this energy source (thermal convection) was exhausted and obviously no other source was available in order to maintain this dynamo. In the case of Earth, the initial



Copyright © 2005 Pearson Prentice Hall, Inc.

Figure 1.3: A cutaway of the six regions of the Earth, the core, mantle, crust, hydrosphere, atmosphere and magnetosphere. © 2005 Pearson Prentice Hall, Inc.

thermal convection has been replaced by heat from radioactive decay of uranium and thorium as well as by the release of heat of fusion resulting from the gradual solidification of its outer core. In other words, convection arises from a temperature difference in the Earth's outer core because the bottom is much hotter than the top of the liquid layer. But most probably, this is not the case for Venus. Very likely, Venus has a liquid outer core like Earth, which does not convect and has uniform temperature. Hence, it is reasonable to assume that either Venus has no solid inner core or that its core is not currently cooling. The lack of an inner core can be explained by the absence of plate tectonics which would let off heat in order to cool the core. Thus, the mantle of Venus cannot cool quick enough to drive a core convection and thus, a dynamo. Another reasonable explanation could be that the core of Venus has already completely solidified (Stevenson 2003, Nimmo 2002).

Consequently, no magnetosphere exists which would shield the upper atmosphere from cosmic radiation and solar wind. However, a very small magnetic field is present, called induced magnetic field, which is the result of the direct interaction between the highly conductive ionosphere and the oncoming solar wind. This finding raised important questions such as: Why does Venus lack a magnetic field? Did Venus ever possess a magnetic field?

It is important to note that the slow rotation of Venus is not responsible for the lack of a

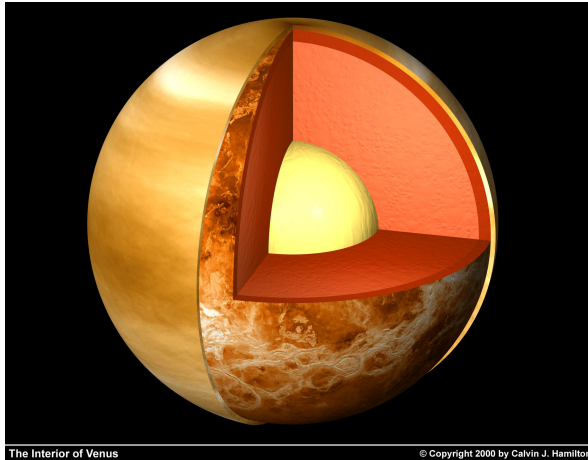


Figure 1.4: A cutaway view of a possible internal structure of Venus. The surface is derived from Magellan radar images. The crust is shown as dark red, the mantle as light red and the inner core as yellow. © 2000 by Calvin J. Hamilton

magnetic field because a slow rotation favours the maintenance of dynamos. Also relevant to note is that Venus, unlike Mars, does not exhibit remanent crustal fields originating from a possible early period of dynamo activity because estimations of temperatures in the crust lead to the conclusion that they are above the Curie point (Stevenson 2003, Nimmo 2002).

1.1.4 The surface

The Pioneer Venus Orbiter and Magellan missions carried out radar altimetry providing information about the Venusian surface and its topography (see Figure 1.5). The surface consists of smoothly rolling plains (70 %), lowland regions (20 %) called “planitia” and highland areas (10 %) called “terrae”. The two most prominent continental-sized features are Ishtar terra and Aphrodite terra. Ishtar terra is located in the northern hemisphere and its size is comparable with Australia. In the middle of Ishtar lies Maxwell Montes (11 km) which is the highest mountain on Venus. Aphrodite terra is found near the equator being as large as Africa. The lowlands show almost no features. Most likely, this can be explained by global resurfacing which means that the planitia have been flooded by lava within the last 500 Million years (Taylor 2006).

On Earth, the main mechanism for internal heat loss are plate tectonics and plate boundary volcanism. But Venus does not have plate tectonics and thus, internal heat is probably lost through hotspot volcanism (Leftwich et al. 1999). Indeed, most of the Venusian surface has been shaped by volcanic activity which becomes apparent by hundreds of volcanoes of different sizes and respective lava flows. Therefore, the surface exhibits

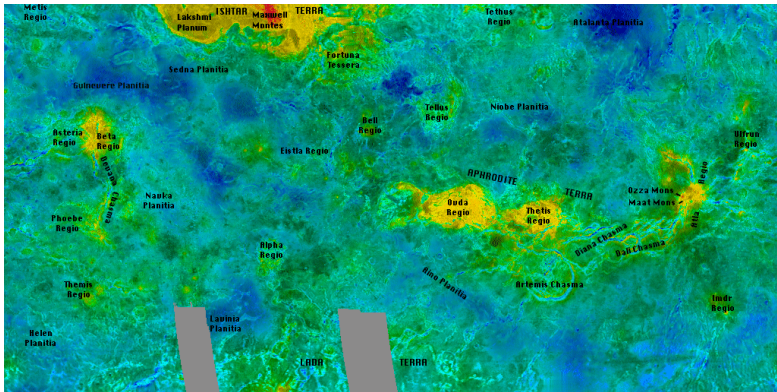


Figure 1.5: Map of Venus obtained by Magellan illustrating its topography (smoothly rolling plains, lowland regions called “planitia” and highland areas called “terrae”). © NASA/JPL.

enormous calderas which are more than 100 kilometers in diameter whereas the terrestrial craters are only several kilometers in diameter. But not all of the craters found on Venus are of volcanic origin. There are also many impact craters caused by large meteorites.

The surface of Venus has been estimated to be less than 1 billion years old, which is quite young compared to Mars or Mercury, and is ascribed to global resurfacing. Some scientist suggest that the ongoing volcanic activity is probably the driving force of planetary resurfacing. Others suggest that volcanism is ongoing on Venus but at a reduced rate after a global resurfacing event (Leftwich et al. 1999), so that the interior of Venus is essentially heating up.

1.1.5 The atmosphere and its evolution

The atmosphere of Venus is strikingly different from the Earth’s atmosphere. It is very massive and composed mainly of carbon dioxide and nitrogen with small amounts of sulphur dioxide, argon, water vapor and carbon monoxide as listed in Table 1.3.

The current state of the Venusian atmosphere can be explained by the high equilibrium temperature at the surface and the greenhouse effect associated with it. If the terrestrial planets were formed from well-mixed solar nebular material, it is highly likely, that Venus once had the same amount of liquid water as Earth. However, the outgassed water could not condensate due to high surface temperatures since the increased saturation vapor pressure amplified the greenhouse effect which in turn led to a further increase of the surface temperature. This self-energizing greenhouse effect is known as a runaway greenhouse effect. Even, if the early Venus has not been that wet, the amount of outgassed carbon dioxide was sufficient to initiate the greenhouse effect and thus, leading to extremely high surface temperatures (Bauer 2001).

It is important to note that on Venus, carbon dioxide was not embedded into rocks due

Atmospheric Parameters	Mercury	Venus	Earth	Mars
Total mass of atmosphere (kg)	< 1000	4.8×10^{20}	5.1×10^{18}	2.5×10^{16}
Atmospheric composition				
Major (%)	O ₂ 42.0 Na 29.0 H ₂ 22.0 He 6.0 K 0.5	CO ₂ 96.5 N ₂ 3.5	N ₂ 78.1 O ₂ 20.9 H ₂ O 1.0	CO ₂ 95.32 N ₂ 2.7 Ar 1.6 O ₂ 0.13 CO 0.08
Minor (ppm)	Ar CO ₂ H ₂ N ₂ Xe Kr Ne	SO ₂ 150 Ar 70 H ₂ O 20 CO 17 He 12 Ne 7	Ar 9340 CO ₂ 380 Ne 18.18 He 5.24 CH ₄ 1.7 Kr 1.14 H ₂ 0.55	H ₂ O 210 NO 100 Ne 2.5 HDO 0.85 Kr 0.3 Xe 0.08
Surface pressure (bars)	10^{-15}	92	1	0.01
Surface density (kg/m ⁻³)	–	65.0	1.217	0.02
Average temperature (K)	440	737	288	210

Table 1.3: Table comparing the atmospheric parameters of the terrestrial planets Mercury, Venus, Earth and Mars (Williams 2005).

to the absence of water but instead was accumulated in the atmosphere. If the terrestrial carbon dioxide would have not been absorbed in the oceans and rocks, 98 % of carbon dioxide were released into the Earth's atmosphere, leading to an atmospheric pressure which would be 70 times of what it is now. Except for oxygen and water, the atmosphere of Earth would be quite similar to that of Venus, if the carbon dioxide would not have been absorbed in the past.

Venus is completely covered by a thick cloud layer, located between 45 and 65 km above the surface (Taylor 2006), which consists mainly of sulfur dioxide and sulfuric acid droplets. This layer inhibits direct investigations of the Venusian surface in the visible light but the clouds are not opaque in the near-infrared and ultraviolet wavelengths. The cloud tops rotate very fast around the planet with a period of only 4-5 days due to wind velocities of 100 m s^{-1} (Markiewicz et al. 2007). These high retrograde speeds reached near 60 km height are surprising for such a slowly rotating planet but the factors which are responsible for this super-rotation are still unknown. Below the clouds the wind velocities decrease with decreasing altitude because the atmosphere becomes denser. Near 10 km height the winds are already less than 10 m s^{-1} and are close to zero at the surface.

Venus has a planetary albedo of 0.75 (Earth: 0.31) which means that 75 % of the incident solar radiation is reflected back into space without being absorbed due to the planet-wide cloud blanket. Only $\sim 10 \%$ of the sunlight diffuses through the cloud layer

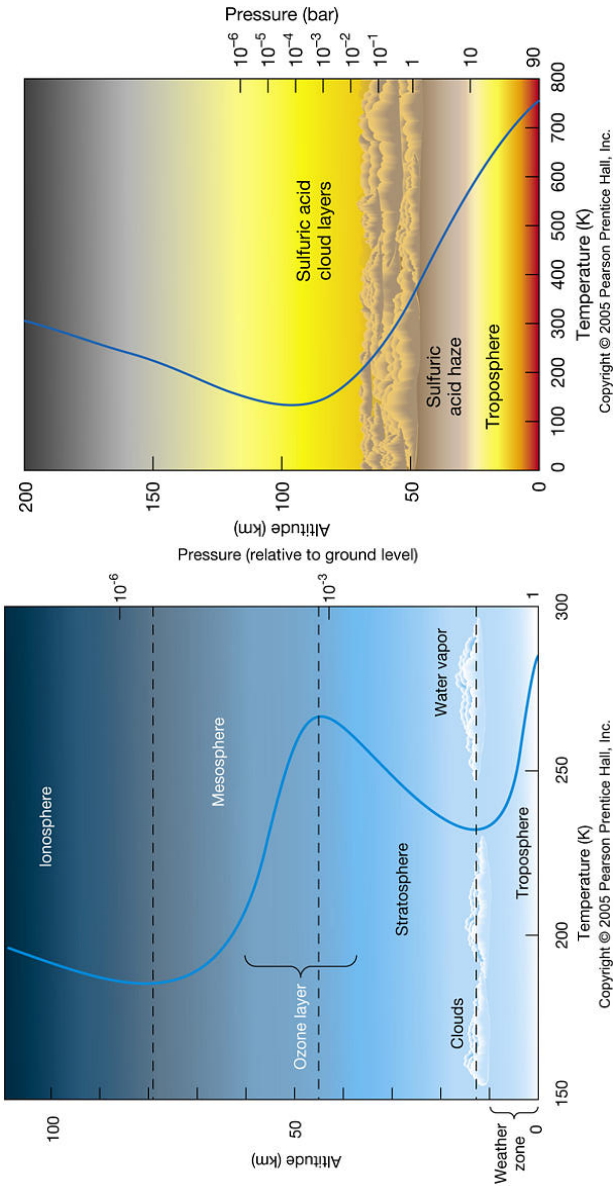
providing about 17 W cm^{-2} of solar irradiation at the surface (Taylor 2006). The thermal infrared heat energy is trapped in the lower atmosphere and hence, raising the surface temperature up to 737 K. The CO_2 in the atmosphere contributes to the strong greenhouse effect on Venus, but other gases, such as SO_2 , CO and HCl, also increase the surface temperatures. The atmosphere also contains a small amount of water in the form of water vapor (10 mbar). In contrast to Earth: if all the water on Earth was put into the atmosphere, there would be about 100 bars of atmospheric pressure.

How can we explain the small amount of water that is present in the atmosphere of Venus? There are two hypotheses (Bauer 2001): (1) Either Venus developed with a small amount of material containing water and the present water originated from comet impacts, (2) or Venus was once wet (maybe as wet as Earth) but water was lost over geological time scales. This latter theory is supported by the measured ratio of deuterium-to-hydrogen (D/H). Since hydrogen is lighter than deuterium, it escapes more easily from the atmosphere leading to an enrichment of deuterium in the atmosphere. Most probably, the early Venus was wetter than it is today because the D/H-ratio on Venus is about 150 times larger than the terrestrial value. Possible escape mechanisms are discussed in subsection 1.1.7.

Like the Earth's atmosphere (see left panel of Figure 1.6), one can divide the atmosphere of Venus into different layers defined by temperature, composition and degree of ionization. The atmosphere can be structured into a lower, middle and upper atmosphere based on its temperature gradient (see right panel Figure 1.6). The lower region is called troposphere, reaching from the ground up to $\sim 62 \text{ km}$ height, and is characterized by a negative adiabatic lapse rate of about -10 K/km , i. e. the temperature decreases continuously with increasing height. The upper boundary of the troposphere is referred to as tropopause. The strong greenhouse effect is responsible for the extremely high equilibrium temperature near the surface due to the large concentration of carbon dioxide. The middle atmosphere, or mesosphere, is located between 62 and 120 km above the surface. The temperature decreases with altitude and reaches 150 K near 80 km altitude while the atmosphere is almost isothermal between 80 and 110 km height. A temperature minimum is reached at the mesopause near 120 km. The upper part is called thermosphere, lying above the mesosphere, and is characterized by a temperature difference between the dayside and nightside of Venus. On the dayside the temperature increases with height, reaching about 300 K near 170 km while on the nightside colder temperatures of 100-130 K are observed. Therefore, the nightside is often referred to as the cryosphere.

Collisions between neutral atoms become negligible above around 180 km altitude which is called the exosphere with its lower boundary referred to as exobase. In this region particles can escape from the atmosphere if their kinetic energy exceeds the gravitational binding energy and if they move along an upward trajectory without colliding with another atom or molecule.

The temperature increase in the thermosphere is much less than that on Earth although Venus is much closer to the Sun. This results from the abundant carbon dioxide in the Venusian atmosphere which is a very efficient cooling agent (de Pater and Lissauer 2001). There is another difference between both planets. Venus does not have a stratosphere like Earth, where a temperature rise occurs due to the radiation absorption by ozone.



Copyright © 2005 Pearson Prentice Hall, Inc.

Copyright © 2005 Pearson Prentice Hall, Inc.

Figure 1.6: Left: The vertical structure of the Earth's atmosphere. Right: The temperature gradient of the Venusian atmosphere. © 2005 Pearson Prentice Hall, Inc.

In terms of its composition the atmosphere can be described as follows: The lower atmosphere is well mixed and therefore called homosphere where the main constituent is carbon dioxide (CO₂). Its upper boundary, the homopause, is reached near 135 km altitude. Above that lies the heterosphere where a separation by molecular weight occurs, i. e. lighter molecules have large scale heights while heavier molecules are found at lower heights only. Hence, in the upper atmosphere (above 150 km) atomic oxygen becomes the dominant neutral species and is replaced by helium, non-thermal atomic oxygen and eventually atomic hydrogen at even higher altitudes (Schunk and Nagy 2004).

In terms of its ionization state the atmosphere can be divided as follows: The neutral atmosphere of Venus is found between 50 and 90 km altitude where almost no ionized particles exist. Above 100 km the atmosphere is ionized by solar radiation and therefore, is called the ionosphere.

1.1.6 Ionosphere

The ionosphere on the dayside produces a plasma density maximum of about $3\text{-}5 \times 10^5 \text{cm}^{-3}$ by means of photoionization of the main constituent CO₂



near 140 km height where the optical depth (τ_0) equals one. The dayside ionosphere of Venus behaves like a Chapman layer in which ion production by solar EUV radiation is balanced by photochemical recombination (Brace and Kliore 1991). In other words, the maximum of electron (ion) density is identical to the height of the ion production rate maximum where $\tau_0 = 1$ for ionizing radiation at zenith $\chi = 0$ (Chapman theory).

However, the major ion at the peak altitude is not CO₂⁺ but O₂⁺ which is generated by the following photochemical processes: atom-ion interchange



or charge transfer



which is quickly followed by the reaction



At higher altitudes also O⁺ and H⁺ ions become important. In addition to this well-developed dayside ionosphere one can find also a significant nightside ionosphere with peak plasma densities of around 10^4cm^{-3} at an altitude near 140 km (Knudsen 1992). Since the night on Venus lasts about 58 Earth days the photoionization process can not be considered as source for the ionospheric nightside. Rather plasma transport from the day-side due to pressure gradients and low energy electron impact ionization are responsible for maintaining the nightside ionosphere.

Since Venus does not possess an intrinsic magnetic field (see Subsection 1.1.3) the solar wind interacts directly with the upper atmosphere producing a pressure balance between the solar wind ram pressure and the thermal pressure of the ionosphere. This

boundary is called ionopause (detailed discussion found in Subsection 1.2.4) and is characterized by a sudden decrease in ionospheric density. The altitude of the ionopause depends on the level of solar activity and solar zenith angle. It is found in the sub-solar region near 300 km for average solar conditions and increases towards the terminator (~800 km).

1.1.7 Escape of atoms and ions

Unlike Earth, Jeans escape does not play a significant role for atmospheric loss on Venus because the exospheric temperature is relatively low ($T_V = 300$ K, $T_E = 1000$ K).

However, non-thermal processes are of importance on Venus (and Mars). For example, charge exchange



and dissociative recombination



produce hot H^* atoms which are accelerated beyond escape velocity if they gain sufficient excess energy (*) in these reactions and as a result, they escape from the gravity field of Venus. Furthermore, atmospheric ions are also lost from the atmosphere because the solar wind interacts directly with the ionosphere of Venus which is illustrated in Figure 1.7. Dissociative recombination of the main ion O_2^+ produces an extended hot oxygen corona on the dayside from where hot O^* ions can be dragged off by the solar wind flow (pickup process). Whereas on the nightside of Venus accelerated planetary ions can be lost through the plasma tail (Bauer 2001). Moreover, heavy O^+ ions can be lost from the ionosphere by means of detached plasma clouds which seems to be triggered by magnetohydrodynamic (MHD) instabilities (e. g. interchange instability, Kelvin-Helmholtz instability) occurring at the dayside ionopause. Pioneer Venus Orbiter (PVO) observed such plasma clouds above the ionopause, primarily near the terminator and further downstream. Brace et al. (1982) investigated several of these clouds and demonstrated that the plasma within the clouds originate from the Venusian ionosphere since the electron temperature and density were similar to that observed in the ionosphere. Finally, when a fast incident plasma ion or freshly-produced pickup ion hits an atmospheric atom, the atom gains energy in this collision which can initiate a cascade of elastic collision between atmospheric particles, extending over 10's of kilometers. In this cascade of collisions, the resulting fast atoms can be knocked upward into ballistic trajectories and thus, populate the corona. However, some of these sputtered atoms have sufficient momentum in the right direction in order to escape the gravitational field of Venus. This loss process is called atmospheric sputtering where energy transfer events are caused by fast incident ions. On Venus, sputtering is the only process which produces neutral O escape fluxes (Lammer et al. 2006).

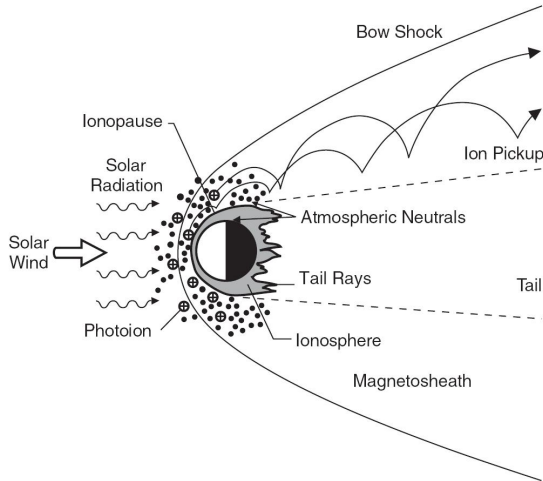


Figure 1.7: Since Venus does not possess an intrinsic magnetic field, the solar wind interacts directly with the ionosphere and hence, leads to atmospheric escape by means of photoionization, charge exchange and electron impact ionization. (Russell et al. 2006)

1.1.8 What are the similarities and differences between Venus and Earth?

Venus is often referred to as “Earth’s twin” due to the similarities between both terrestrial planets. First of all, Venus is the closest planet to Earth in terms of its mean orbital distance from the Sun (0.72 AU). Furthermore, the planets are about the same size, mass, mean density and surface gravity. Then, CO_2 and N_2 are found in both atmospheres. Additionally, Venus is assumed to have the same solid-body composition and interior heat source as Earth.

However, more appropriate would be the denotation “Earth’s evil twin” because Venus offers an extremely hostile and harsh world for any form of life compared to Earth. The fundamental differences are the absence of a natural satellite around Venus and the lack of an intrinsic Venusian magnetic field. Another large discrepancy appears in the rotation of the solid body. Venus rotates very slowly and retrograde once every 243 days while Earth’s prograde rotation period is 24 hours. Then, the Venusian atmosphere, primarily composed of CO_2 , is 94 times denser than the Earth’s atmosphere. The greenhouse effect is much stronger on Venus than on Earth, leading to an extreme surface temperature and pressure. As a result of the very hot surface environment, liquid water is unstable on the Venusian surface. Unlike Earth, Venus does not have plate tectonics but suffers from occasional catastrophic volcanic resurfacing.

1.1.9 Replace Venus with an Earth-like planet – what happens?

What would happen, if an Earth-like planet is put at the position of Venus? The atmosphere of the planet would begin to warm up due to the higher input of solar energy. The higher temperatures imply that the atmosphere would be able to hold more water vapor and as a result, some of the oceans' water would start to evaporate. Since water vapor is a greenhouse gas which absorbs thermal heat energy, it would lead to an increase in atmospheric water vapor which in turn would lead to an increase in atmospheric temperature. Consequently, the atmosphere would be capable to hold even more water vapor and the oceans would evaporate. The system would stabilize, when all the liquid water on the surface was absorbed and the temperature was extremely high. This scenario is known as "Runaway Greenhouse Effect" and is in fact what has happened to Venus.

Why did not Earth undergo the same runaway greenhouse effect? The decisive element is Earth's location in the solar system. The atmosphere of Earth is holding much less water vapor compared to Venus because of the lower atmospheric temperatures. Additionally, the atmosphere is stable at relatively low water abundances and temperatures. In order to trigger a runaway greenhouse effect, Earth would need about 40 % more solar irradiance. That would be achieved either if Earth would be closer to the Sun or if the Sun would put out more energy. However, the Sun's output increases with time so that one day (about 2 billion years from now), Earth probably will develop a runaway greenhouse situation. But would the water be lost? The water vapor content would significantly enhance in the atmosphere but which may lead to an increase in exobase temperature and respective increase in Jeans escape. Whether an increase in ionospheric density will lead to an enhanced ion loss is not obvious because the ionosphere is protected by the global magnetic field.

1.2 Types of plasma interaction with magnetized and unmagnetized bodies

The nature of solar wind interaction with a planet or satellite is characterized by two properties, namely whether it has an intrinsic magnetic field or/and a substantial atmosphere. As demonstrated in Figure 1.8, one can distinguish between four different types of plasma interaction: bodies which have

1. a global magnetic field and an atmosphere,
2. a planetary magnetic field but no significant atmosphere,
3. no intrinsic magnetic field but a substantial atmosphere,
4. neither an internal magnetic field nor an atmosphere.

In the following subsections I will explain in short each type of plasma interaction on the basis of one example in order to demonstrate their differences.

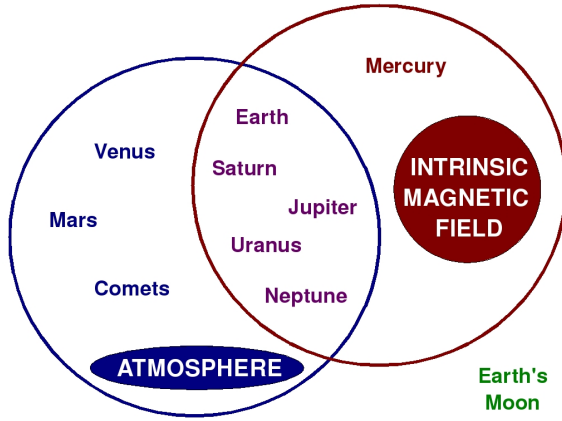


Figure 1.8: How the solar wind interacts with a planet depends on the existence of a global magnetic field and/or a significant atmosphere.

1.2.1 Earth's Moon

Our moon represents the simplest case of the various plasma interactions since it does neither have an internal magnetic field nor a significant atmosphere.

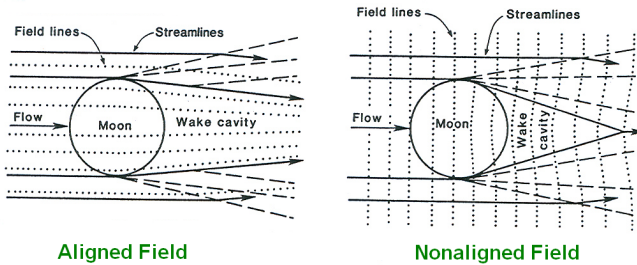


Figure 1.9: Schematic of the solar wind interaction with Earth's moon. Left: The magnetic field lines are parallel to the plasma flow so that the lunar wake can persist to large distances. Right: The magnetic field lines are perpendicular to the undisturbed flow which results in a wake closed immediately behind of the body. (Kivelson and Russell 1995)

It is a poor conductor because it is composed of insulating material and as a result, incident solar wind particles hit its surface directly and are absorbed. The interplanetary magnetic field lines diffuse relatively fast through the body so that its upstream orientation

is almost not disturbed and the wake just behind the obstacle is practically devoid of particles. In this case, no bow shock will form upstream of the Moon because the oncoming plasma flow does not sense that there is an obstacle since no waves are generated at the surface.

Figure 1.9 illustrates two hypothetical configurations for the lunar wake in the solar wind, depending on the orientation of the interplanetary magnetic field (IMF). If the magnetic field of the Moon is zero and the flow speed is high compared with the thermal velocity, the wake will persist to large distances. However, if the plasma flow is slow relative to the thermal speed, thermal motions perpendicular to the flow direction can refill the empty space within a short distance downstream of the Moon (Kivelson and Russell 1995). In other words, the lunar wake can exist far downstream of the obstacle if the IMF is aligned with the upstream flow or it is closed just behind the body if the IMF is nonaligned with the undisturbed solar wind flow.

1.2.2 Earth

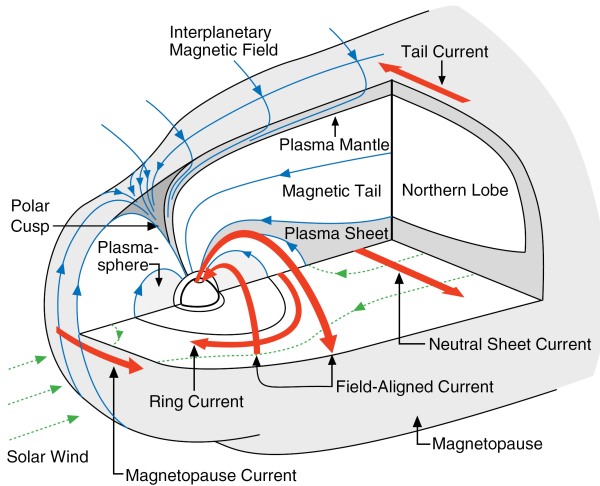


Figure 1.10: The global structure of the Earth’s magnetosphere. (Russell 2000)

Our Earth is an appropriate example in order to demonstrate the complex process of solar wind interaction with a magnetized body which has also a substantial atmosphere, as shown in Figure 1.10.

The dipolar magnetic field acts as a nearly impenetrable obstacle about which the solar wind must flow around. As a result, a magnetic cavity, the magnetosphere, forms.

It is compressed on the dayside and stretched out into an extended magnetotail on the nightside, reaching far beyond the lunar orbit. This magnetotail consists of two lobes of opposite magnetic polarity which are separated by a neutral sheet.

The solar wind is considered as a super-sonic and super-alfvénic flow because the sound speed ($c_s \approx 60 \text{ km s}^{-1}$) and alfvén speed ($v_A \approx 40 \text{ km s}^{-1}$) are significantly smaller than the solar wind bulk velocity ($v_{sw} \approx 400 \text{ km s}^{-1}$). Consequently, a standing magnetosonic shock wave is generated in front of the obstacle, the so-called bow shock, where a substantial fraction of the particles' kinetic energy is converted to thermal energy. The region behind the shock is referred to as magnetosheath where the solar wind continues as a thermalized and subsonic plasma flow. It is a quite turbulent region which is characterized by perpetual changes of the IMF orientation, both spatial and temporal.

The magnetic cavity is bounded by the magnetopause which is a three dimensional surface resulting from the solar wind-magnetic field interaction. It separates a region of relatively weak magnetic field (magnetosheath) from a region which is dominated by the strong terrestrial magnetic field (magnetosphere). Hence, in order to maintain force balance across the magnetopause, it must carry a surface current, known as magnetopause current (Baumjohann and Treumann 1996). It is only a part of a large current system (see Figure 1.10) which is responsible for the transport of charge, momentum, energy and mass as well as formation of magnetic fields inside the Earth's magnetosphere.

The uppermost part of the neutral atmosphere is ionized by solar radiation forming an ionosphere which is connected with the above lying plasmasphere. The torus-shaped plasmasphere is located inside the radiation belt and contains cool but dense plasma of ionospheric origin which co-rotates with the Earth. At high latitudes charged particles originating outside the atmosphere can precipitate along magnetic field lines down to ionospheric altitudes where they collide with and ionize neutral atmospheric particles. As a result, photons emitted by this process produce the polar light (aurora).

1.2.3 Mercury

Mercury possesses a small Earth-like magnetosphere resulting from the solar wind interaction with its global magnetic field. Its intrinsic magnetic field is usually strong enough to stand off the solar wind well above its surface (1.3-2.1 Mercury radii), except for times of increased ram pressure. Then, interplanetary particles can impinge directly onto the surface of Mercury. In contrast to Earth, the planet occupies a relatively large volume of its magnetic cavity so that stable trapping regions, such as the radiation belt, cannot form.

Another important difference between both planets is the absence of an atmosphere. Consequently, there also is no ionosphere which would serve as a source of plasma and charge carriers which implies that the current system of Mercury cannot resemble the current system occurring in the Earth's magnetosphere. The solar wind is considered to be the primary source of Mercury's magnetospheric plasma. However, based on ground-based observations we know that also planetary ions released or sputtered from the surface contribute to the plasma. Moreover, the higher solar wind densities found at Mercury imply that the plasma densities in the plasma sheet are also higher compared to Earth (de Pater and Lissauer 2001).

1.2.4 Venus

Venus does not possess an intrinsic magnetic field to shield the upper atmosphere against the in-coming solar wind flow. The lack of such a magnetic cavity results in a highly structured plasma environment, similarly to that observed at Mars and comets. It is characterized by the direct interaction of the solar wind with the top of the ionosphere (see Figure 1.11). This leads to atmospheric escape processes, solar wind induced current systems and a complex nightside ionosphere consisting of tail rays, filaments, ionospheric holes and plasma clouds.

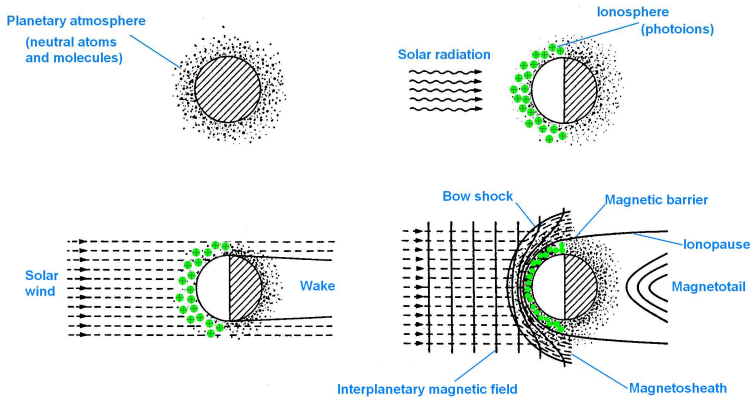


Figure 1.11: The neutral atmosphere of a planet without intrinsic magnetic field is ionized by solar radiation, resulting in the formation of an ionosphere which in turn acts as an obstacle to the solar wind. Consequently, the magnetized plasma flow is diverted around the conducting ionosphere so that the interplanetary magnetic field is draped over the planet producing a magnetic barrier on the dayside and inducing a magnetotail on the nightside. (Kivelson and Russell 1995)

Solar radiation ionizes the neutral atmosphere of Venus creating a substantial ionosphere. The upper boundary of the ionosphere, known as ionopause, is characterized by a sharp gradient in the electron density and forms at an altitude where the thermal plasma pressure of the ionosphere (nkT) equals the external pressure which is the sum of the solar wind dynamic pressure (ρv^2), its thermal pressure (nkT) and the magnetic pressure of the interplanetary magnetic field (B^2/μ_0). In general, the incident dynamic pressure is the largest component in the subsolar region but weakens towards the terminator region where the other two may become the dominant terms. The ionopause was found to be located about 300 km above the surface in the subsolar region and to have an altitude about 1000 km near the terminator at solar maximum (Phillips and McComas 1991).

Due to the supersonic and super-Alfvénic solar wind a bow shock is formed upstream

of the planet where the solar plasma flow is heated and slowed down. The region between the fast magnetosonic shock wave and the ionopause is called the magnetosheath, where an increased and turbulent magnetic field is observed. Since the interplanetary magnetic field (IMF) is frozen into the magnetosheath flow, it piles up at the dayside of the obstacle producing a so-called magnetic barrier (Zhang et al. 2008b) as it is carried around the planet. The solar wind plasma is significantly excluded from this region and the magnetic pressure dominates over the incident ram pressure. The IMF lines drape around the obstacle and as a result, create an induced magnetotail consisting of two lobes of opposite polarity separated by a plasma sheet (Luhmann and Cravens 1991). Observations revealed another boundary layer, located between the magnetosheath and the ionopause (see Figure 1.12), the so-called mantle region or transition zone, characterized by the presence of solar wind protons and planetary ions (Phillips and McComas 1991). Above the upper boundary of the mantle the shocked solar wind plasma is found whereas beyond the lower boundary of the mantle planetary ions become the main particle population (ion composition boundary).

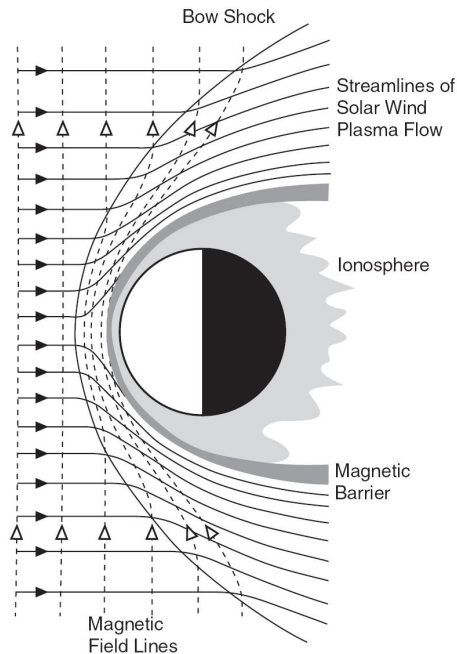


Figure 1.12: Schematic of the magnetosheath and magnetic barrier of Venus. (Zhang et al. 1991)

1.3 Observational history

For almost fifty years, planet Venus has been an attractive target in planetary space science and thus, was the focus of several space missions (from the Soviet Union and the United States) and ground based observations. Due to these observations it was possible to establish a basic description of the physical and chemical conditions existing in the atmosphere of Venus but also a lot of new puzzles did arise. One of the major and most interesting questions is why Venus has become such a hostile and exotic planet compared to Earth although both planets are similar in many respects. This overview regarding the previous spacecraft missions (see Figure 1.13) and their findings will only focus on the plasma environment and escape processes of Venus since it is the subject of this thesis.

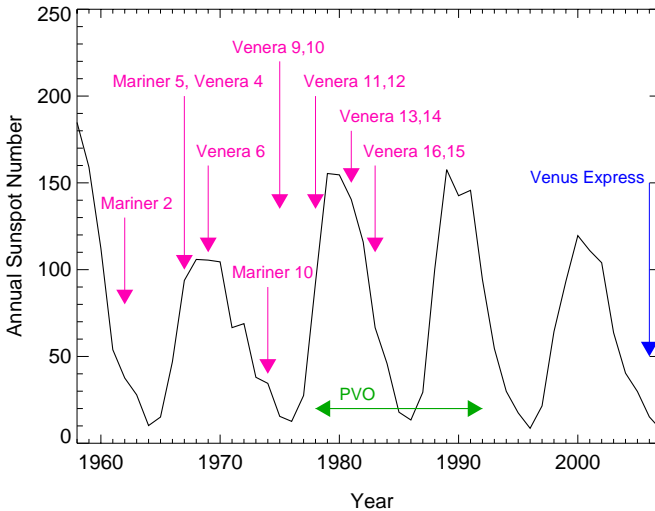


Figure 1.13: This plot shows the annual sunspot number from 1958 to 2007 and the dates of previous missions which contributed significantly to the current understanding of the plasma and electromagnetic environment of Venus. The current mission Venus Express was launched on 9 November 2005 and arrived at Venus on 11 April 2006.

The first successful attempt to investigate the solar wind interaction with Venus was made by the Mariner 2 spacecraft which flew by Venus on December 14, 1962. Closest approach was at 41000 km from the center of the planet, just sunward of the terminator plane (Phillips and McComas 1991). On the one hand, no planetary perturbation of the IMF was observed, neither from the magnetometer nor from the ion spectrometer, which led to the conclusion that Mariner 2 had never passed through a planetary bow shock. On

the other hand, the energetic particle experiment did not measure any energetic protons and electrons which would have suggested magnetospheric trapping. Thus, the conclusion of this mission was that the spacecraft had never entered a magnetosphere and that the planetary magnetic moment must be smaller than the terrestrial moment.

Five years later, Venera 4 was the next spacecraft to visit Venus and impacted the planetary nightside on October 18, 1967. Mariner 5 flew by just one day later, getting closer to within 4100 km from the planetary surface and approximately 2500 km from the optical shadow. Both missions contributed significantly to the global picture of the plasma environment of Venus due to their important observational discoveries such as the first observations of the planetary bow shock by magnetic field and plasma experiments. Moreover, Venera 4 found a low nightside ionospheric density as well as a lack of an intrinsic magnetic field. Also Mariner 5 concluded from their observations, like Mariner 2, that the planet does not possess a planetary magnetosphere due to the absence of energetic electrons and protons. Additionally, the radio occultation experiment onboard Mariner 5 detected a transition between solar and ionospheric plasmas, where the ion density dropped suddenly from near 10^4 cm^{-3} to values similar to those in interplanetary space. This boundary was called 'plasmopause' and is now known as ionopause. Another interesting discovery of the Mariner 5 spacecraft, obtained by $L\alpha$ airglow measurements via ultraviolet photometry, was the extended neutral exosphere, consisting of atomic and molecular hydrogen. Furthermore, the Mariner 5 particle and field instruments measured fluctuating magnetic fields within the magnetosheath and entered a region, just outside the optical shadow of the planet, which showed a magnetic field configuration that was almost aligned with the Sun-Venus line as well as low plasma density and flow speed. This was most probably the first direct observation of the induced magnetotail although its existence had not been unambiguously demonstrated by this mission.

The next spacecraft was Venera 6 and arrived at Venus on May 17, 1969. Nothing new was found by this mission but its measurements confirmed the existence of a magnetosonic shock wave in front of the obstacle which extended downstream from the planet.

The Mariner 10 spacecraft encountered Venus on February 5, 1974 on its way to Mercury. The bow shock was found to be closer to the planet than observed by the previous missions. Some scientists suggested that this variation maybe caused by changes in the composition of the ionosphere, solar wind speed or the IMF. All previous spacecraft visited Venus near solar cycle maximum while the Mariner 10 flyby was close to solar minimum. So other experimenters thought that it might be correlated with the variation of the solar wind pressure, since the ram pressure was higher for Mariner 10 than for Mariner 5. Although this mission provided the first observational suggestion that the above mentioned factors could be responsible for controlling the shock location, the modulation of the bow shock position by the solar cycle was suggested much later. Measurements made by the magnetometer detected intermittent field rotations and fluctuations which suggested multiple crossings between the downstream magnetosheath and a disturbed wakelike region. These observations led to the conclusion that field observation in the wake region is in disagreement with the earlier predictions either for a steady comet-like draping configuration or for a magnetotail based on an intrinsic magnetic field. Moreover, the plasma instrument onboard Mariner 10 found a depletion of energetic electron density within the magnetosheath. This was explained by depleted and compressed magnetic flux tubes as a result of passing near the ionopause. In the downstream region the plasma

instrument discovered regions of low plasma density and speed with observable magnetic fluctuations as well as regions of high density and speed in magnetically quieter regions. The former regions were suggested to be related with plasma instabilities generated by pickup of planetary ions, while the latter were associated with a viscous interaction between solar and planetary plasmas.

After Mariner 10, the twin orbiters Venera 9 and Venera 10 arrived at Venus on October 22 and October 25, 1975, respectively and contributed significantly to the knowledge of solar wind-atmosphere interaction at Venus. Both spacecraft attained a pericenter of about 1600 km, an apocenter near 113 000 km and had 48 hour periods. First of all, Venera 9 and 10 magnetic field observations detected a steady magnetotail with two lobes of opposite polarities and thus, confirmed the theory of a comet-like draping configuration. Owing to both orbiters, it was also possible for the first time to map systematically the planetary bow shock which revealed an asymmetric shock location due to the different velocities of magnetohydrodynamic waves propagating parallel and perpendicular to the magnetic field. In other words, the shock location varies with the clock angle which is defined by the projection of the IMF field vector onto the terminator plane (Russell et al. 2006). Thus, the bow shock was found to be farther away from the planet for magnetic fields nearly perpendicular to the flow because in this direction the velocity of the fast wave is greatest. As a consequence, the shocked plasma is less compressed and requires a greater volume in order to be deflected around the planet. Furthermore, the wide-angle plasma experiments onboard Venera 9 and 10 provided important insights into the plasma properties of the terminator and near wake region of Venus. The investigators found a stable electron population and barely observable ion fluxes extending 3-4 R_V downstream from the planet in a region which they called umbra. This umbra was encircled by a so-called penumbra (nightside magnetosheath) which exhibited less dense, slower and hotter plasma than in the dayside magnetosheath. The narrow-angle electrostatic plasma experiments were responsible for the investigation of the nightside interaction region. The data indicated the existence of a so-called boundary layer (or rarefaction region) which contained a mixture of solar and planetary particles and extended as far as 5 R_V downstream from Venus.

On December 4, 1978 encountered Pioneer Venus Orbiter (PVO) the planet, provided a huge data set over 14 years and contributed decisively to our current knowledge of the plasma environment of Venus. Here I will only mention the different topics of research which were done based on PVO measurements, since a detailed description of the solar wind-atmosphere interaction at Venus is given in Section 1.2.4. Due to the fact that PVO was able to carry out measurements over more than a complete solar cycle, it was possible to confirm some of the theories which were based on measurements provided by the previous missions. One of these milestones was the fact that the bow shock and the ionopause offer solar cycle effects and asymmetries ordered by the IMF as was already suggested by Mariner 10 and Venera 9, 10 observations. The bow shock, the ionopause and the magnetotail could be systematically mapped and described. Furthermore, the complexity of the nightside and near-terminator ionosphere and the possible ionization sources had been investigated. PVO also provided measurements of the flow field and magnetic characteristics of the magnetosheath. Additionally, the picked up planetary ions in the near-planet magnetosheath and in the downstream region were identified. Last but not least, the extended exosphere of suprathermal oxygen were analyzed. Unfortunately, PVO was not

able to carry out observations in the region 2-6 R_V downstream of the planet and thus, did not improve our knowledge about the tail region. Accordingly, the question, how the deep tail is connected to the near-planet environment remained unknown after the PVO mission. Also due to the orbital sampling bias, it was impossible to investigate the subsolar shock region, especially the ionosphere, as well as the near-Venus plasma environment during solar minimum (Russell et al. 2006).

During the period of PVO, also Venera 11 through 16 visited Venus. However, based on their observations we did not gain a lot of new insights into the understanding of the solar wind-atmosphere interaction. 1978 Venera 11 and 12 entered the orbit of Venus and provided only improved photometry measurements of the $L\alpha$ airglow and exospheric modeling based on these observations. Venera 13 and 14 arrived at Venus 1981 but unfortunately did not lead to new knowledge of the plasma environment. 1983 Venus was encountered by Venera 15 and 16 which resulted in new data on the ionosphere in the decreasing part of the solar cycle.

1.4 Venus Express mission

Although we owe most of our current knowledge of the solar wind interaction with Venus to the long lasting Pioneer Venus Orbiter (PVO) mission (1978-1992), providing observations over more than a complete solar cycle, a lot of questions remain unanswered. Venus Express (VEX) is the first European mission to visit planet Venus and is the sister mission of Mars Express (MEX) which is in orbit around Mars with a similar set of instruments. The VEX spacecraft design is based on that of MEX but of course with some necessary modifications, which for example are correlated with the four times higher flux at Venus than at Mars.

The VEX mission aims at a global investigation of the atmosphere and the plasma environment of Venus and addresses several important aspects of the geology and surface physics. The basic idea of this mission is to observe from orbit the same target with different instruments at the same time. This provides a comprehensive, versatile and complete view of the different phenomena taking place on Venus. The key questions and scientific objectives are related to the global atmospheric circulation, the atmospheric chemical composition and its variations, the surface-atmosphere physical and chemical interactions including volcanism, the physics and chemistry of the cloud layer, the thermal balance and role of trace gases in the greenhouse effect, the origin and evolution of the atmosphere, and the plasma environment and its interaction with the solar wind (Svedhem et al. 2007). A better understanding of the above mentioned key issues could provide an answer to the most fundamental question, why Venus is so different from the Earth, although both planets are similar in size, density and distance from the Sun.

On 9 November 2005 VEX was successfully launched by a Soyuz-Fregat rocket, from the Baikonur Cosmodrome in Kazakhstan. After a five-month interplanetary journey to the inner solar system, the spacecraft arrived at its destination on 11 April 2006 and was captured by the Venusian gravity. VEX has a highly elliptic polar orbit (see Figure 1.14) with a 24-hour period and thus, enables high spatial resolution observations as well as global observations. The pericentre altitude is maintained between 250 and 400 km with pericentre latitude at 78° (above the North pole) and the apocentre altitude

is near 66 000 km. Owing to this sampling geometry, we are now able to investigate two important regions, namely the low altitude terminator region and mid-magnetotail at about $4 R_V$, which were not covered by the PVO mission. These regions are important in order to understand the plasma transport from the dayside to the nightside and thus, to understand how the nightside ionosphere and wake are formed.

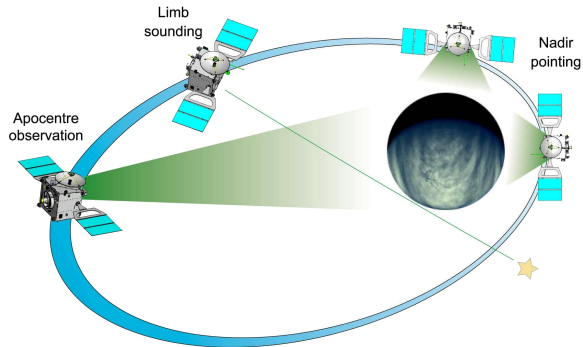


Figure 1.14: Venus Express orbit around Venus and its different observation modes. © ESA.

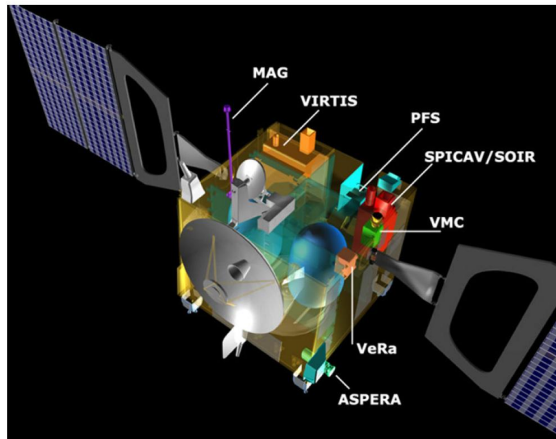


Figure 1.15: The locations of the seven scientific instruments on the Venus Express spacecraft. © ESA.

The VEX payload consists of the following scientific instruments (see Figure 1.15):

- ASPERA-4 (Analyser of Space Plasma and Energetic Atoms),
- PFS (Planetary Fourier Spectrometer, currently not operating),
- SPICAV/SOIR (Ultraviolet and Infrared Atmospheric Spectrometer),
- VeRa (Venus Express Radio Science Experiment),
- VIRTIS (Ultraviolet/visible/near-infrared Mapping Spectrometer),
- MAG (Magnetometer) and
- VMC (Venus Monitoring Camera).

The first five listed above are inherited from the MEX and Rosetta missions with some minor changes and the last two units, namely MAG and VMC, have been specifically developed for the VEX project (Svedhem et al. 2007).

The plasma experiment ASPERA-4 is responsible for the detection and characterization of the neutral and charged particles existing in the Venus plasma environment. This instrument is described in more detail in Section 2.1 since it is the focus of this thesis.

PFS is a high-resolution IR Fourier spectrometer and is designed for studying the mesosphere (60-100 km) and the upper cloud layer of the planet. But unfortunately, the instrument is currently not operating because its entrance mirror got stuck and PFS could not be put into proper operation.

SPICAV/SOIR is an ultraviolet and infrared spectrometer for stellar and solar occultation measurements and nadir observations. Its main scientific targets are to provide vertical profiles of atmospheric density and temperature in the altitude range from 70 to 180 km (upper atmosphere: mesosphere and lower thermosphere) and vertical profiles of the haze above the clouds and the microphysical properties of aerosols. In order to learn more about the mesospheric composition and chemistry, SOIR measures the main trace gases, such as HDO, SO₂, COS, CO, HCL, HF, and searches for new trace gases such as, hydrocarbons (CH₄, C₂H₂, etc.), nitrogen oxides (NO, N₂O, etc.) and chlorine-bearing compounds (CH₃Cl, ClO₂). These observations will contribute to solve the problem of atmospheric evolution and thus, the question of water escape.

The prime task of the radio-science experiment VeRa is to provide vertical profiles of the density and temperature in the altitude range from 40 to 100 km in order to analyse the vertical structure of the atmosphere and ionosphere. But VeRa also studies surface properties, the gravity field, the interplanetary medium and the electron density profile from about 80 km up to 600 km (ionopause).

VIRTIS is a visible and near-IR imaging and high-resolution spectrometer which has several important scientific goals. This instrument studies the composition of the lower atmosphere by measuring weak night-side emissions in the spectral 'windows' of the cloud layer and analyses the cloud structure, composition and scattering properties. Moreover, VIRTIS is suitably equipped for cloud tracking in the UV and IR as well as for the retrieval of the vertical field of wind velocities in order to investigate the atmospheric dynamics. Furthermore, it is carrying out temperature mapping of the surface in order to detect hot

spots related to possible volcanic activity. Additionally, VIRTIS searches for lightning, seismic wave activity and for variations related to surface/atmosphere interaction.

The Magnetometer (MAG) onboard VEX measures the magnetic field magnitude and its direction. The principle scientific objectives of MAG are to define the plasma boundaries at Venus and to study the solar wind-atmosphere interaction. MAG maps the magnetic field in the magnetosheath, the magnetic barrier, the ionosphere and the magnetotail with high temporal resolution. Furthermore, the instrument detects the strength and occurrences of electromagnetic waves which are associated with any atmospheric discharges in order to contribute to the understanding of Venus lightning. Additionally, the MAG data provide important information to other instruments onboard the spacecraft, e. g. ASPERA, for any combined studies of the Venus plasma environment (Zhang et al. 2006).

The main scientific goals of the wide-angle camera VMC are the investigation of the atmospheric dynamics at the cloud tops (~ 70 km altitude), the identification of the unknown UV absorber, the study of the circulation of the thermosphere in the altitude range of 100-130 km, the search for lightning and the investigation of the surface brightness temperature in order to search for hot spots (volcanic activity). One of the fundamental questions, which VMC tries to answer, is the mechanism of the super-rotation and the polar vortices.

Although VEX covers a wide range of scientific objectives, enhancing our knowledge about Venus, still some topics are left for future missions: such as the chemistry of the lower atmosphere, the abundance of noble gases and isotopes, the microphysics of the clouds and surface geology as well as the interior of the planet. However, the VEX data will play an important role for planning new missions which may also carry landers, balloons or other aerobots.

1.5 Motivation and open questions

Our knowledge of the Venusian plasma environment has significantly improved in the past 20 years mainly due to the long lasting PVO mission providing a large dataset including low and high solar activity periods. However, many unresolved and interesting issues remain open and several of these unanswered questions are currently addressed by the VEX mission as discussed in the previous section.

This work deals with the investigation of the global plasma environment of Venus by using ASPERA-4 data and comparing with 3D hybrid simulations in order to contribute to the following issues:

- What is the nature of the plasma boundaries around Venus? Can these ion boundaries be described by simple functions?
- Do the interaction regions and boundaries determined by ASPERA-4 at low solar activity coincide with those identified primarily by the magnetic field data obtained by PVO?
- What is the correlation of the bow shock and magnetic barrier region determined by the magnetic field data from the Magnetometer onboard VEX with the ion boundaries established by the ion and electron data from ASPERA-4 instrument?

- Does the terminator shock distance exhibit solar cycle variations? Is the bow shock location sensitive to changes in the upstream dynamic pressure of the solar wind?
- Is an induced magnetic field needed for pressure balance?
- What are the planetary ion loss rates from the planet into space? What are the escaping ion species? Are the locations of plasma boundaries important for the escape?
- Can the hybrid model contribute to the understanding of the escape mechanisms induced by the solar wind at Venus? How good is the concordance of the escape fluxes derived from the hybrid simulations with the estimated ion loss rates obtained by observations, theoretical models and other numerical approaches?
- How important are the loss processes for the atmospheric history? Where did the water go?

Of course not all of these questions are answered by this study but will help to solve this issues.

The work is organized as follows. Chapter 2 describes the basics of the ion and electron sensor of the ASPERA-4 experiment and the structure of the 3D hybrid model. The first half of Chapter 3 deals with our identification of the plasma boundaries based on ASPERA-4 measurements and the dependency of the terminator shock distance on the solar wind ram pressure as well as on the solar EUV flux closing with a discussion of this data analysis. In the second half the simulation results carried out for different solar wind conditions based on VEX and PVO observations are analyzed and compared with each other at the end of this chapter. The comparison between the plasma and magnetic field data extracted from the simulation with the ASPERA-4 and MAG observations along the VEX spacecraft trajectory is given in Chapter 4. Moreover, the atmospheric escape rates of oxygen are discussed in the last section. A summary and the conclusions are given in Chapter 5. Finally, this study closes with an outlook for future investigations.

2 Method

Since this thesis deals with a comparison between the data analysis of the ASPERA-4 experiment with the results of 3D hybrid code simulation in order to investigate the global plasma environment of Venus, I will summarize some basic facts about the electron and ion sensors onboard VEX and the 3D hybrid model in this chapter. A detailed description of the ASPERA-4 instrument and simulation code is given by Barabash et al. (2007b) and Bagdonat and Motschmann (2002b), respectively.

2.1 The ASPERA-4 instrument

The “Analyzer of Space Plasmas and Energetic Atoms” (ASPERA-4) onboard the VEX spacecraft is a copy of the ASPERA-3 experiment included in the MEX project. It is a comprehensive plasma diagnostic package which measures energetic neutral atoms (ENAs), electrons and ions with a wide angular coverage in order to investigate the solar wind-atmosphere interaction and to characterize the plasma and neutral gas environment in the near-Venus space. Furthermore, ASPERA-4 was designed to (1) characterize quantitatively the impact of plasma processes on the atmosphere, (2) determine the global plasma and neutral gas distributions, (3) study solar wind induced atmospheric escape, (4) investigate energy deposition from the solar wind into the ionosphere and erosion of the ionosphere, and (5) provide undisturbed solar wind parameters. The background of all these studies addresses the fundamental question: why Earth, Mars and Venus have undergone such different thermal and atmospheric evolutions? The Earth’s atmosphere has always been protected by its intrinsic magnetic field against solar wind induced erosion processes. Mars has cooled faster than Earth and Venus, and its internal magnetic field disappeared around 500 million years after the formation of the planet. Consequently, its atmosphere has become almost completely eroded by the solar wind. Venus does not possess a global magnetic field and probably never did. However, due to its higher gravity, the Venusian atmosphere was not eroded as compared to Mars. The atmosphere is extremely dense and contains only very little water (30 ppm). How the water has been lost at Venus is one of the central questions ASPERA-4 tries to answer.

The ASPERA-4 instrument consists of two units, the Main Unit (MU) and the Ion Mass Analyzer (IMA). The location of MU and IMA on the VEX spacecraft are shown in Figure 2.1. The MU comprises four sensors (see Figure 2.2), namely, two Neutral Particle Detectors (NPD1 and NPD2), a Neutral Particle Imager (NPI) and an Electron Spectrometer (ELS) as well as a digital processing unit (DPU). All these components are located on a turnable platform (scanner). A 4π maximum coverage is achieved by the combination of 360° sensor field of view (FOV) (180° for NPDs) and the scans from 0°

to 180°. However, a part of the FOV is blocked by the spacecraft body so that the real coverage depends on the instrument location on the spacecraft. The MU also houses the electronics for operations and data handling while IMA has its own electronics package.

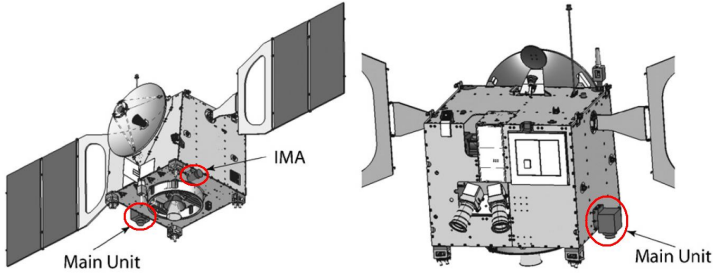


Figure 2.1: The accommodation of the Main Unit and Ion Mass Analyser on the Venus Express spacecraft.

The NPDs perform measurements of the ENA flux, resolving velocity (0.1-10 keV) and mass (hydrogen and oxygen) with a coarse angular resolution. The NPI provides measurements of the integral ENA flux (0.1-60 keV) with no mass and energy resolution but relatively high angular resolution. The ELS performs electron energy measurements and IMA provides measurements of the main ion components (H^+ , He_2^+ , He^+ , O^+ and heavier ions). Table 2.1 summarizes the performances of the electron and ion sensors which are described in more detail in the following subsections. No further details will be given for NPI and NPD since only ELS and IMA data are used in the thesis.

Parameter	ELS	IMA
Particles to be measured	Electrons	Ions
Energy	5 eV - 20 keV	10 eV - 36 keV
Energy resolution, $\Delta E/E$	0.07	0.07
Mass resolution	–	$m/q = 1, 2, 4, 8, 16, 32, > 40$
Intrinsic field of view	$4^\circ \times 360^\circ$	$90^\circ \times 360^\circ$
Angular resolution, FWHM	$4^\circ \times 22.5^\circ$	$4.5^\circ \times 22.5^\circ$
G-factor/pixel, $cm^2 sr$	7×10^{-5}	3.5×10^{-4}
Efficiency, %	Incl. in G-factor	Incl. in G-factor
Time resolution (full 3D), s	4	192
Mass, kg	0.3	2.4

Table 2.1: The performance of the Electron Spectrometer and Ion Mass Analyzer.

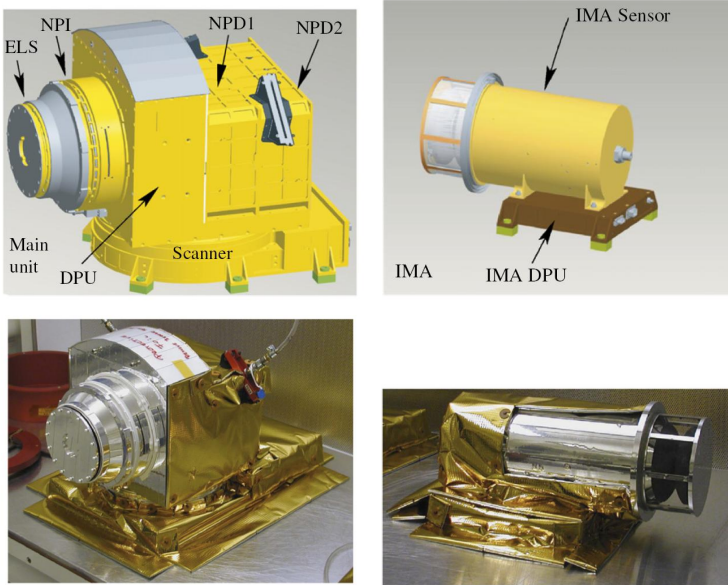


Figure 2.2: The overall configuration of the ASPERA-4 experiment.

2.1.1 Electron Spectrometer (ELS)

The ELS sensor consists of a spherical top-hat electrostatic analyzer (ESA) and two concentric hemispherical electrodes. A cross section of the ELS sensor is shown in Figure 2.3. The charged particles can enter the top-hat at any angle in the plane of incidence. The electrons are then deflected through the central hole in the outer hemisphere by a positive voltage applied to the inner hemisphere and are filtered in energy by the electric field between the hemispheres. Then, the electrons are detected and recorded by a micro-channel plate (MCP). Behind the MCP, they hit one of the 16 anodes where each anode defines a 22.5 degree sector of the incident azimuth angle.

Electrons with energies up to 20 keV/q are measured with a high energy resolution. By means of varying the electrostatic potential between the analyzer plates, the energy of the electrons selected by the filter can be changed. The plate voltage, divided into 128 steps, is swept once every 4 seconds which determines the energy channels of ELS. Since ELS is mounted on the main unit, full 3D electron measurements are possible, if the mechanical scanner is in operation. But this is only the case on some nightside passes.

The ELS sensor was constructed to be insensitive to UV light so that it can operate even when it is looking directly to the Sun. However, ELS is sensitive to photoelectrons which are created by UV light hitting the spacecraft surface. Hence, one must avoid a pile-up of these charged particles (originating from spacecraft charging) at the entrance

of the sensor in order to impede saturation of the counters. This is achieved by applying a negative deflection voltage of around 5-6 eV at the top-hat exit above the MCP. Consequently, low energy electrons below 5-6 eV are reflected and cannot be measured by ELS (e. g., low energy electrons of the ionosphere).

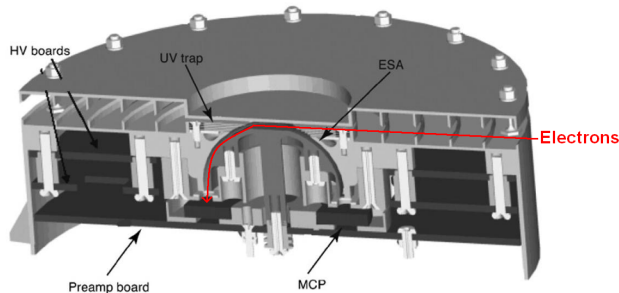


Figure 2.3: A cross section of the Electron Spectrometer.

2.1.2 Ion Mass Analyser (IMA)

The IMA sensor can perform ion energy spectroscopy and ion composition analysis at the same time. That means, IMA determines the mass per charge (M/q) and energy per charge (E/q) of ions with 1-80 amu/ q and 0.01-36 keV/ q . A schematic of the ion sensor is presented in Figure 2.4.

The incoming ions enter the sensor through an outer grounded grid and reach the deflection system. This entrance system consists of two curved, charged plates with changing voltages in order to vary the incident polar angle of the ions. That means, the angle of the deflected ions depends on the voltage applied to the deflector electrodes. Thus, a full 3D coverage is achieved every 192 seconds by electrostatic sweeping of the polar angle from -45° up to $+45^\circ$ over 16 steps.

The next station for the ions is the top-hat electrostatic analyzer (ESA) which comprises two concentric hemispheres with a variable electric field between them so that the ions are filtered in energy per charge. Then, the surviving ions pass through the magnetic separation section where permanent magnets deflect the ions along different trajectories, depending on their mass per charge. Leaving the magnetic mass analyzer, the ions impact a MCP. The electrons which exit the MCP are detected by an imaging anode system composed of 32 concentric rings and 16 sectors. This system determines both the mass per charge (mass rings) and the azimuth (sector) of the incoming ions. A negative voltage can be applied between the ESA exit and the magnetic separation entrance in order to accelerate light ions at low energies. For instance, H^+ ions would not reach the MCP without this acceleration because their gyroradius is too small.

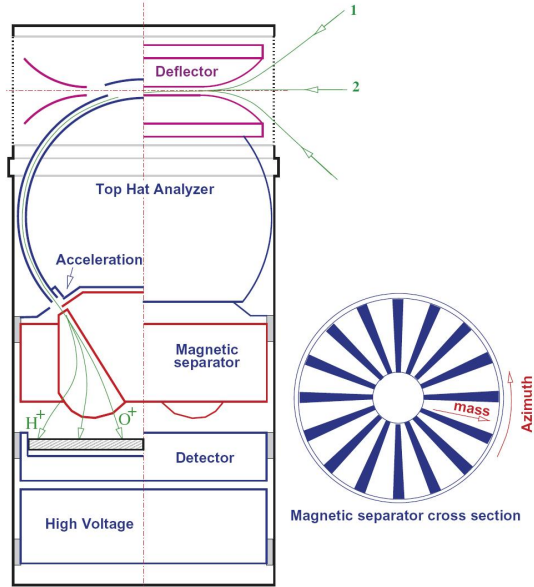


Figure 2.4: A cross section of the Ion Mass Analyzer (left) with examples of the ion trajectories, and magnet separator (right).

2.2 Simulation code

The results of the data analysis are compared with numerical simulations by means of a 3D hybrid model which has been originally developed by Bagdonat and Motschmann (2002a,b) to study the solar wind interaction with comets. Furthermore, the present version of this hybrid code has already been successfully applied for modeling the solar wind interaction with magnetized asteroids (Simon et al. 2006a), for studying the plasma environment of Mars (Böβwetter et al. 2004, 2007) and Titan (Simon et al. 2006b, 2007), as well as for the simulation of Rhea’s magnetospheric interaction (Roussos et al. 2008).

In the hybrid model the ions are treated as individual particles moving in self - consistently generated electromagnetic fields, whereas the electrons are modeled as a massless ($m_e = 0$) charge-neutralizing fluid. In the following subsections the main basic features of the model are explained. A more detailed description of the code can be found in the studies mentioned before.

The hybrid code is written in the computer language C. The simulations are performed on linux based AMD Opteron single-core computers with 16 GB ram and 2.4 GHz CPU frequency. Typical computing times for the VEX based simulation runs (solar minimum conditions) were almost 3 months in order to achieve a quasi-stationary state. In the case

of PVO based simulation runs representing solar maximum conditions, the computing time would be more than 6 months in order to reach the same level of quasi-stationary state due to higher ion production rates.

2.2.1 Basic equations

As already mentioned, the ions are treated as individual particles in order to cover ion dynamics. Hence, the code solves the equation of motion for the ions:

$$\frac{d\vec{x}_s}{dt} = \vec{v}_s \quad (2.1)$$

and

$$\frac{d\vec{v}_s}{dt} = \frac{q_s}{m_s}(\vec{E} + \vec{v}_s \times \vec{B}) - k_D n_n (\vec{v}_s - \vec{u}_n) \quad (2.2)$$

where q_s , m_s , \vec{x}_s and \vec{v}_s are the charge, mass, position and velocity of an individual particle of species s , respectively; whereas \vec{E} and \vec{B} are the electromagnetic field quantities. The first term on the right in Equation 2.2 expresses the Lorentz term and the second the drag force, which takes into account collisions of ions and neutrals (k_D is a constant taken from Israelevich et al. (1999)). n_n and \vec{u}_n are the number density and bulk velocity of the neutrals. We use $\vec{u}_n = 0$.

The electron fluid description is based on the momentum equation

$$0 = n_e m_e \frac{d\vec{u}_e}{dt} = -en_e(\vec{E} + \vec{u}_e \times \vec{B}) - \nabla P_{e,sw} - \nabla P_{e,hi} \quad (2.3)$$

and by using Ampere's law

$$\nabla \times \vec{B} = \mu_0 \vec{j} = -en_e \vec{u}_e + en_i \vec{u}_i \quad (2.4)$$

one can derive the electric field

$$\vec{E} = -\vec{u}_i \times \vec{B} + \frac{(\nabla \times \vec{B}) \times \vec{B}}{\mu_0 en_e} - \frac{\nabla P_{e,sw} + \nabla P_{e,hi}}{en_e} \quad (2.5)$$

where \vec{u}_i denotes the mean ion velocity. The mean ion density (n_i) is equal to the electron density (n_e) due to the assumption of quasi-neutrality.

We are using two different electron pressure terms in order to consider the different electron temperatures in the solar wind and ionosphere, respectively. Both electron populations are assumed to be adiabatic, i. e.

$$P_{e,sw} = \beta_{e,sw} \left(\frac{n_{e,sw}}{n_0} \right)^\kappa \quad (2.6)$$

$$P_{e,hi} = \beta_{e,hi} \left(\frac{n_{e,hi}}{n_0} \right)^\kappa \quad (2.7)$$

where κ is the adiabatic exponent which has a value of $\kappa=2$ instead of $5/3$, because the thermodynamic coupling is only effective in the two dimensions perpendicular to the field (Böbwegger et al. 2004).

Finally, the set of hybrid equations is completed by Faraday's law

$$\frac{\partial \vec{B}}{\partial t} = \nabla \times (\vec{u}_i \times \vec{B}) - \nabla \times \left[\frac{(\nabla \times \vec{B}) \times \vec{B}}{\mu_0 en_e} \right] \quad (2.8)$$

expressing the time evolution of the magnetic field.

2.2.2 Basic scheme

The basic principles of the numerical techniques which are used to solve the set of hybrid equations are shortly described in this section. A detailed discussion can be found in the thesis of Bagdonat (2005).

The simulation code uses a Particle-in-cell (PIC) method for solving the set of hybrid equations mentioned in the previous section 2.2.1. A detailed description of the PIC code is given by Birdshall and Langdon (1985). Figure 2.5 shows the basic idea of the PIC code which requires a fixed grid defined in coordinate space. The electric and magnetic fields as well as the charge and current densities are defined only at the grid nodes whereas the individual particles can be located anywhere inside the grid cells.

First of all, the electromagnetic fields at the individual particle positions are needed for solving the equation of motion for each particle. Then, these field quantities are interpolated from the grid nodes back onto the position of the particles. In the next step, the forces acting on the particles are calculated. Finally, the individual particles are moved in the simulation grid.

Figure 2.6 demonstrates the four basic steps which are carried out in each computational time step Δt . These are:

1. **Collection of moments:**

By using the positions and velocities of the individual particles, the charge and current densities are calculated for each node of the simulation grid.

2. **Calculation of field equations:**

The field equations 2.5 and 2.8 are solved by means of the charge and current densities obtained in the first step, resulting in an updated electric and magnetic field vector for each grid node.

3. **Interpolation of forces:**

For each particle the electromagnetic field quantities are interpolated from the grid point positions to the particle position.

4. **Movement of particles:**

The equations 2.1 and 2.2 are solved using the electric and magnetic field at the individual particle position, resulting in an updated position and velocity of the particle.

2.2.3 Curvilinear Grid

The simulation is applied to a curvilinear grid in three spatial dimensions which allows high spatial resolution in the vicinity of the planetary atmosphere. This non-orthogonal fisheye-grid is obtained from an equidistant Cartesian grid by modifying the radial distance of the grid points from the center of the coordinate frame. A detailed description of the grid generation is given by Bößwetter et al. (2004) and Simon et al. (2006b).

For the simulations presented in this thesis the box size was chosen to be $6 R_V$ with 101 grid cells in each spatial direction. By using this grid one obtains a spatial resolution of about 100-150 km per grid cell in the vicinity of the obstacle. Beyond the distorted grid (equidistant cartesian grid) a resolution of 250-300 km per grid cell is achieved.

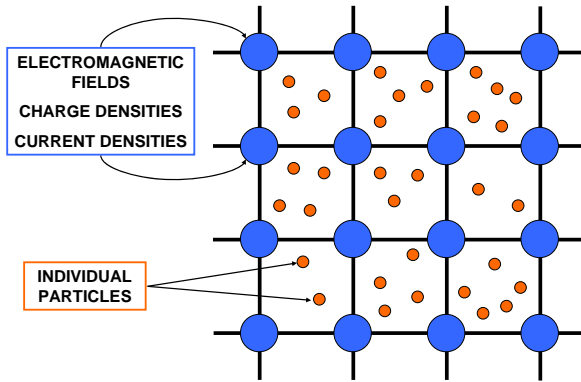


Figure 2.5: This sketch shows the basic idea of the Particle-in-cell (PIC) method which solves the set of hybrid equations. A fixed grid is defined in coordinate space. The electromagnetic quantities as well as the charge and current densities are calculated only on the grid nodes (blue) whereas the individual particles (orange) can move anywhere in between.

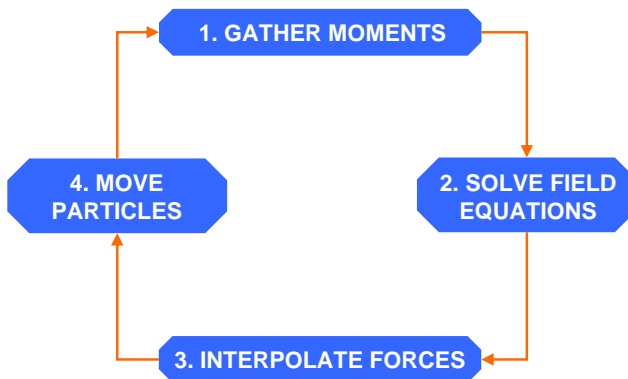


Figure 2.6: Each computational cycle is composed of these four basic steps which are carried out by a Particle-in-cell (PIC) code.

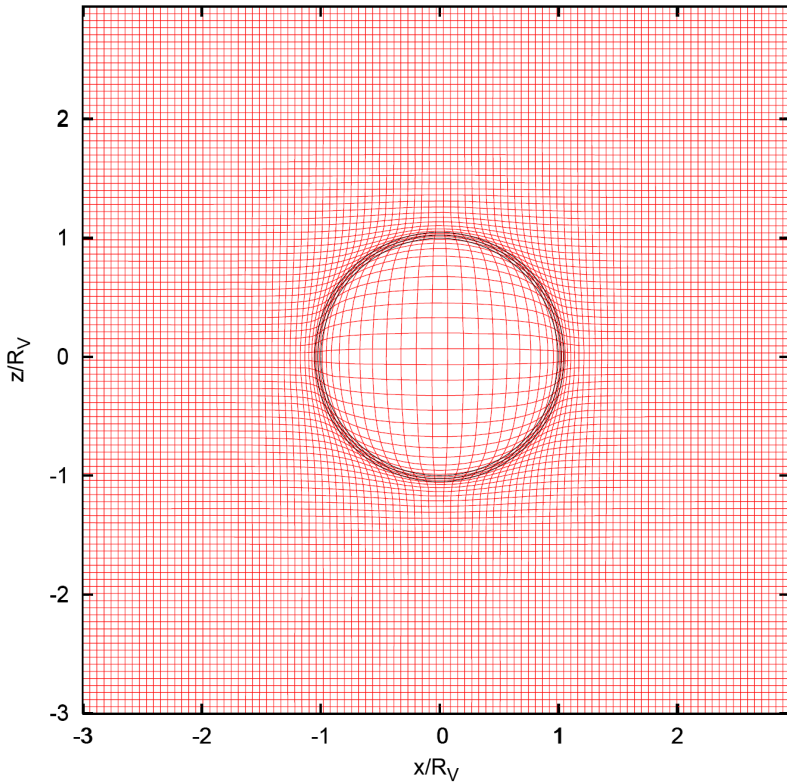


Figure 2.7: Curvilinear simulation grid (fisheye-grid). The black inner circle marks the surface of the planet, whereas the middle and the outer circles depict 150 km and 300 km above the surface, respectively.

2.2.4 Boundary conditions

It turned out that the boundary conditions imposed on the outer boundaries of the cubic simulation box, the inner boundary of the simulation (spherically shaped obstacle) and the interior of the planet are a critical issue in order to keep the simulation numerically stable.

The 3D model uses “inflow” and “outflow” boundary conditions for the outer borders of the simulation box. The solar wind comes in at the left side of the box (inflow boundary) and leaves the simulation domain at the right side (outflow boundary). For the remaining edges some sort of free or absorbing boundary is desirable, but that turned out

to make the simulation unstable. Thus, inflow boundary conditions have been chosen for the remaining “walls” of the box which simply keep constant values.

The inner restriction of the simulation box is located 150 km above the planetary surface and has a spherical shape marking the simulated lower border of the Venusian ionosphere. Solar wind protons as well as planetary ions hitting this inner boundary are removed from the simulation. This absorbing boundary condition is in a sense a disadvantage for the simulation because it represents a sink for the particles and hence, also for energy. However, this condition is not completely unrealistic since the simulation does not consider any recombination process or other chemical processes.

The interior of the planet is modeled by means of an assumed artificial inner ion density which is increased while the simulation proceeds. This inner density profile is a good approximation to the surrounding ionospheric (heavy ion) density profile and shows a relatively good agreement at least in the subsolar region. Consequently, strong electric fields arising from density gradients are avoided which rapidly would make the simulation unstable.

However, no boundary conditions are imposed on the electromagnetic fields, which means, the equations for \vec{E} and \vec{B} are solved at the grid nodes outside as well as inside of the obstacle. This implies that the magnetic field can penetrate through the interior of the planet by dint of numerical diffusion effects which is of course only a very rough approximation to the real situation, where the fields are deflected around the ionosphere.

2.2.5 Simulation geometry

In each computational cycle, the simulation code calculates the field quantities on a three dimensional grid. However, for discussing and analyzing the 3D simulation results, given in section 3.2, it is more convenient to visualize the results in two dimensional cuts through the simulation box along the terminator ($x=0$), polar ($y=0$) and equatorial ($z=0$) plane. Figure 2.8 shows an ideal simulation geometry, where the solar wind flows in the positive x -direction, the background magnetic field (perpendicular to the plasma flow) points in the positive y -direction and thus, the convection electric field ($\vec{E} = -\vec{v} \times \vec{B}$) completes the right-handed system pointing in the negative z -direction (southward). But when IMF is antiparallel to the y -axis, the solar wind electric field is orientated along the positive z -axis (northward). For practical reasons in discussing the simulation results I denote the hemisphere to which the solar wind electric field is pointing as the E^+ hemisphere (southern hemisphere) and the other as E^- hemisphere (northern hemisphere) like for the situation shown in Figure 2.8.

The size of the simulation box in each spatial direction is $-3R_V \leq x, y, z \leq 3R_V$ for all simulation runs presented in section 3.2 which is an appropriate size for the investigation of the near-plasma environment of Venus. R_V denotes the radius of Venus which is 6051.8 km. The planet is always located in the middle of the simulation box.

Since ASPERA-4 data are compared with simulations in section 4, it is important to note here that the simulation (SIM) coordinate system is different from the Venus-Sun-Orbit (VSO) system used in literature and measurements. The positive x -axis points away from the Sun in SIM while it points to the Sun in VSO. The positive y -axis in SIM points into the direction of orbital motion while in VSO it is orientated opposite to the planet’s orbital motion. The positive z -axis is orientated out of the ecliptic plane pointing North

in both coordinate systems.

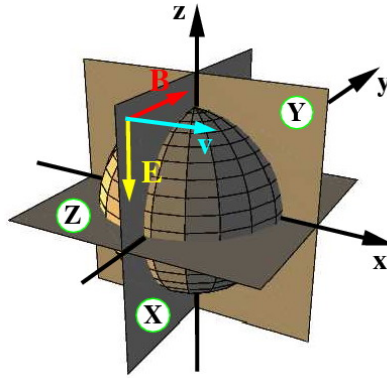


Figure 2.8: Cross sections of the simulation box at the plane $X=0$ (terminator plane), $Y=0$ (polar plane) and $Z=0$ (equatorial plane). The undisturbed solar wind flows in the positive x -direction, the convection electric field ($\vec{E} = -\vec{v} \times \vec{B}$) points in the negative z -direction and the background magnetic field completes the right-handed system pointing in the positive y -direction.

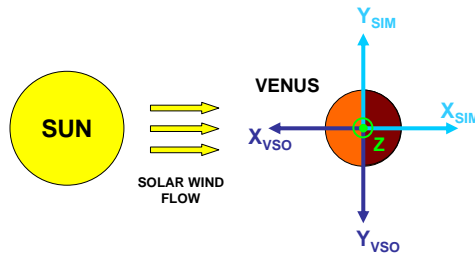


Figure 2.9: Simulation (SIM) coordinate system vs. Venus-Sun-Orbit (VSO) coordinate system. The positive x -axis points away from the Sun in SIM while it points to the Sun in VSO. In SIM the positive y -axis points into the direction of orbital motion while in VSO it is orientated opposite to the planet's orbital motion. The positive z -axis is orientated out of the ecliptic plane pointing North in both coordinate systems.

2.2.6 Modeling the atmosphere of Venus

The Venusian atmosphere is modeled as a spherically symmetric gas cloud around the planet consisting of atomic oxygen which is the dominant neutral in the upper atmosphere above around 150 km, as already mentioned in subsection 1.1.5. The radial density distribution includes atmospheric and exospheric exponential profiles. The profile for the cold oxygen is based on the model from Kulikov et al. (2006) and the hot oxygen profile is based on PVO measurements compared with model calculations obtained by Nagy et al. (1990). Both density profiles are shown in Figure 2.10. The cold oxygen densities are neutral O atoms existing in the Venusian atmosphere below ~ 400 km altitude. The hot oxygen densities are excited O^+ atoms existing in the exosphere which gained excess energy via photochemical reactions or collisions (see subsection 1.1.7) populating the corona up to 6000 km above the surface.

In order to reproduce the atmospheric profile of oxygen as accurate as possible, three exponential terms with different scale heights (H_1, H_2, H_3) are used in the neutral gas profile (cold and hot oxygen):

$$n_n(r) = n_1 \cdot \exp\left[\frac{(r_1 - r)}{H_1}\right] + n_2 \cdot \exp\left[\frac{(r_2 - r)}{H_2}\right] + n_3 \cdot \exp\left[\frac{(r_3 - r)}{H_3}\right] \quad (2.9)$$

The number densities n_1, n_2 and n_3 correspond to the reference heights r_1, r_2 and r_3 , respectively. This neutral profile which is constant in space and time, also acts as a decelerator of the solar wind protons and planetary ions in the collision term of equation 2.2.

The heavy planetary oxygen ions are incorporated into the simulation by means of a so-called Chapman production function, that means, the local ion production rate q depends on the altitude above the surface (r) as well as on the solar zenith angle (χ).

$$q(r, \chi) = \frac{\partial n_i(r, \chi)}{\partial t} = \nu k n_n(r) \cdot \exp\left\{-\frac{\sigma}{\cos(\chi)} \left[n_1 H_1 \cdot \exp\left(\frac{(r_1 - r)}{H_1}\right) \right. \right. \quad (2.10)$$

$$\left. \left. + n_2 H_2 \cdot \exp\left(\frac{(r_2 - r)}{H_2}\right) + n_3 H_3 \cdot \exp\left(\frac{(r_3 - r)}{H_3}\right) \right] \right\} \quad (2.11)$$

This production function results from the ionization of the neutral profile by means of solar EUV radiation (photoionization frequency for atomic oxygen, measured at Earth and scaled to the heliocentric distance of Venus). Other ion production processes, like electron impact ionization and charge exchange are not taken into account in our model.

Figure 2.11 shows the neutral profile as well as ion production profiles of the day- and nightside of the planet for solar minimum conditions, ($\nu=4.55 \times 10^{-7} \text{ s}^{-1}$, Torr and Torr (1985)). The ion production rate on the dayside is a function of the altitude above the surface and the solar zenith angle, $q=q(r, \chi)$. The solar zenith angle ranges only between $-87^\circ < \chi < +87^\circ$ instead of $-90^\circ < \chi < +90^\circ$ in order to avoid singularities. However, photoionization does not take place on the nightside of Venus as mentioned in subsection 1.1.5. Plasma transport from the dayside due to pressure gradients and electron impact ionization are the sources of the weak nightside ionosphere at Venus. Hence, the ion production rate on the nightside is independent of the solar zenith angle and is set to an altitude depending value, $q=q(r, \chi=87^\circ)$. This yields about 10% of the dayside ion production rate which is an adequate representation for the weak nightside ionosphere.

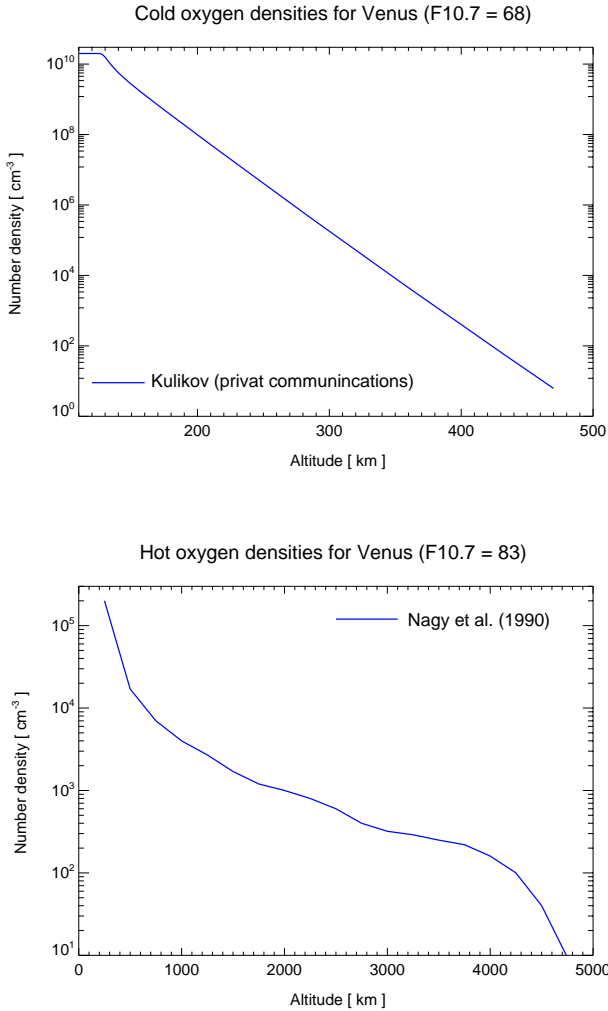


Figure 2.10: Cold O and hot O^* number densities as a function of altitude (km). The upper panel shows the density profile of cold atomic oxygen at Venus for low solar activity ($F_{10.7cm} = 68 \times 10^{-22} \text{ W m}^{-2} \text{ Hz}^{-1}$) based on the model of Kulikov et al. (2006). The lower panel shows the density profile of hot atomic oxygen at Venus for low solar activity ($F_{10.7cm} = 83 \times 10^{-22} \text{ W m}^{-2} \text{ Hz}^{-1}$) based on Pioneer Venus Orbiter (PVO) measurements (Nagy et al. 1990).

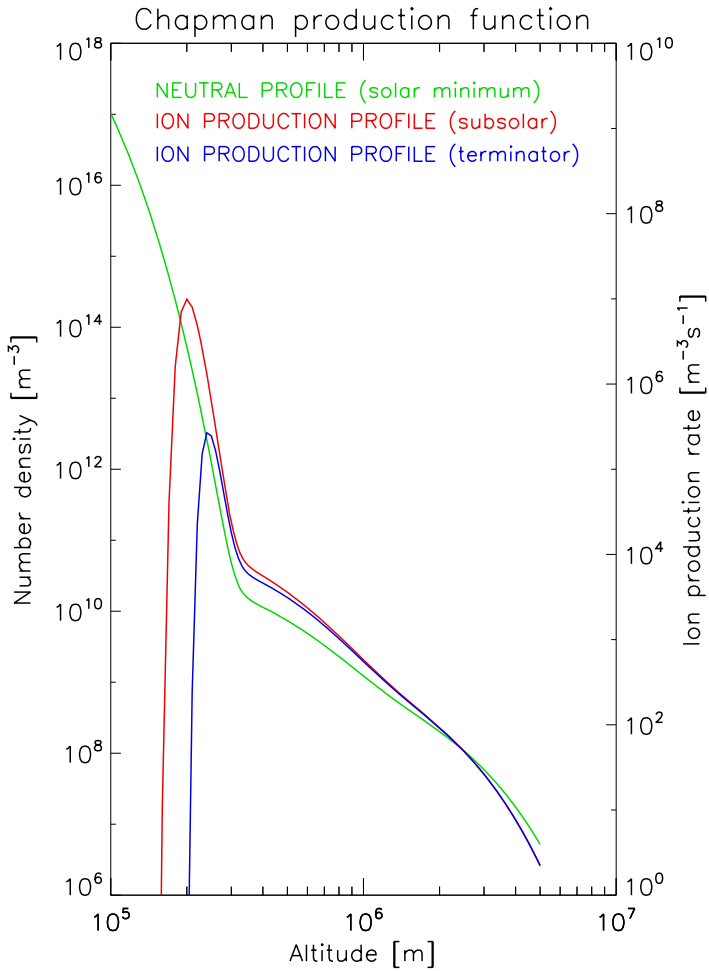


Figure 2.11: The neutral number density (green line) and the ion production rate (red line in subsolar direction and blue line at the terminator) of oxygen as a function of altitude at solar minimum (ionospheric photoionization frequency $\nu=4.55 \times 10^{-7} \text{ s}^{-1}$ (Torr and Torr 1985)).

3 Results

In this chapter I will present the results of the data analysis and the hybrid simulations.

In section 3.1, I will report on measurements made by the ion and electron sensors of ASPERA-4 during their first 14 months of operation and, thereby, determine the locations of the Venus bow shock (BS) and the upper and lower boundary of the mantle region (UMB and LMB) under solar minimum conditions. Additionally, the variation of the terminator shock position as a function of the solar wind dynamic pressure and solar EUV flux are investigated. Finally, this section closes with a discussion of the data analysis.

Section 3.2 reports on the results from the simulation runs carried out for different parameter sets in order to study the global plasma environment of Venus by a 3D hybrid model. The input parameters for Run 1 and Run 2 are based on Venus Express (VEX) observations made on a specific orbit at low solar activity. Run 3 is based on Pioneer Venus Orbiter (PVO) measurements representing typical values for high solar activity. A comparison between the results of the solar minimum runs and solar maximum run is given in the last subsection (3.2.2).

3.1 Location of Plasma Boundaries

Current knowledge of the solar wind interaction with Venus comes almost entirely from the long lasting PVO mission (1978 – 1992) which provided a data set that extended over a complete solar cycle (Russell et al. 2006). The plasma boundaries at Venus were originally identified using data measured by the PVO magnetometer and plasma analyzer. Compared with the magnetometer (MAG) and the plasma analyzer (ASPERA-4) on board of the VEX spacecraft, the PVO instruments had much lower temporal, energy and angular resolutions. VEX gives us the opportunity to fill the gaps left by the PVO observations and to extend our knowledge of the plasma environment of Venus.

In this work, the locations of the plasma boundaries have been exclusively determined from particle measurements obtained by the Electron Spectrometer (ELS) and the Ion Mass Analyzer (IMA), described in chapter 2. Although PVO made observations over the entire solar cycle, no direct measurements of the near Venus plasma environment during solar minimum were possible due to the high PVO orbital altitude (> 2000 km) at that time. The VEX spacecraft has a constant periapsis altitude of about 250 km and thus, we can sample this region during solar minimum. Just prior to PVO arrival, the Russian Venera 9 and 10 orbiters (1975 – 1976) observed the Venus solar wind interaction, including the bow shock and tail during solar minimum (Verigin et al. 1978).

Russell et al. (1988) and Zhang et al. (1990) investigated the Venus bow shock based on nearly 2000 PVO shock crossings and found that the shock location is modulated by the

solar cycle and solar EUV flux, the upstream solar wind parameters and the orientation of the interplanetary magnetic field (IMF) [see also Phillips and McComas (1991) and Russell et al. (2006)]. For modeling the bow shock they have used a simple conic section with its focus at the center of the planet based on PVO data. In this study, a 3-parameter fit based on ASPERA-4 measurements was utilized to achieve a more realistic shape of this boundary. The same technique, i. e. a conic fit with conic focus along the Sun-planet line as a third free parameter, has already been used by Slavin et al. (1980) based on PVO data and was later applied to Mars by Vignes et al. (2000).

Downstream of the planet the plasma measurements indicate a very broad transition zone from solar wind to planetary ions which is referred as to “mantle” region (see Figure 1.12). This boundary layer is characterized by the appearance of magnetosheath plasma as well as ionospheric plasma. The upper and lower boundary of the mantle can be defined by a strong decrease in energetic electrons and a disappearance of solar wind protons, respectively. Since the mantle boundaries can not be represented by a simple conic function (see section 3.1.3) an alternative approach is used in order to model them. Spenser et al. (1980) using PVO data identified a boundary they called the ionosheath boundary, which was defined by an ambient decrease in solar wind flux. Also an ionopause was defined by its association with the vanishing of protons. These authors had, however, no nightside observations. Further, Zhang et al. (1991) defined the ionopause and the upper boundary to constitute the limits of a region of increased magnetic pressure.

3.1.1 VSO coordinate system

Before the ASPERA-4 data are presented and discussed in the following subsections, it is convenient to introduce the Venus-Sun-Orbital (VSO) coordinate system which is used for mapping these data.

In VSO, the positive X_{VSO} -axis points from the center of Venus to the Sun (opposite to the solar wind bulk velocity), the positive Y_{VSO} -axis points opposite to the heliocentric orbital motion of Venus, and the Z_{VSO} -axis completes the right-handed system pointing towards the ecliptic north.

Figure 3.1 illustrates a typical 24-h orbit around Venus in two different displays. The right panel shows the highly elliptical polar orbit in the XZ -plane with the x -axis and y -axis corresponding to the X_{VSO} and Z_{VSO} direction, respectively. In the left panel, the same orbit is shown in the XR_{cyl} -plane, again with the x -axis corresponding to the X_{VSO} direction but the y -axis corresponding this time to R_{cyl} . R_{cyl} is the cylindrical distance defined as $R_{cyl} = \sqrt{Y_{VSO}^2 + Z_{VSO}^2}$ under the assumption of cylindrical symmetry of the plasma distribution along the X_{VSO} -axis.

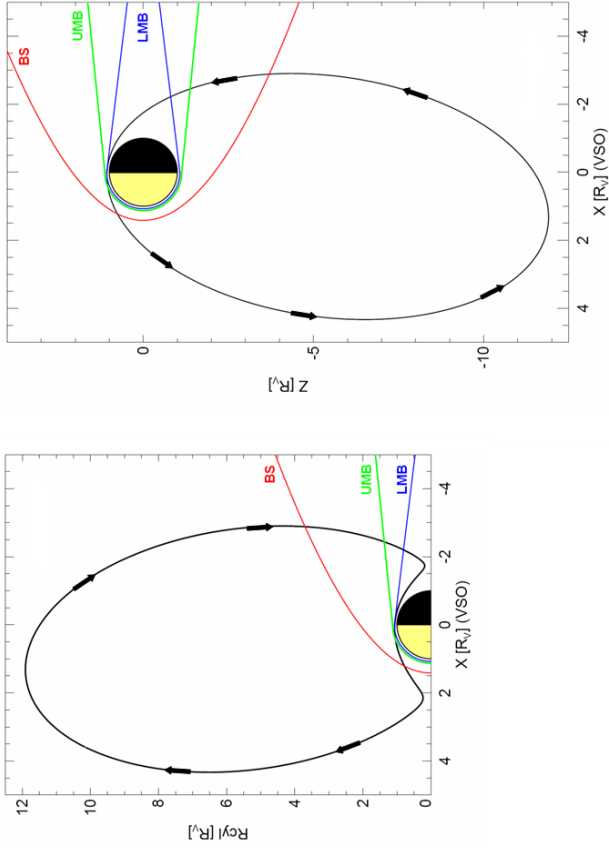


Figure 3.1: A typical 24h-orbit of Venus Express shown in two different displays in order to illustrate the function of the R_{cyl} product. Left: the x-axis corresponds to the X_{VSO} direction and the y-axis to $R_{cyl} = \sqrt{Y_{VSO}^2 + Z_{VSO}^2}$ (assumption of cylindrical symmetry). Right: the x-axis corresponds to the X_{VSO} direction, but the y-axis corresponds to the Z_{VSO} direction in this panel. The average position and shape of the plasma boundaries are also plotted based on the fitting techniques presented in section 3.1.3.

3.1.2 Observations

The data used in this thesis were obtained by the ASPERA-4 experiment onboard of Venus Express which consists of an Electron Spectrometer (ELS), an Ion Mass Analyser (IMA), a Neutral Particle Imager (NPI) and two Neutral Particle Detectors (NPD1 and NPD2). The plasma instrument is presented in section 2.1 and a detailed description is given by Barabash et al. (2007b). In this study we present data from the electron and ion spectrometers, exclusively.

Figure 3.2 displays data obtained on July 15, 2006 showing the main plasma features of the solar wind interaction with Venus about one hour before and after the closest approach of orbit No. 85. The top panel shows an energy spectrogram of measured electrons in the energy range of 0.1 eV - 20 keV obtained by ELS. But electrons below 5 eV are reflected to avoid saturation of the counters. The sensor has 16 anodes covering a total field of view of $4^\circ \times 360^\circ$. Shown are counts obtained during 4s sampling intervals integrated over anodes 5 - 15 of the sensor because anodes 0 - 4 are more noisy. The data shown in the next two panels represent protons and heavy ions, respectively, measured by IMA, integrated over all 16 anodes and separated into 8 spatial sectors covering a total field of view of $90^\circ \times 360^\circ$. Note that signatures above 50 eV energy in the bottom panel in the solar wind and magnetosheath regions are not caused by heavy ions but by saturation of the proton channels. A spatial scan during 192s by electrostatic deflection produces the repeatable pattern visible in the spectrogram. The X -axis shows the distance, position and time of the spacecraft along the orbit.

First, VEX is located inside the solar wind before crossing the bow shock (BS) at 01:15 UT, identified by an increase in counts of energetic electrons ($E > 35\text{eV}$) in the magnetosheath with respect to the solar wind. Passing the BS, the spacecraft enters the magnetosheath, characterized by the shocked, slowed down and heated solar wind. At 01:48 UT, VEX crosses the upper mantle boundary (UMB), identified by a strong decrease in electron counts ($E > 35\text{eV}$), and is located in a so-called mantle region or transition zone, where we observe a mixture of solar wind protons and planetary ions. The lower boundary of the mantle (LMB), crossed at 01:57 UT, we also call the Ion Composition Boundary (ICB), because at this boundary the solar wind protons disappear and the planetary ions become the main population. LMB is identified in ELS by the appearance of ionospheric photoelectrons ($E > 10\text{eV}$). Passing the LMB, the spacecraft is located in the ionosphere between 01:57 UT and 02:01 UT. On the outbound pass, VEX crosses again all the mentioned plasma regions and boundaries, but in reverse order, i. e. at 02:01 the LMB, at 02:08 UT the UMB and at 02:22 the BS, and finally, is back in the solar wind.

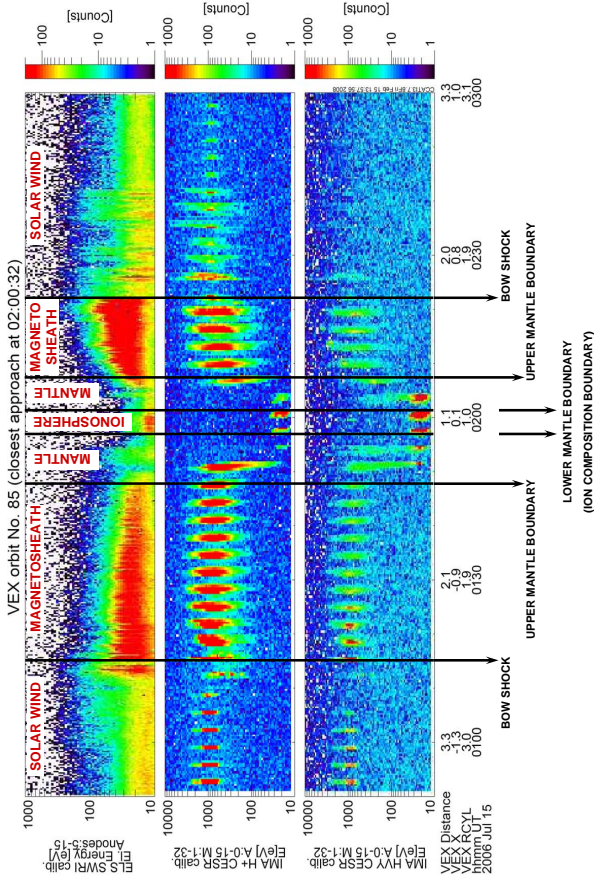


Figure 3.2: ASPERA-4 data recorded on July 15, 2006 - about an hour before and after the pericenter of that orbit ($1R_{\gamma}=6051.8$ km). The top panel shows the total counts of energetic electrons measured by the ELS sensor and the two panels below presents the total counts of the proton and heavy ion channels of the IMA sensor, respectively. The heavy ion channel contains proton counts whenever the proton channel saturates. The black vertical arrows mark the plasma boundaries separating the different interaction regions (solar wind, magnetosheath, mantle and ionosphere).

3.1.3 Plasma boundary fits

From 14 May 2006 to 31 December 2007, 817 Venusian BS crossings, 842 UMB crossings and 798 LMB (ICB) crossings were identified in ELS and IMA data as described above.

For the bow shock we applied the curve fitting technique developed by Slavin and Holzer (1981) which has also been used by Trotignon et al. (2006) for modeling the plasma boundaries at Mars. The observed shock locations have first to be transformed into an aberrated solar ecliptic system (X', Y', Z' ; VSO), where the X' -axis is anti-parallel to the mean solar wind flow direction in the Venus frame of reference assuming a 5 degree aberration. Then, a conic function in polar coordinates, assuming cylindrical symmetry along the X' -axis, is least-square fitted to the observed BS positions. In order to get the best fit to the observations we used an offset of the conic focus along the symmetry axis as introduced by Slavin et al. (1980). Thus, the shock surface is represented by the following equation

$$r = \frac{L}{1 + \epsilon \cdot \cos \theta} \quad (3.1)$$

where the polar coordinates (r, θ) are measured with respect to a focus located at ($x_0, 0, 0$). L is the semi-latus rectum and ϵ is the eccentricity (see Table 3.1).

	$L [R_V]$	ϵ	$x_0 [R_V]$	$r_{tsd} [R_V]$
This study	1.515	1.018	0.664	2.088
Slavin et al. (1984)	1.68	1.03	0.45	2.096
Russell et al. (1988)	2.14	0.609	0.	2.14
Zhang et al. (1990)	2.131	0.66	0.	2.131
Zhang et al. (2008a)	2.14	0.621	0.	2.14

Table 3.1: Venusian BS fit parameters from ASPERA-4/VEX in comparison with Venera 9/10 (Slavin et al. 1984), PVO (Russell et al. 1988, Zhang et al. 1990) and MAG/VEX (Zhang et al. 2008a) results at solar minimum. L , ϵ , x_0 and r_{tsd} are the semi-latus rectum, eccentricity, conic focus and terminator shock distance, respectively.

	Upper mantle boundary	Lower mantle boundary
Circular fit	$r_{UMB} = 1.130 R_V$	$r_{LMB} = 1.076 R_V$
Linear regression	$k_{UMB} = -0.101 R_V$ $d_{UMB} = 1.130 R_V$	$k_{LMB} = 0.122 R_V$ $d_{LMB} = 1.076 R_V$

Table 3.2: UMB and LMB fit parameters from ASPERA-4/VEX at solar minimum.

For modeling the positions of UMB and LMB we used a somewhat different approach because we found that the observations on the dayside and on the nightside cannot be

represented by single conic functions. This was for example also noted in the case of the magnetic pile-up boundary (MPB) at Mars (Trotignon et al. 2006). Thus, we used circular fits for the dayside observations ($X' > 0$) and linear regressions [$y = k \cdot x + d$] for the nightside measurements ($X' < 0$) in order to model the mantle boundaries (see Table 3.2). Note that, currently we do not have data for the mantle region below about 50° solar zenith angle and thus, both fits provide boundaries which are too far away from the planet on the dayside. In order to get more realistic mantle fits it is necessary to include crossings in the subsolar region, expected later during the VEX mission.

Figure 3.3 displays the axisymmetric BS, UMB and LMB (ICB) fits derived using the first 19 months of ELS and IMA observations in an aberrated VSO coordinate system. The red curve is the fit to all BS crossings (circles) obtained by Slavin's method. The green and blue curves are the fits to all UMB (diamonds) and LMB (triangles) crossings, respectively, obtained using the approach discussed above.

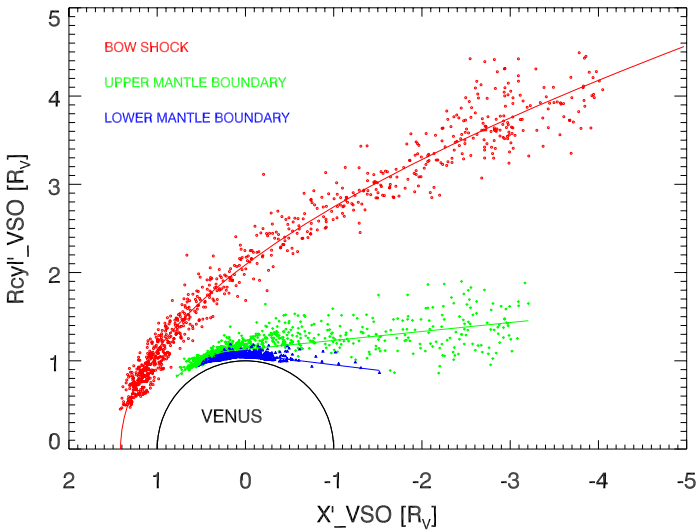


Figure 3.3: This plot displays axisymmetric bow shock (BS), upper (UMB) and lower (LMB) mantle boundary fits derived using the first 19 months of ASPERA-4 observations in an aberrated VSO coordinate system. The BS crossings (red circles) were fitted to a conic function. The UMB (green diamonds) and LMB (blue triangles) crossings were fitted by a circle on the dayside and by linear regression on the nightside.

3.1.3.1 Solar wind dynamic pressure vs. terminator shock distance

Additionally, the variation of the BS position at the terminator as a function of the solar wind dynamic pressure has been investigated as shown in Figure 3.4. All BS crossings (blue plus signs) were extrapolated to the terminator plane using a conic section curve with a fixed focus ($x_0 = 0.664$) and eccentricity ($\epsilon = 1.018$) and a variable L value:

$$L = \sqrt{(X' - x_0)^2 + Y'^2 + Z'^2 + \epsilon \cdot (X' - x_0)}. \quad (3.2)$$

Then the terminator shock distance is given by

$$r_{tsd} = \sqrt{L \cdot (L + 2 \cdot \epsilon \cdot x_0) + x_0^2 \cdot (\epsilon^2 - 1)}. \quad (3.3)$$

The red points in Figure 3.4 represent median values over pressure bins and demonstrate clearly the independence of the BS position from the ram pressure during solar minimum conditions. This finding is in agreement with results obtained by Russell et al. (1988) and by Zhang et al. (2004) based on PVO observations.

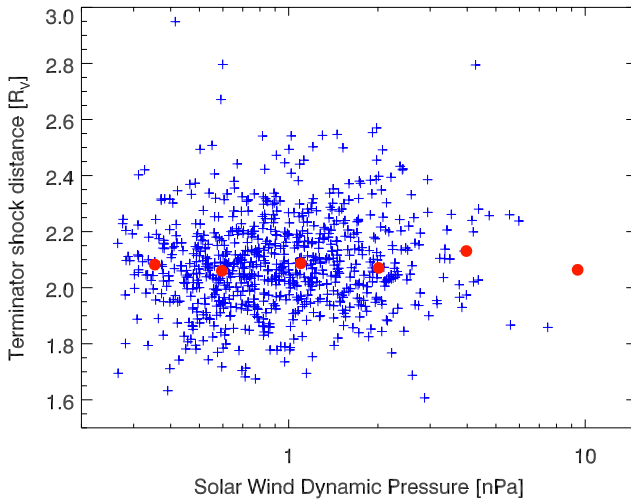


Figure 3.4: The dependence of the bow shock position at the terminator on the dynamic pressure of the solar wind derived from ASPERA-4 measurements. All bow shock crossings (blue plus signs) were extrapolated to the terminator plane using a conic section curve with a fixed eccentricity ($\epsilon = 1.018$) and a fixed focus ($x_0 = 0.664$) and with a variable semi-latus rectum. No normalization has been applied to the data. The red points represent median values over pressure bins.

3.1.3.2 Solar EUV flux vs. terminator shock distance

From PVO observations we learned that the solar wind interaction with Venus is very dependent on the phase of the solar cycle (Russell et al. 2006). During solar minimum the BS is found to be closer to the planet than during solar maximum due to lower ionization and ion pickup rates caused by EUV flux changes over the 11-year solar cycle.

Figure 3.5 shows the terminator BS position, obtained by equation 3.3, as a function of the solar EUV flux (F50 index: 0.1 - 50nm integrated photons $\text{cm}^{-2} \text{s}^{-1}$ and shifted to Venus) derived from SOHO SEM observations since VEX does not carry an instrument for this purpose. The Solar Extreme-Ultra-Violet Monitor (SEM) is a highly stable photodiode spectrometer that continuously measures the full solar disk absolute photon flux at the He II 30.4 nm line as well as the absolute integral flux between 17 and 70 nm.

Although this index is an excellent indicator of overall solar activity levels, we do not observe yet an effect on the terminator BS location in our data set, because the EUV flux variation is small over the period of observation as expected for solar minimum.

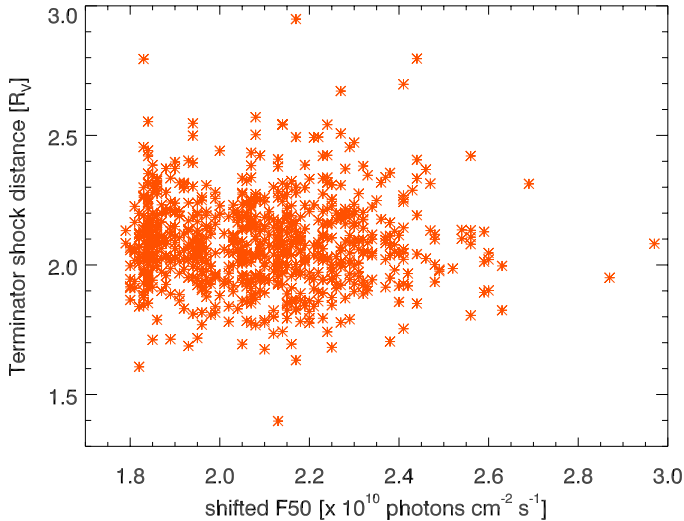


Figure 3.5: This plot shows the terminator bow shock position as a function of solar EUV flux (F50 index: 0.1 - 50nm integrated photons $\text{cm}^{-2} \text{s}^{-1}$) derived from SOHO SEM observations and shifted to Venus. All bow shock crossings (orange asterisk signs) were extrapolated to the terminator plane by means of the conic function.

3.1.4 Influence of data accuracy on the boundary determinations

For the determinations of the plasma boundaries the absolute calibrations of the IMA and ELS sensors are not relevant since we determine the boundary crossings only by relative changes of the observed flux intensity. However, the main influences are caused by the time resolutions of the observations. The ion sensor (see subsection 2.1.2) has a time resolution of only 192 seconds for a full 3D scan and thus, it can only be used as a rough indicator for the occurrence of the planetary ions. We use the ELS sensor (see subsection 2.1.1) and magnetic field observations, which both have a time resolution of 4 seconds, to determine the crossing times. Since the spacecraft velocity relative to Venus is less than 10 km/s, this corresponds to spatial precision of 40 km for the determinations of the plasma boundaries. On the other hand, if the boundaries are moving relative to Venus with velocities larger than 10 km/s, the error is respectively higher. Another influence on the accuracy of the boundary determinations is the aberration of the solar wind flow by the orbital speed of Venus. For this aberration we assume a constant solar wind speed of 400 km/s corresponding to an aberration angle of 5° .

3.1.5 Discussion and Conclusions

In this section, the positions of the Venusian BS, UMB and LMB at solar minimum have been determined based on ASPERA-4 observations made on board the VEX spacecraft. The observed VEX crossings of the plasma boundaries were transformed into an aberrated solar ecliptic system, assuming a 5 degree aberration angle. The BS is represented by a conic section, expressed in polar coordinates under the assumption of cylindrical symmetry along the X' -axis (i.e. opposite to the solar wind flow direction) and with an offset of the focus which is allowed to move along the symmetry axis. The radial coverage in the subsolar region is not homogeneously sampled by VEX and thus, the BS fit was corrected by omitting crossings below 30° solar zenith angle. The UMB and LMB (or ICB) are each represented by a circle on the dayside and by a line fit on the nightside in order to obtain satisfactory fits to the data.

Figure 3.6 shows the VEX BS fit in comparison with other shock models based on different data sets at solar minimum. The BS fit obtained in this study is in good agreement with the BS model of Slavin et al. (1984) based on Mariner 5,10 and Venera 4,6,9,10 observations. They also used a 3-parameter conic section for modeling the upstream and downstream shock location which results in a hyperbola since $\epsilon > 1$. Russell et al. (1988) investigated the Venusian BS by means of magnetic field measurements on board PVO. They fitted the dayside shock crossings by using a 2-parameter conic function where its focus is fixed at the center of the planet resulting in an ellipse since $\epsilon < 1$. The dayside BS model from Zhang et al. (2008a), based on Magnetometer data made on board VEX, is also obtained by using a 2-parameter conic section with a fixed focus at the center of Venus. However, only shock crossings between 0° and 117° solar zenith angle were fitted, whereas the distant BS (solar zenith angle $> 117^\circ$) is represented by an asymptotic shock cone determined by an average magnetosonic Mach number of 5.5 at solar minimum. Theoretically, the distant BS should be a Mach cone but in-situ measurements made by ASPERA-4/VEX provide the counterevidence that this is not the case for the Venusian BS. The same result was found by Trotignon et al. (2006) investigating the location and

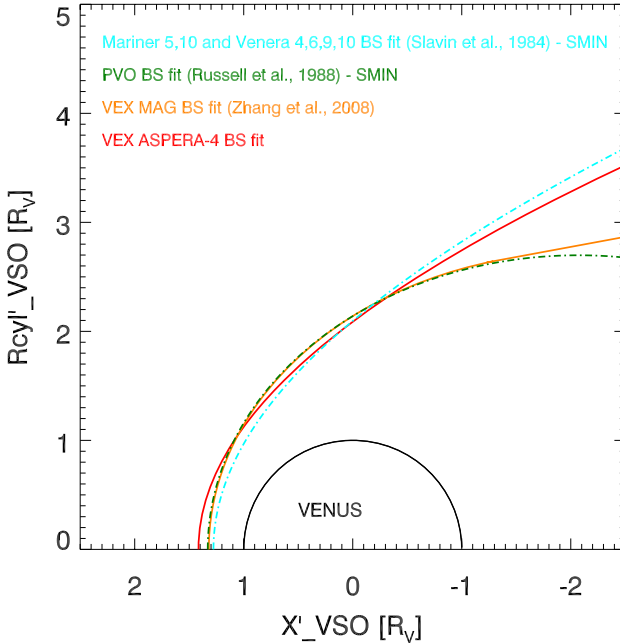


Figure 3.6: Venus Express bow shock (BS) fit in comparison with other shock models based on different data sets at solar minimum. Slavin et al. (1984) also used a 3-parameter conic section for modeling the upstream and downstream BS ($\epsilon > 1$ hyperbola). Russell et al. (1988) and Zhang et al. (2008a) fitted the dayside BS crossings with a 2-parameter conic function where its focus is fixed at the center of the planet ($\epsilon < 1$ ellipse).

shape of the Martian BS based on Phobos 2 and Mars Global Surveyor (MGS) data sets. These observations demonstrated that the far downstream BS at Mars does also not meet a Mach cone. In summary, the shape of the VEX BS fit rather agrees with the BS model of Slavin et al. (1984) than with the elliptical BS models of Russell et al. (1988) and Zhang et al. (2008a).

Dubinin et al. (2008) determined the magnetospheric boundary (MB) and photoelectron boundary (PEB) at Mars based on ASPERA-3 and MARSIS observations on board Mars Express. MB is identified by a strong decrease (inbound pass) or increase (outbound pass) in energetic electron density. PEB marks the outer boundary of the ionosphere which is identified by the appearance of energy peaks in the range between 20 and 30 eV in the electron spectrograms. Consequently, the physics of UMB and LMB can be compared with MB and PEB, respectively.

However, the upper and lower boundary positions of the magnetic barrier determined by Zhang et al. (2008b) based on the magnetometer observations on board VEX are only partly in agreement with our determination of UMB and LMB locations. At the terminator the average thickness of the mantle region is around 500 km and hence, 300 km less thick than the magnetic barrier. The thickness of the magnetic barrier in the subsolar region is around 200 km (Zhang et al. 2008b) but currently we cannot estimate this thickness for the mantle region due to the lack of mantle crossings below around 50° solar zenith angle.

In conclusion, the ASPERA-4 measurements exhibit a relatively stable BS position, whereas the upper and lower boundary of the mantle region are highly variable on the nightside. In comparison to the large variations observed for the UMB, the variations of the BS position is smaller (about 15 % of the terminator distance). The variations visible in the BS locations can be attributed to the variations in the magnetic field strength, since the BS position should depend on the upstream Mach number (Zhang et al. 2008a). Previous studies based on PVO data (Russell et al. 1988) showed that the main factors influencing the BS position are the solar cycle, the upstream magnetosonic Mach number and the IMF clock angle ($\arctan(B_y/B_z)$). But to detect the relatively small influences on magnetosonic Mach number and IMF clock angle, Russell et al. (1988) use only small subset of the large PVO data set (3300 orbits) with crossings within $0.5 R_V$ close to the terminator. If we would apply the same selection to our data set, our statistics would be insufficient in order to analyze the dependency of the terminator BS position on the magnetosonic Mach number and IMF clock angle. For that reason we leave these issues for a later investigation. On the other hand, if we cannot decrease the number of data points we introduce a larger error in the dependency analysis caused by the projection of all BS crossings onto the terminator plane as well as by the assumption of a constant aberration angle.

Furthermore, the effect of the solar wind dynamic pressure on the terminator BS location was examined. We find that the shock position is insensitive to changes in the dynamic pressure of the solar wind, at least during solar minimum, as was earlier reported by Russell et al. (1988) and by Zhang et al. (2004). We observed that the spread in the terminator distance was much lower in our dataset than in that investigated by Zhang et al. (2004) represented in Figure 3, despite the fact that these authors tried to correct for EUV and IMF influence. One reason may be that solar conditions in our 19 month dataset varied less than was the case in the course of the long duration PVO observations. Also, Zhang et al. (2004) used in their fits a focus fixed at the center of the planet, which fits the bow shock shape less well.

Additionally, the dependence of the terminator BS position on the solar EUV flux was investigated because the solar wind interaction with Venus is very dependent on the phase of the solar cycle. At solar minimum the BS is found to be closer to the planet than at solar maximum by PVO due to lower ionization and ion pick up rates (Russell et al. 2006). However, in the ASPERA-4 data set one does not observe yet an effect on the terminator BS position because the EUV flux variation is small over the period of observation as expected for solar minimum.

3.2 Hybrid Simulations

The global Venus-solar wind interaction can be studied by different numerical investigations such as gasdynamic, magnetohydrodynamic (MHD) and kinetic models.

In general, a gas dynamic model (Spreiter and Stahara 1992) is able to reproduce some of the global characteristics of the interaction (bow shock, magnetosheath region) but it neglects the individual particle behavior as well as the effects of the magnetic field on the plasma dynamics. Thus, this fluid approximation does not include the magnetic barrier in a self-consistent manner and additionally, does not consider the exospheric ion pickup process due to the convective electric field (Zhang et al. 1993).

More sophisticated treatments can be done using MHD models because here the magnetic field is taken into account in a self-consistent manner (Wu 1992, Tanaka 1993, Murawski and Steinolfson 1996a,b, Tanaka and Murawski 1997, Kallio et al. 1998, Bauske et al. 1998). The position and shape of the bow shock, bow shock asymmetries associated with the oblique IMF orientation, the formation of the magnetic barrier, the magnetosheath and the magnetotail could be reproduced in these studies and are in a good agreement with observational data (e. g. from PVO). While MHD simulations provide an adequate picture of the large-scale solar wind interaction with Venus, including the mass loading of the solar wind with heavy oxygen ions, several important kinetic effects are not considered in these studies due to the single fluid description. Thus, asymmetries in the form of the bow shock, the magnetic barrier intensity and the planetary pickup distribution as well as the formation of the ion composition boundary (separation between solar wind plasma and planetary plasma) and multiple-shocklets (explained in Section 3.2.1.1) cannot be reproduced by MHD models.

The gyroradii of the solar wind protons are in the range of several hundred kilometers, and therefore comparable with the characteristic scales of the subsolar interaction region. The gyroradii of the heavy pickup ions are in the range of several thousand kilometers, and therefore comparable with the radius of the planet. Thus, a kinetic treatment seems to be mandatory and is used here. Since the gyroradii of the electrons are very small, a fluid description is used for the solar wind and ionospheric electrons. A full particle code would be the most suitable numerical investigation but with the current computational resources, a fully kinetic approach is not feasible. Hence, a hybrid model is a very useful tool for studying the kinetic effects because it treats ions as gyrating particles (Moore et al. 1991).

Several hybrid simulations were carried out over the past years and in general demonstrated a good qualitative agreement between the simulation results and observational data.

The results of a three-dimensional hybrid simulation from Brecht and Ferrante (1991), including the ionosphere by assuming the planet as a conducting sphere, showed that the bow shock and magnetic barrier are asymmetrical at Venus.

In the hybrid model of Shimazu (2001) the Venusian planet was treated as an ionized gaseous body with uniform and constant supply of plasma. The simulation results provided an asymmetric bow shock with a multiple-shock structure, a magnetic barrier in front of the planet with asymmetries along the solar wind electric field, a magnetotail, tail rays and a plasma sheet. He found that the calculated asymmetry in the magnetic barrier intensity was consistent with observations, but the direction of the calculated asymmetry

in the shock size did not concur with the observed asymmetry. Shimazu (2001) assumed that this discrepancy could be a result of not taking into account the effect of photoionization and charge exchange outside of the ionosphere in the hybrid model. However, he pointed out that further studies are needed in order to investigate this incongruity. Additionally, they demonstrated that ions escape to the magnetotail through the tail rays and that the tail rays were connected with the plasma sheet.

Other hybrid approaches deal with the investigation of the ion escape processes with a particular emphasis placed on the processes occurring at the ionopause associated with the Kelvin-Helmholtz instability (Terada et al. 2002, 2004). Their 2D simulation model results yielded an asymmetrical convection pattern of the ionosphere due to the asymmetrical momentum transport across the ionopause and showed the dynamic nature of the interaction. Moreover they concluded that most probably, the dynamic ion removal process associated with the Kelvin-Helmholtz instability plays a significantly role in the ion escape from the planet. However, since they considered only two dimensions in their hybrid model, the Kelvin-Helmholtz instability might be of less importance for the ion escape processes at Venus, if relaxation occurs in the third dimension. This has not been taken into account in their investigation.

Kallio et al. (2006) studied the solar wind interaction with Venus using a global three-dimensional self-consistent quasi-neutral hybrid model (QNH) and focused on the asymmetries in the direction of the convection electric field caused by kinetic effects, the role of the interplanetary magnetic field (IMF) x-component and the properties of the escaping planetary O^+ ions. On the one hand they found a notable north-south asymmetry of the magnetic field and plasma due to ion finite gyroradius effects and escaping O^+ ions. On the other hand they showed that an asymmetry exists between the quasi-perpendicular bow shock hemisphere and the quasi-parallel bow shock hemisphere, which results from the IMF x-component. In general, the QNH model is able to reproduce the main observed plasma and magnetic field regions such as the bow shock, the magnetosheath, the magnetic barrier and the magnetotail.

The model of Kallio et al. (2006) is similar to the hybrid approach presented in this study. The main differences between the two models are associated with the spatial resolution of the simulation grid, the temperature of the electrons and the IMF angle. Our model performs the simulation on a curvilinear grid (see section 2.2.3) obtaining a spatial resolution of about 100-150 km/cell in the vicinity of the obstacle and about 250-300 km/cell beyond the distorted grid. The model of Kallio et al. (2006) use an equidistant grid which provides only a spatial resolution of 605 km everywhere in the simulation box which, for instance, inhibits the evolution of a self-consistent ionosphere. In our hybrid code, we take into account the different electron temperatures in the solar wind and ionosphere by using two different electron pressure terms which play an important role in the ICB formation (discussed in the following section), while Kallio et al. (2006) assume cold electrons. Finally, they use the Parker spiral angle as cone angle while in this study the average IMF angle is determined based on the Magnetometer data for the respective orbit.

Parameter	Values	Comments
Solar wind density, n_{sw}	5.0 cm ⁻³	—
Solar wind velocity, v_{sw}	360.0 km s ⁻¹	in x-direction
Magnetic field magnitude, B_{sw}	5.0 nT	in y-direction
IMF orientation, φ_{sw}	-22.5 deg	in VSO
Polar angle, ϑ_{sw}	90.0 deg	in z-direction lying in the equatorial plane
Electron beta, $\beta_{e,sw}$	0.81	$T_{e,sw} = 10.0$ eV
Proton beta, $\beta_{i,sw}$	1.61	$T_{i,sw} = 20.0$ eV
Ionospheric electron beta, $\beta_{e,hi}$	0.02	$T_{e,hi} = 0.3$ eV (Miller et al. 1980)
Alfén velocity, v_A	48.77 km s ⁻¹	—
Alfénic Mach Number, M_A	7.38	dimensionless
Sound velocity, c_S	75.81 km s ⁻¹	—
Sonic Mach Number, M_S	4.75	dimensionless
Ionospheric photoionization		
frequency, ν_{smin}	4.55×10^{-7} s ⁻¹	Torr and Torr (1985)
Total ion production, Q_{O^+}	1.037×10^{26} s ⁻¹	Chapman production function
Lower boundary of atmosphere	1 R_V + 150.0 km	$R_V = 6051.8$ km
Upper boundary of atmosphere	2 R_V	—
Box size, X, Y, Z	$-3 R_V \leq X, Y, Z \leq +3 R_V$	—
Number of grid cells, N_X, N_Y, N_Z	(101, 101, 101)	—
Time step, Δt	2.09 s	—
Total running time, t	1043.97 s	—

Table 3.3: List of simulation parameters used for Run 1 (VEX orbit 85).

3.2.1 Simulation results for low and high solar activity

3.2.1.1 Run 1: VEX orbit 85 – Polar angle = 90

Table 3.3 shows a list of input parameters measured on orbit 85 (15 July 2006) by the plasma and magnetic field instruments onboard VEX, parameters taken from literature and parameters calculated based on all these values as well as simulation parameters. The plasma moments (n_{sw} , v_{sw} , $T_{e,sw}$ and $T_{i,sw}$) derived from ASPERA-4 are estimated either by integrating over a given range in the phase space (integration method), or by assuming a Boltzmann distribution for the phase space density (fitting method) (Fränz et al. 2007). The magnetic field parameters (B_{sw} , φ_{sw} and ϑ_{sw}) obtained by MAG are mean values from the inbound and outbound pass of the concerned orbit. The ionospheric electron temper-

3 Results

ature ($T_{e,hi}$) was taken from Miller et al. (1980) (PVO observations) because a deflection voltage of about 5 eV prevents the measurement of low energy electrons (spacecraft photoelectrons) by the ELS sensor in order to avoid saturation of the counters (see subsection 2.1.1). The other parameter taken from literature is the ionospheric photoionization frequency for atomic oxygen during solar minimum activity (Torr and Torr 1985).

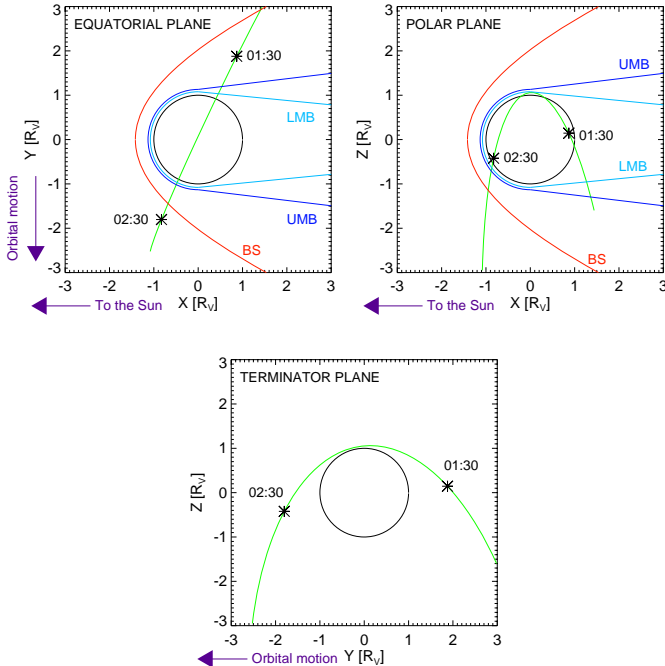


Figure 3.7: Projections of the trajectory of the Venus Express orbit No.85 on the equatorial, polar and terminator plane of our 3D hybrid simulation. The undisturbed plasma flow is directed along the (+x)-axis, the convection electric field ($\vec{E} = -\vec{v} \times \vec{B}$) is orientated antiparallel to the z-axis and the background magnetic field completes the right-handed system pointing in the positive y-direction (tilted 157.5° , corresponding to -22.5° in VSO, in the equatorial plane).

Figure 3.7 shows the trajectory of the VEX spacecraft on July 15, 2006 (orbit 85) in the SIM coordinate system projected on the equatorial, polar and terminator plane. The undisturbed solar wind parameters derived from ASPERA-4 and MAG were measured on this orbit which lies in the terminator plane (view of the trajectory from the nightside of Venus). Additionally, the plasma boundaries determined in subsection 3.1.3 based on ASPERA-4 measurements are displayed in all three panels. In the equatorial cut VEX

crosses the BS at 01:15 UT, flies over the North pole of Venus and crosses the BS again at 02:22 UT on the outbound pass. In the polar cut the spacecraft approaches the BS on the inbound pass from the nightside passing through the wake region, reaches closest approach of around 309 km above the planet's North pole at 02:00:32 UT and leaves the plasma environment of Venus on the dayside.

Figures 3.8 and 3.9 represent global 3D views of the simulation results for the magnetic field configuration and heavy ion density, respectively. The cutting planes through the simulation box are taken at $X=0$ (terminator plane), $Y=0$ (polar plane) and $Z=0$ (equatorial plane). The simulation geometry is described in subsection 2.2.5.

In Figure 3.8, showing the magnetic field configuration at Venus, the solar wind enters the simulation box from the left forming a magnetosonic shock wave upstream of the planet. On the dayside the IMF piles up in front of the obstacle, drapes around Venus and creates an induced magnetotail consisting of two lobes on the nightside. In the equatorial plane one can see the dusk magnetic field lobe where the IMF points toward the planet (visible in Figure 3.12).

A global picture of the planetary plasma is shown in Figure 3.9. In the northern hemisphere (E^-) one can see a very sharp ion composition boundary (ICB) whereas in the southern hemisphere (E^+) this boundary is less pronounced because the heavy ions are accelerated along the convective electric field and dragged away from the planet (pickup process). The formation of the ICB is discussed in more detail below.

Figures 3.10, 3.11 and 3.12 represent 2-dimensional cuts of the 3D simulation results ($t=940s$) at the cutting planes $X=0$ (terminator plane), $Y=0$ (polar plane) and $Z=0$ (equatorial plane), respectively.

In Figure 3.10 are shown from left to right the solar wind density n_{sw} [cm^{-3}], heavy

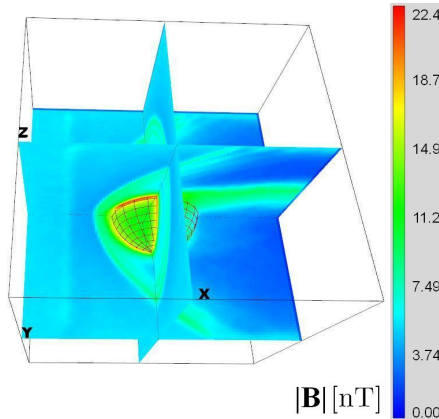


Figure 3.8: Global 3D view of simulation results showing the magnetic field strength [nT]. The cutting planes through the simulation box are taken at $X=0$ (terminator plane), $Y=0$ (polar plane) and $Z=0$ (equatorial plane).

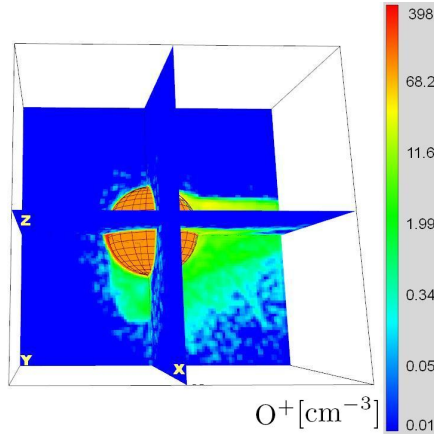


Figure 3.9: Global 3D view of simulation results showing the heavy ion density (O^+) [cm^{-3}]. The cutting planes through the simulation box are taken at $X=0$ (terminator plane), $Y=0$ (polar plane) and $Z=0$ (equatorial plane).

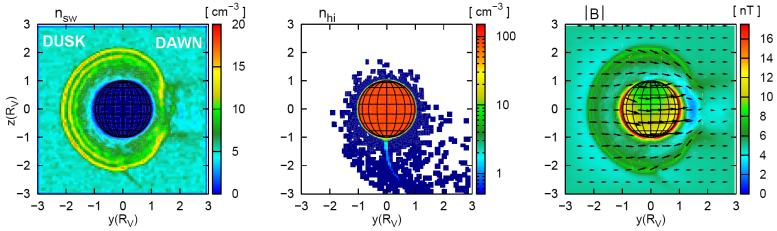


Figure 3.10: Simulation results of Run 1 in the terminator plane, i. e. one looks from tail-side towards Venus. The solar wind is orientated out of the plane ($+x$ -axis), the convective electric field is antiparallel to the ($+z$)-axis and points away from the planet and thus, the background magnetic field completes the right-handed system ($+y$ -axis). The figures display from left to right the solar wind density (n_{sw}), the heavy ion density (n_{hi}) and the background magnetic field. An asymmetric bow shock, exhibiting a shocklet structure, is formed in front of the obstacle due to the supersonic solar wind (left plot). The interplanetary magnetic field is draping around Venus generating an induced magnetotail on the nightside of the planet (right plot). See text for details.

ion density n_{hi} [cm^{-3}] and the magnetic field $|B|$ [nT] along the terminator plane. The increased solar wind density indicates a bow shock formation in front of the obstacle due to the supersonic solar wind flow (left plot). The fast magnetosonic shock

wave exhibits several asymmetries. On the one hand, the shock geometry offers a small asymmetry with respect to the north-south direction due to the pickup of oxygen ions in the direction of the convective electric field. As a consequence, the mass-loading effect decelerates the plasma flow in the E^+ hemisphere. On the other hand, the bow shock is also asymmetric with respect to the dawn-dusk direction which results from the chosen interplanetary magnetic field (IMF) angle of -22.5° in VSO (for symmetric case: 90°). Furthermore, the bow shock is not circular at the terminator plane because the propagation velocity of the fast magnetosonic wave is greatest in the direction of 90° to the magnetic field (positive z-axis). Thus, the plasma is less compressed and requires a greater volume in order to flow around the obstacle in this direction (Russell et al. 1988). Besides these asymmetries there are two more features visible in the solar wind density. Behind the bow shock, so-called shocklets (Omidi and Winske 1990) or multiple shocks (Shimazu 2001) occur which are kinetic shock substructures due to the finite gyroradius of the solar wind protons where the proton density locally increases (at the reversal point) and the proton velocity decreases at the same time. Lastly, the shock is very weak (or almost not present) on the dawn side of the obstacle due to a quasi-parallel shock scenario. The shock normal is parallel to the IMF orientation (see $|B|$ in Figure 3.12) so that solar wind protons can be reflected there and are gyrating back into the plasma flow.

In the heavy ion density (Figure 3.10) one can see clearly an exospheric region (hot oxygen corona) which is in direct interaction with the on-coming plasma flow, as well as a weak ionosphere (cold oxygens) because of the low solar activity condition.

The global configuration of the magnetic field is illustrated in the last plot in Figure 3.10. As already mentioned in subsection 1.2.4, Venus does not possess an intrinsic magnetic field and thus, the IMF lines are draping around Venus leading to an induced magnetotail on the nightside of the planet.

Figure 3.11 displays the simulation results of the solar wind density n_{sw} [cm^{-3}] and velocity $|v_{sw}|$ [km s^{-1}], heavy ion density n_{hi} [cm^{-3}] and velocity $|v_{hi}|$ [km s^{-1}], the magnetic field $|B|$ [nT] and the solar wind electric field $|E|$ [V km^{-1}] in the polar plane.

In the polar plane the simulation produces an almost symmetric flow of the shocked and slowed down solar wind around the obstacle. Additionally, a plasma wake is formed behind the planet where the proton density vanishes (proton cavity).

The solar wind bulk velocity is increased downstream above the north pole (E^- hemisphere) whereas downstream below the south pole (E^+ hemisphere) it is significantly decelerated. The same features appeared in the 3D hybrid simulation of the plasma environment of Mars and Bößwetter et al. (2004) found the following explanation for that picture. The magnetic tension and the pressure force, which are caused by the curvature and magnetic field gradients, are operating on the solar wind protons and heavy ions. These forces are strongest in the vicinity of the poles where the draped magnetic field lines can unwind. As a result, it leads to an acceleration of the solar wind plasma in the E^- hemisphere while the same acceleration force is compensated by the decelerated solar plasma flow stemming from the mass loading of heavy ions in the E^+ hemisphere.

By comparing the solar wind and heavy ion densities one observes a clear separation of the different plasmas in the E^- hemisphere which is divided by the so-called ion composition boundary (ICB), as also already mentioned in subsection 3.1.2 in the course of the determinations of the plasma boundaries based on spacecraft measurements. The formation of the ICB has already been extensively studied by Simon et al. (2007) in the

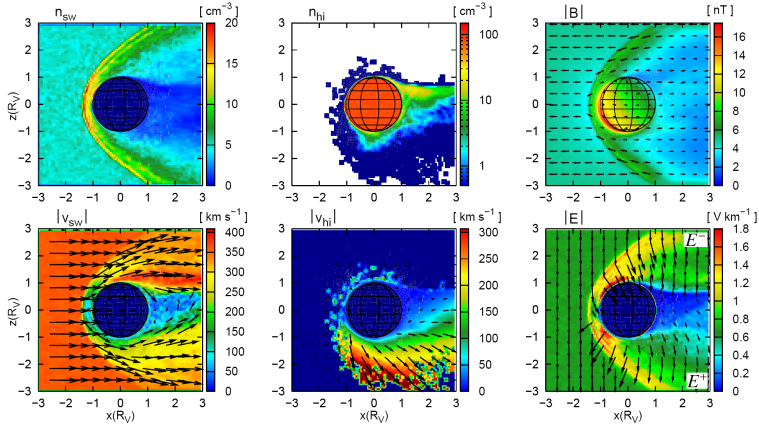


Figure 3.11: Cut through the simulation box of Run 1 along the polar plane, i. e. one looks from the western (dusk) side (in the sense of orbital motion) towards Venus. The plasma flow comes in from the left (+x-axis), the solar wind electric field points away from the planet (-z-axis) and the interplanetary magnetic field completes the right-handed system pointing into the plane (+y-axis). The figures illustrate from left to right in the first row the solar wind density (n_{sw}), the heavy ion density (n_{hi}) and the background magnetic field; and in the second row the solar wind bulk velocity ($|v_{sw}|$), heavy ion bulk velocity ($|v_{hi}|$) and the convective electric field. In the density plots a clear separation between the solar wind and ionospheric plasma takes place forming the so-called ion composition boundary (ICB) in the northern hemisphere. In the south hemisphere there is no clear ICB due to the mass loading effect, i. e. the planetary ions are accelerated in the direction of the convective electric field and are picked-up by the solar wind flow. The solar wind electric field $\vec{E} = -\vec{v} \times \vec{B}$ vanishes where the heavy ion plasma dominates. See text for details.

framework of global 3D hybrid simulations of the plasma environments of Mars and Titan. They concluded that the underlying physical mechanism which is giving rise to the ICB is associated with the Lorentz forces that act on protons and heavy ions and can be explained in terms of kinetic models. The decisive role for the development of the ICB plays the combination of the convective electric field and the electron pressure forces. That means, in the E^- hemisphere where both forces are antiparallel it leads to the formation of a sharply pronounced boundary layer inhibiting the mixing of the plasmas. In contrast, in the E^+ hemisphere no ICB emerges due to the parallelism of both forces. As a result heavy ions are dragged away from the planet in the direction of the convective electric field and thus, causing a significant extension of the ionospheric tail. In other words, on the one hand, at the ICB the solar wind ions are reflected because the electron pressure gradient points away from the planet due to the high electron density in the iono-

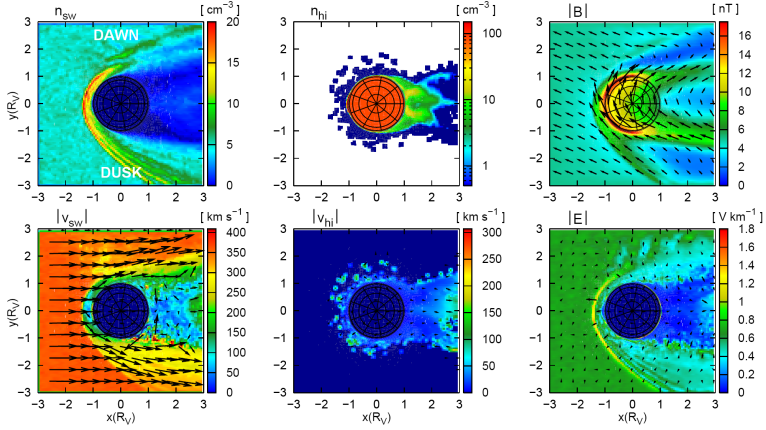


Figure 3.12: Simulation results in the equatorial plane, i. e. one looks from ecliptic North towards Venus. The undisturbed solar wind flow is parallel to the positive x -axis, the convective electric field points into the plane ($-z$ -axis) and the background magnetic field completes the right-handed system ($+y$ -axis) and is tilted 157.5° in the equatorial plane. The figures show from left to right in the first row the solar wind density (n_{sw}), the heavy ion density (n_{hi}) and the background magnetic field; and in the second row the solar wind bulk velocity ($|v_{sw}|$), heavy ion bulk velocity ($|v_{hi}|$) and the convective electric field. Behind the bow shock, the solar wind density is increased and the solar wind bulk velocity is decreased, characterizing the magnetosheath region. Atmospheric material is lost through the plasma wake, thereby forming tail rays and filaments on the nightside ionosphere. The interplanetary magnetic field piles up on the dayside of the planet, producing a so-called magnetic barrier region, wherein the magnetic pressure exceeds the thermal pressure of the solar wind (plasma beta below unity). See text for details.

sphere and on the other hand, the heavy ion particles are accelerated towards the ICB in the direction of the convective electric field which points to the planet.

Inside the ionospheric tail the particles gyrate with a small gyroradius due to the vanishing solar wind electric field while the picked up oxygen ions move away from Venus on large cyclodial paths as can be seen in the bulk velocity of the heavy ions. Owing to the acceleration of the planetary particles in the direction of the convective electric field, heavy ions are picked up by the solar wind, mass is added to the plasma flow (mass loading effect) and atmospheric material leaves from the planet.

The intensity of the magnetic field shows an asymmetric behavior which also has been confirmed by observations (Zhang et al. 1991) as well as by previous simulations (Shimazu 2001, Bößwetter et al. 2004). The piling up of the magnetic field in the E^+ hemisphere is a consequence of the mass loading by planetary ions which leads to a deceleration of the shocked solar wind.

The convective electric field, carried by the solar wind, vanishes in the plasma wake because it is inhomogeneously filled with ionospheric plasma as can be seen in Figure 3.11 and 3.12. In the E^- hemisphere the electric field is orientated perpendicular to the ICB and thus, pointing towards the planet while in the E^+ hemisphere it is pointing away from Venus, as already mentioned above in the course of explaining the ICB formation.

Figure 3.12 illustrates the simulation results of the solar wind density n_{sw} [cm^{-3}] and velocity $|v_{sw}|$ [km s^{-1}], heavy ion density n_{hi} [cm^{-3}] and velocity $|v_{hi}|$ [km s^{-1}], the magnetic field $|B|$ [nT] and the solar wind electric field $|E|$ [V km^{-1}] in the equatorial plane. The bow shock is asymmetrical also in the equatorial plane, as mentioned above when describing the simulation results of the terminator plane. Again, one finds the multiple shocklet structure as well as the quasi-parallel shock scenario, on the western (dusk) side (in the sense of orbital motion). In addition, the solar wind bulk velocity is significantly decreased in the downstream region which is a characteristic of the magnetosheath. The geometry of the magnetic field on the nightside is related to the draping of the interplanetary magnetic field over the obstacle on the dayside (Luhmann and Cravens 1991). As a result, an induced magnetotail is formed behind the planet, consisting of 2 lobes of opposite polarity separated by a plasma sheet. Additionally, the IMF piles up on the dayside of the planet, producing a so-called magnetic barrier region, wherein the magnetic pressure exceeds the thermal pressure of the solar wind. This is also consistent with spacecraft measurements (Zhang et al. 1991) as well as global hybrid simulations of weakly magnetized bodies like e. g., Mars (Böbwetter et al. 2004, Modolo et al. 2006), Venus (Jarvinen et al. 2008) and comets (Bagdonat and Motschmann 2002b).

3.2.1.2 Run 2: VEX orbit 85 – Polar angle $\neq 90$

In general, Run 2 represents the same VEX orbit 85 like the previous Run 1 but the polar angle ϑ has been changed in order to rotate the SIM coordinate system. Since Venus is symmetrical, i. e. typifying an ideal sphere, having no preferential direction, one can rotate the coordinate system. Hence, one can keep the same cutting planes through the simulation box at $X=0$, $Y=0$ and $Z=0$ to ease the comparison between the different runs instead of introducing cuts along tilted planes. In other words, Run 2 represents the same situation like Run 1, but one simply looks at a different location in the simulation box of Run 2 along the respective cutting planes due to the change in the polar angle. The polar angle (or azimuth angle) defines the clockwise angle from the positive Z -direction in VSO (and in SIM), i. e. if $\vartheta = 0^\circ$, the polar angle points northward along the positive Z_{VSO} -axis, if $\vartheta = 90^\circ$, it lies in the equatorial plane, and if $\vartheta = 180^\circ$ it points southward along the negative Z_{VSO} -axis. The polar angle plays an important role in the plasma environment of weakly or non-magnetized planets since it affects the BS asymmetries as well as the location of the pickup ions.

In Run 1 the polar angle was chosen to be 90.0° so that the interplanetary magnetic field lies in the equatorial plane tilted clockwise 67.5° from the positive Y_{SIM} -axis (or clockwise 157.5° from the positive X_{SIM} -axis). Since the solar wind bulk velocity flows along the positive X_{SIM} -axis, the solar wind electric field ($\vec{E} = -\vec{v} \times \vec{B}$) completes the right-hand system being antiparallel to the positive Z_{SIM} -axis. This was the situation in Run 1 in the coordinate system of the simulation (SIM).

For Run 2 a polar angle of 127.5° was determined based on the magnetic field observa-

Parameter	Values	Comments
Solar wind density, n_{sw}	5.0 cm ⁻³	—
Solar wind velocity, v_{sw}	380.0 km s ⁻¹	in x-direction
Magnetic field magnitude, B_{sw}	5.0 nT	in y-direction
IMF orientation, φ_{sw}	-22.5 deg	in VSO
Polar angle, θ_{sw}	127.5 deg	in z-direction pointing into the south hemisphere
Electron beta, $\beta_{e,sw}$	0.81	$T_{e,sw} = 10.0$ eV
Proton beta, $\beta_{i,sw}$	1.61	$T_{i,sw} = 20.0$ eV
Ionospheric electron beta, $\beta_{e,hi}$	0.02	$T_{e,hi} = 0.3$ eV (Miller et al. 1980)
Alfén velocity, v_A	48.77 km s ⁻¹	—
Alfénic Mach Number, M_A	7.79	dimensionless
Sound velocity, c_S	75.81 km s ⁻¹	—
Sonic Mach Number, M_S	5.01	dimensionless
Ionospheric photoionization		
frequency, ν_{smin}	4.55×10^{-7} s ⁻¹	Torr and Torr (1985)
Total ion production, Q_{O^+}	1.037×10^{26} s ⁻¹	Chapman production function
Lower boundary of atmosphere	$1 R_V + 150.0$ km	$R_V = 6051.8$ km
Upper boundary of atmosphere	$2 R_V$	—
Box size, X, Y, Z	$-3 R_V \leq X, Y, Z \leq +3 R_V$	—
Number of grid cells, N_X, N_Y, N_Z	(101, 101, 101)	—
Time step, Δt	2.09 s	—
Total running time, t	1043.97 s	—

Table 3.4: List of simulation parameters used for Run 2 (VEX orbit 85).

tions by averaging the measured values shortly before and after the BS crossing occurred. In this case, the background magnetic field tilted 67.5° from the positive Y_{SIM} -axis is orientated 37.5° out of the equatorial plane pointing into the south hemisphere, which results in a convective electric field that is tilted from the negative Z_{SIM} -axis in order to complete the right-handed system. A more detailed discussion follows below when explaining the 2D cuts of the simulation results. Note that the arrows in the 2D cuts represents not only the direction but also the intensity of the parameter projected onto the respective cutting plane.

Beside the polar angle, the bulk velocity in the undisturbed solar wind region has been changed due to new calibration factors for the IMA data. Thus, the Alfénic Mach Number as well as the Sonic Mach Number also changed insignificantly compared to that used in

Run 1. These different values have only a minor contribution to the simulation results in Run 2.

Figure 3.13, 3.14 and 3.15 display 2D cuts of the 3D simulation results of Run 2 ($t=940s$) in the terminator, polar and equatorial planes, respectively.

Figure 3.13 shows the simulation results of the solar wind density n_{sw} [cm^{-3}], heavy ion density n_{hi} [cm^{-3}] and magnetic field $|B|$ [nT] in the terminator plane.

Like in Run 1, a bow shock is formed upstream of the planet exhibiting a very pronounced shocklet structuring (left plot). Due to the polar angle the interplanetary magnetic field is orientated out of the equatorial plane pointing into the south hemisphere (see right plot) which also changes the direction of the solar wind electric field and hence, the direction of the pickup process. Additionally, the quasi-parallel shock situation occurring on the dawn side (in the sense of orbital motion) of the planet in Run 1 (see left plot in Figure 3.10) disappears in the terminator plane in Run 2.

There is still a dawn-dusk asymmetry visible in the shock geometry but it is smaller than in Run 1 whereas the north-south asymmetry is more significant in Run 2 (left plot). The reason for that is the motional electric field which is still pointing southward but is tilted from the negative z -axis towards the dusk side of the planet where the mass-loading effect decelerates the plasma flow.

The middle plot (heavy ion density) shows the weak ionosphere (small light circle) around the planet with the hot oxygen corona (dark blue region) and the plasma sheet (light blue ray) which lies close to the equatorial plane on the dusk side of Venus due to the used polar angle. The plasma sheet lying in the middle of the magnetic lobes of the induced magnetotail (right plot) has also been rotated since the polar angle is not 90 degree in this run.

Figure 3.14 illustrates the simulation results of the solar wind density n_{sw} [cm^{-3}] and velocity $|v_{sw}|$ [$km\ s^{-1}$], heavy ion density n_{hi} [cm^{-3}] and velocity $|v_{hi}|$ [$km\ s^{-1}$], the magnetic field $|B|$ [nT] and the solar wind electric field $|E|$ [$V\ km^{-1}$] in the polar plane. The

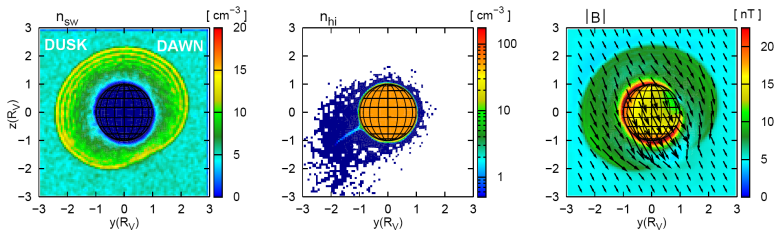


Figure 3.13: Simulation results of Run 2 in the terminator plane, i. e. one looks from tailside towards Venus. The solar wind is orientated out of the plane ($+x$ -axis), the background magnetic field is tilted 127.5° from the $+z$ -axis pointing into the south hemisphere and the convective electric field completes the right-handed system pointing to the dusk side (in the sense of orbital motion) of the planet. The figures display from left to right the solar wind density (n_{sw}), the heavy ion density (n_{hi}) and the background magnetic field.

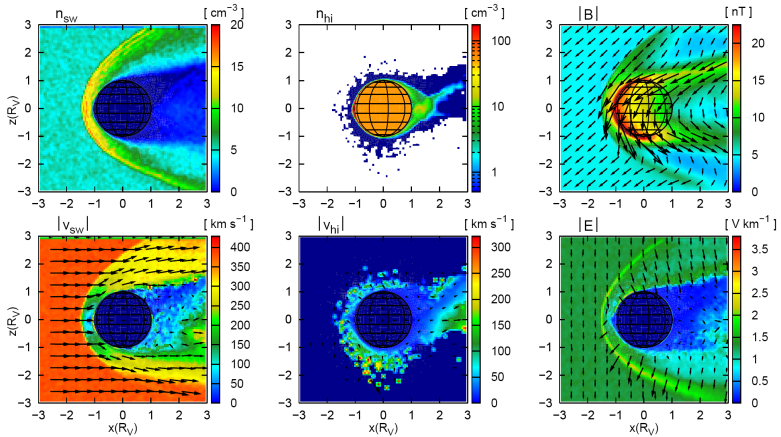


Figure 3.14: Cut through the simulation box of Run 2 along the polar plane, i. e. one looks from the western (dusk) side (in the sense of orbital motion) towards Venus. The plasma flow comes in from the left (+x-axis), the interplanetary magnetic field (IMF) points into the plane but is tilted from the +y-axis according to the polar (127.5°) and IMF (157.5°) angles, while the convection electric field completes the right-handed system pointing away from the planet close to the equatorial region on the dusk side of the planet. The figures illustrate from left to right in the first row the solar wind density (n_{sw}), the heavy ion density (n_{hi}) and the background magnetic field; and in the second row the solar wind bulk velocity ($|v_{sw}|$), heavy ion bulk velocity ($|v_{hi}|$) and the convective electric field.

cut through the polar plane showing the dusk side of Venus in Run 2 mirrors the features appearing in the equatorial plane in Run 1 (see Figure 3.12) which is a consequence of the polar angle being 127.5° in the present case instead of $\vartheta=90.0^\circ$.

In the solar wind density plot, one can see clearly the asymmetrical form of the bow shock with its multiple shocklets. The panel below shows the solar wind velocity which decreases significantly behind the shock, especially in the subsolar region, defining the magnetosheath domain.

The heavy ion density picture demonstrates that the maximum of the ionospheric production takes place at the subsolar point where the solar EUV radiation causes the maximum ionization. Additionally, a hot oxygen corona is present around the planet which interacts directly with the oncoming solar wind flow, and behind the obstacle a plasma wake is formed filled with planetary particles. In contrast to Run 1 (see $|v_{hi}|$ in Figure 3.11), the pickup process does not take place in the polar plane in Run 2 which is expressed by the small arrows and arrowheads reflecting the direction and strength of the heavy ion velocities in this cutting plane. The planetary ions are picked up on the dusk side of the planet between the polar and equatorial plane but closer to the equatorial plane which is

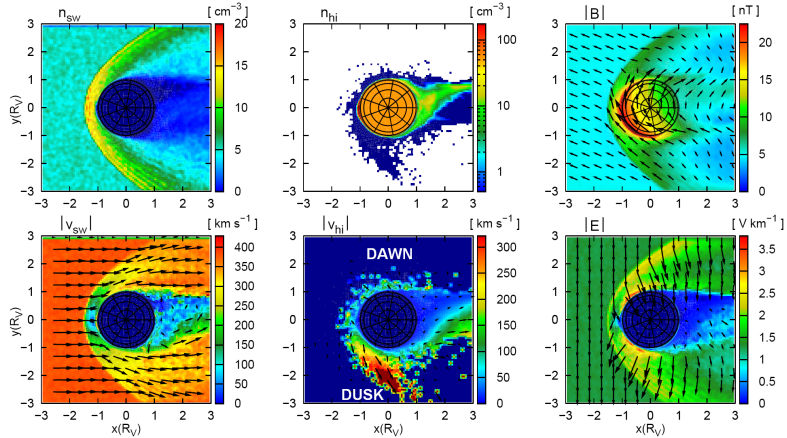


Figure 3.15: Simulation results of Run 2 in the equatorial plane, i. e. one looks from ecliptic North towards Venus. The undisturbed solar wind flow is parallel to the positive x -axis, the background magnetic field is tilted clockwise 67.5° from the positive y -axis and is orientated 37.5° out of the equatorial plane pointing into the south hemisphere due to the polar angle (127.5°). The solar wind electric field points into the plane but is tilted from the negative z -axis towards the dusk side (in the sense of orbital motion) of Venus in order to complete the right-handed system. The figures show from left to right in the first row the solar wind density (n_{sw}), the heavy ion density (n_{hi}) and the background magnetic field; and in the second row the solar wind bulk velocity ($|v_{sw}|$), heavy ion bulk velocity ($|v_{hi}|$) and the convective electric field.

demonstrated in $|v_{hi}|$ of Figure 3.15.

Unlike Run 1 (see $|B|$ in Figure 3.11), the induced magnetotail with its 2 lobes of opposite polarities (see arrows) lies almost in the polar plane which is displayed by $|B|$. The interplanetary magnetic field piles up in front of the obstacle expressed by the red colouring ($|B| > 20\text{nT}$) and drapes around the planet creating the magnetotail which is tilted towards the polar plane.

Figure 3.15 represents the simulation results of the solar wind density n_{sw} [cm^{-3}] and velocity $|v_{sw}|$ [km s^{-1}], heavy ion density n_{hi} [cm^{-3}] and velocity $|v_{hi}|$ [km s^{-1}], the magnetic field $|B|$ [nT] and the solar wind electric field $|E|$ [V km^{-1}] in the equatorial plane. The cut through the equatorial plane of the simulation box looking from the ecliptic North onto Venus in Run 2 reflects the plasma features occurring in the polar plane in Run 1 (see Figure 3.11) due to the rotation of the SIM coordinate system by using a different polar angle.

In the equatorial cutting plane the shock geometry as well as the shocked solar wind flow are almost symmetric (see n_{sw} and $|v_{sw}|$) which are similar to the solar wind density and

velocity pictures of Run 1 in Figure 3.11 (polar plane).

The denotation E^+ hemisphere for the North hemisphere or E^- hemisphere for the South hemisphere cannot be used in Run 2 for interpreting the simulation results since the polar angle also affects the direction of the solar wind electric field. Here, the convection electric field does not point exactly into the xy -plane along the $-z$ -axis but is tilted from it in the direction of the dusk side of the planet. In the heavy ion velocity plot one can see how the planetary particles are accelerated in the direction of the motional electric field and picked up by the solar wind which takes place close to the equatorial plane.

The picture of $|E|$ illustrates that the convection electric field points approximately towards the planet on the dawn side and is orientated away from the planet on the dusk side of Venus. Thus, the formation of the ICB occurs almost in the equatorial plane on the dawn side as can be seen by comparing $|n_{sw}|$ and $|n_{hi}|$ since the solar wind electric field and the electron pressure forces are antiparallel in that area. However, the ICB is not so sharp in Run 2 compared with that found in Run 1 because both forces are tilted out of the equatorial plane simply due to the rotation of the SIM coordinate system in Run 2.

Like Run 1, demonstrates Run 2 the asymmetric behaviour of the magnetic field intensity, i. e. the interplanetary magnetic field piles up preferably on the dusk side of Venus due to the mass-loading effect which decelerates the plasma flow. Additionally, the magnetic field draping is also visible (see arrows) in this cutting plane because the magnetotail lies between the polar and equatorial plane.

In summary, Run 2 shows the same features as produced in Run 1 but the whole global plasma environment is rotated due to the polar angle of 127.5° . In other words, we would get similar 2D cuts from the simulation outputs of Run 1 by cutting the results of Run 1 along tilted planes. However, it is more convenient to keep the same cutting planes in order to ease the comparison between the presented runs. Thus, the polar angle is used for the obliquity rather than cutting along tilted planes.

3.2.2 Comparison of simulation results: solar minimum (Run 1) vs. solar maximum (Run 3)

The PVO mission provided measurements over more than a complete solar cycle and thus, also a simulation for high solar activity was carried out (Run 3) in order to compare it with the simulation results (Run 1) based on VEX parameters measured at low solar activity. Table 3.5 shows typical solar wind density and velocity as well as magnetic field strength and orientation for solar maximum conditions as observed by PVO.

In Run 3 the Venusian atmosphere was modeled by including atmospheric and exospheric exponential profiles valid for high solar activity which are taken from Hedin et al. (1983) (cold oxygen) and Nagy et al. (1990) (hot oxygen), respectively. Both profiles are shown in Figure 3.16. By using the neutral profile in combination with an ionospheric photoionization frequency of $\nu_{smax}=1.35 \times 10^{-6} \text{s}^{-1}$ (Torr and Torr 1985) one obtains by means of the chapman production function, explained in subsection 2.2.6, the ion production profiles of the day- and nightside of the planet for solar maximum conditions as demonstrated in Figure 3.17.

Figures 3.18, 3.19 and 3.20 represents the 2D cuts of the simulation results of Run 3 at the cutting planes $X=0$ (terminator plane), $Y=0$ (polar plane) and $Z=0$ (equatorial plane), respectively. The similarities and differences of the global Venusian plasma environment

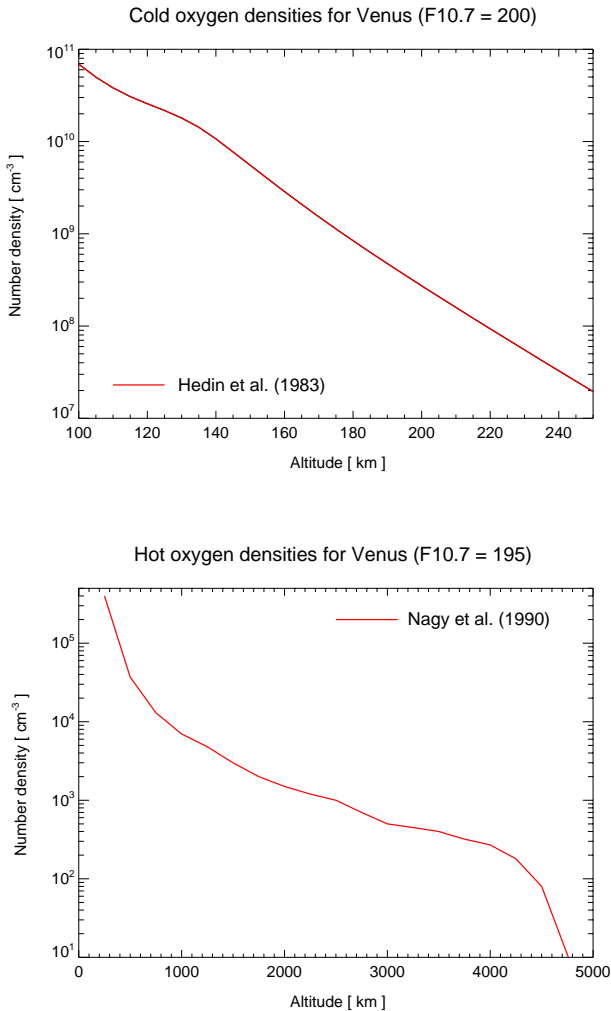


Figure 3.16: Cold O and hot O* number densities as a function of altitude (km). The upper panel shows the density profile of cold atomic oxygen at Venus for high solar activity ($F_{10.7cm}=200 \times 10^{-22} \text{ W m}^{-2} \text{ Hz}^{-1}$) based on the model of Hedin et al. (1983). The lower panel shows the density profile of hot atomic oxygen at Venus for high solar activity ($F_{10.7cm}=195 \times 10^{-22} \text{ W m}^{-2} \text{ Hz}^{-1}$) based on Pioneer Venus Orbiter (PVO) measurements (Nagy et al. 1990).

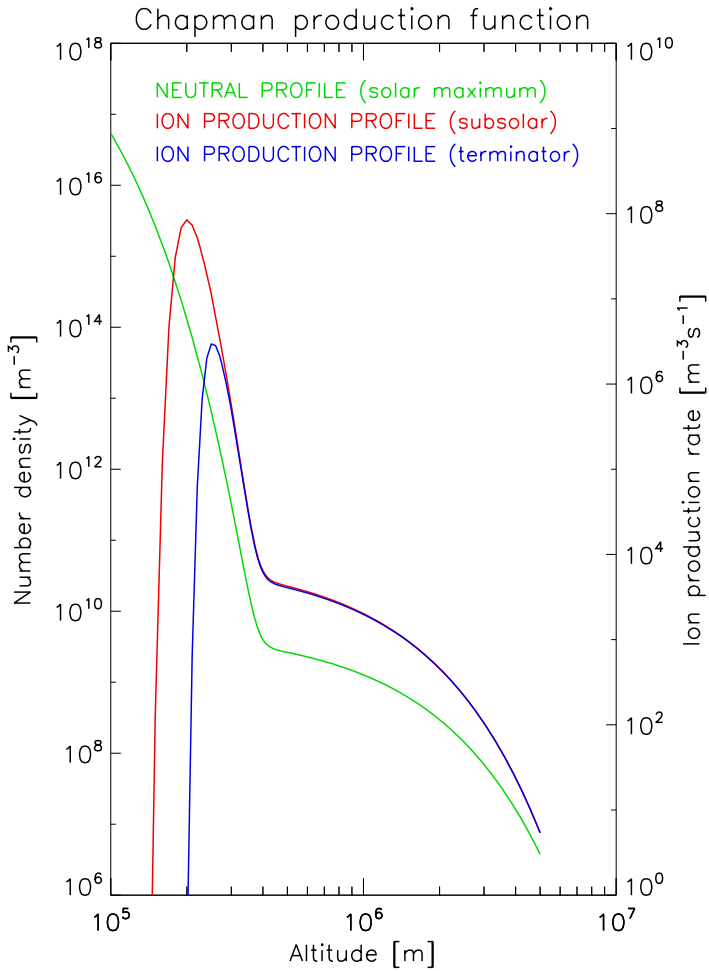


Figure 3.17: The neutral number density (green line) and the ion production rate (red line in subsolar direction and blue line at the terminator) of oxygen as a function of altitude at solar maximum (ionospheric photoionization frequency $\nu_{smax}=1.35 \times 10^{-6} \text{ s}^{-1}$ (Torr and Torr 1985)).

Parameter	Values	Comments
Solar wind density, n_{sw}	18.0 cm ⁻³	—
Solar wind velocity, v_{sw}	400.0 km s ⁻¹	in x-direction
Magnetic field magnitude, B_{sw}	12.0 nT	in y-direction
IMF orientation, φ_{sw}	38.0 deg	in VSO
Polar angle, θ_{sw}	90.0 deg	in z-direction lying in the equatorial plane
Electron beta, $\beta_{e,sw}$	1.50	$T_{e,sw} = 29.80$ eV
Proton beta, $\beta_{i,sw}$	0.43	$T_{i,sw} = 8.62$ eV
Ionospheric electron beta, $\beta_{e,hi}$	0.02	$T_{e,hi} = 0.30$ eV (Miller et al. 1980)
Alfén velocity, v_A	61.69 km s ⁻¹	—
Alfénic Mach Number, M_A	6.48	dimensionless
Sound velocity, c_S	85.79 km s ⁻¹	—
Sonic Mach Number, M_S	4.66	dimensionless
Ionospheric photoionization		
frequency, ν_{smax}	1.35×10^{-6} s ⁻¹	Torr and Torr (1985)
Total ion production, Q_{O^+}	1.002×10^{27} s ⁻¹	Chapman production function
Lower boundary of atmosphere	$1 R_V + 150.0$ km	$R_V = 6051.8$ km
Upper boundary of atmosphere	$2 R_V$	—
Box size, X, Y, Z	$-3 R_V \leq X, Y, Z \leq +3 R_V$	—
Number of grid cells, N_X, N_Y, N_Z	(101, 101, 101)	—
Time step, Δt	0.87 s	—
Total running time, t	434.99 s	—

Table 3.5: List of simulation parameters used for Run 3 based on PVO measurements.

at low and high solar activity obtained by the hybrid model are discussed with respect to the 2D cuts of simulation results of Run 1 based on the VEX parameters observed close to solar minimum. Like in Run 1, the interplanetary magnetic field vector lies in the equatorial plane due to the polar angle of 90.0°. But in contrast to Run 1, the cone angle φ , which is the angle between the solar wind flow and IMF direction, is -142.0° in SIM (38.0° in VSO), so that the solar wind electric field is not aligned with the negative z-axis but is orientated opposite to it (+z-axis) in Run 3 (see $|E|$ plot in Figure 3.19).

In Figure 3.18 are displayed from left to right the solar wind density n_{sw} [cm⁻³], heavy ion density n_{hi} [cm⁻³] and the magnetic field $|B|$ [nT] along the terminator plane, where the solar wind is orientated out of the plane (+x-axis), the convective electric field points into +z-axis and the background magnetic field completes the right-handed system.

As can be seen in the solar wind density plot, again a significant dawn-dusk bow shock asymmetry is produced but compared with that generated in Run 1 (see left plot in Figure 3.10) it is in opposite direction due to the IMF angle of -142.0° . Also a small asymmetry with respect to the north-south direction occurs but this time the shock is further away in the north hemisphere, since the solar wind electric field is parallel to the positive z -axis where the mass-loading effect decelerates the plasma flow as demonstrated by the heavy ion density picture.

If one compares the terminator shock distance (r_{tsd}) in both runs, one finds that the shock is further away from the planet at high solar activity due to the higher ionization and pickup rates caused by EUV flux changes over the 11-year solar cycle. This solar cycle variation of the Venusian bow shock location has already been discussed in the course of the data analysis in subsection 3.1.3.2. Run 3 produces $r_{tsd} \sim 2.4R_V$ in the south (E^-) hemisphere which is in agreement with the study of Russell et al. (1988) based on PVO observations ($r_{tsd} = 2.4R_V$). Furthermore, they demonstrated that the shock is farthest from the planet on the side in which the newly created ions gyrate away from the ionosphere, namely in the direction of the motional electric field, as already mentioned above. In Run 3 the shock occurs at $\sim 2.5R_V$ in the north (E^+) hemisphere and is therefore also consistent with spacecraft observations. In Run 1 the terminator shock distance appears at $\sim 2.1R_V$ and $\sim 2.2R_V$ in the north (E^-) and south (E^+) hemisphere, respectively, which is in agreement with an average distance of $r_{tsd} = 2.088R_V$ obtained by ASPERA-4 observations (see Table 3.1) where all bow shock crossings were extrapolated to the terminator plane under the assumption of symmetrical symmetry. Russell et al. (1988) and Zhang et al. (2008a) found $r_{tsd} = 2.14R_V$ for low solar activity based on PVO measurements which is very similar to the shock distance determined in this thesis. The small difference in the absolute value is caused by the fact that in the previous investigations (Russell et al. 1988, Zhang et al. 2008a) a 2-parameter conic function was used while in this study a 3-parameter conic section was applied as discussed in subsection 3.1.5.

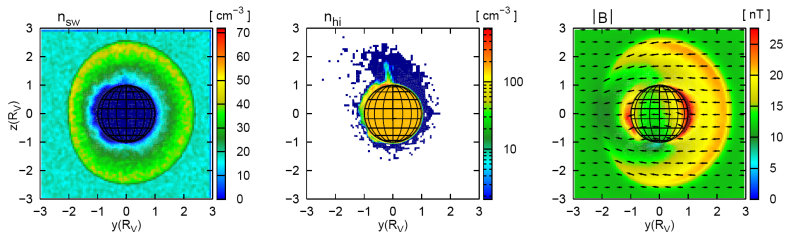


Figure 3.18: Simulation results of Run 3 in the terminator plane, i. e. one looks from tailside towards Venus. The solar wind is orientated out of the plane ($+x$ -axis), the convective electric field is parallel to the ($+z$ -axis) and points away from the planet and thus, the background magnetic field completes the right-handed system ($-y$ -axis). The figures display from left to right the solar wind density (n_{sw}), the heavy ion density (n_{hi}) and the background magnetic field.

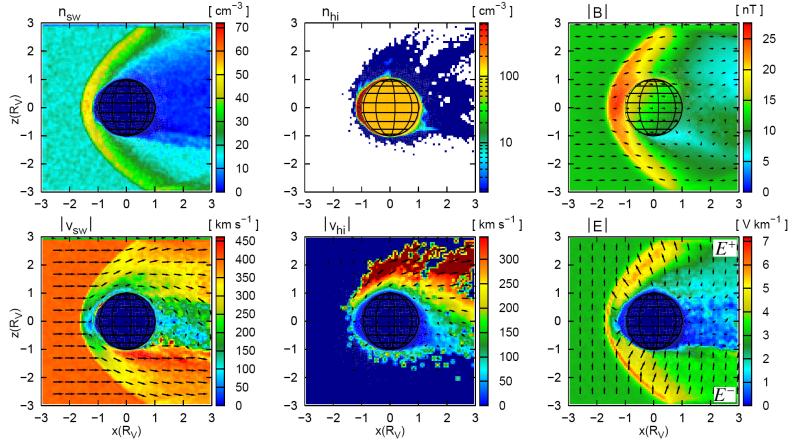


Figure 3.19: Cut through the simulation box of Run 3 along the polar plane, i. e. one looks from the western (dusk) side (in the sense of orbital motion) towards Venus. The plasma flow comes in from the left (+ x -axis), the solar wind electric field points away from the planet (+ z -axis) and the interplanetary magnetic field completes the right-handed system pointing out of the plane (- y -axis). The figures illustrate from left to right in the first row the solar wind density (n_{sw}), the heavy ion density (n_{hi}) and the background magnetic field; and in the second row the solar wind bulk velocity ($|v_{sw}|$), heavy ion bulk velocity ($|v_{hi}|$) and the convective electric field.

Figure 3.19 shows the simulation results of the solar wind density n_{sw} [cm^{-3}] and velocity $|v_{sw}|$ [km s^{-1}], heavy ion density n_{hi} [cm^{-3}] and velocity $|v_{hi}|$ [km s^{-1}], the magnetic field $|B|$ [nT] and the solar wind electric field $|E|$ [V km^{-1}] in the polar plane.

As already discussed above, the bow shock location varies with the solar cycle. This is also demonstrated in the solar wind density picture where the shock distance at the subsolar point r_{ssp} is $\sim 1.6R_V$ while r_{ssp} occurs at $\sim 1.4R_V$ in Run 1 during solar minimum (see n_{sw} in Figure 3.11). By comparing the subsolar shock distances derived from the simulation with data at low solar activity, one finds a good agreement with the 3-parameter bow shock model determined in this thesis based on the ASPERA-4 observations ($r_{ssp}=1.4R_V$) as can be seen in Figure 3.6. The shock models based on PVO measurements obtained by Russell et al. (1988) and Zhang et al. (2008a) provide a similar value of $r_{ssp}=1.32R_V$ using a 2-parameter conic section. In Run 3 r_{ssp} is located at $\sim 1.6R_V$ which is close to PVO observations investigated by Russell et al. (1988) yielding $r_{ssp}=1.5R_V$ during solar maximum.

During solar maximum the atmosphere is more strongly ionized due to higher solar EUV radiation which is shown by the heavy ion density picture where the ionosphere extends over a larger volume on the dayside of the planet than at low solar activity. Additionally,

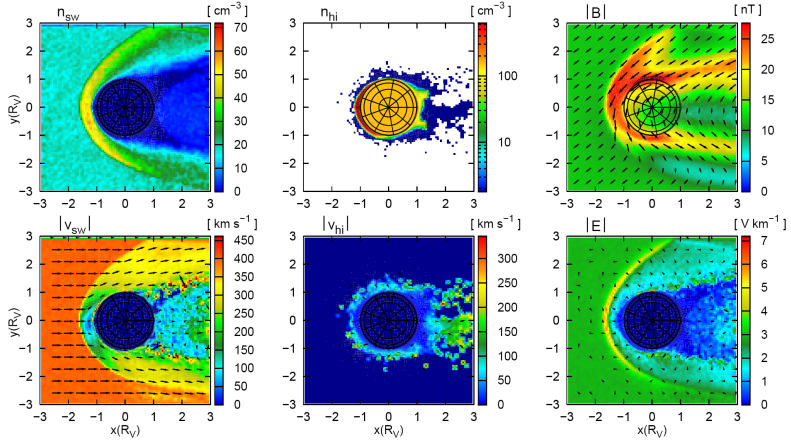


Figure 3.20: Simulation results of Run 3 in the equatorial plane, i. e. one looks from ecliptic North towards Venus. The undisturbed solar wind flow is parallel to the positive x -axis, the convective electric field points out of the plane ($+z$ -axis) and the background magnetic field completes the right-handed system ($-y$ -axis) and is tilted -142.0° in the equatorial plane. The figures show from left to right in the first row the solar wind density (n_{sw}), the heavy ion density (n_{hi}) and the background magnetic field; and in the second row the solar wind bulk velocity ($|v_{sw}|$), heavy ion bulk velocity ($|v_{hi}|$) and the convective electric field.

the ionospheric densities on the dayside and nightside of Venus are significantly larger in Run 3 than in Run 1. As already mentioned in subsection 1.1.6, the nightside ionosphere is maintained by plasma transport from the dayside due to pressure gradients (=main source during solar maximum) and low energy electron impact ionization. However, the horizontal nightward flow is reduced during solar minimum since the ionopause is located at lower altitudes ($z < 300$ km) resulting from the combination of a high ram pressure and low solar EUV radiation (Brace and Kliore 1991). At low solar activity, most of the upper ionosphere is removed resulting in an ill-defined ionospheric nightside which is maintained mainly by energetic electron precipitation at that time.

Like in Run 1, an ICB is formed in the E^- (south) hemisphere of Venus (see $|v_{sw}|$ panel) due to the antiparallelism of the solar wind electric field and electron pressure forces as explained in subsection 3.2.1.1. The planetary ions are accelerated by the convection electric field and therefore, picked up in the E^+ (north) hemisphere. Consequently, the mass-loading effect decelerates the plasma in the region in which the convective electric field is pointing, so that the interplanetary magnetic field is preferably piled up in the E^+ hemisphere as illustrated by the magnetic field intensity $|B|$.

Figure 3.20 demonstrates the simulation results of the solar wind density n_{sw} [cm⁻³] and velocity $|v_{sw}|$ [km s⁻¹], heavy ion density n_{hi} [cm⁻³] and velocity $|v_{hi}|$ [km s⁻¹], the

magnetic field $|B|$ [nT] and the solar wind electric field $|E|$ [$V \text{ km}^{-1}$] in the equatorial plane.

Unlike Run 1, there are no kinetic shock substructures behind the asymmetric bow shock visible in the solar wind density picture (see also n_{sw} in Figures 3.18 and 3.19) due to the small proton inertial length (=sound speed/proton plasma frequency). In Run 3 the proton inertial length is ~ 54 km and thus, multiple shocklets cannot be resolved since the grid cell resolution is around 250-300 km per cell outside in the solar wind region (see subsection 2.2.3). In Run 1 the shocklet structuring can be resolved since the proton inertial length is ~ 102 km due to the lower background density.

The heavy ion density panel displays the pronounced ionosphere on the day- and nightside as already discussed above but the plasma wake has not been fully developed yet. The simulation results shown in this subsection are snapshots of the timestep 25000 ($t=435$ s). The undisturbed solar wind went 20 times through the simulation box and thus, switch on effects are not present any more and a quasi-stationary state has already been reached. However, this simulation would need probably double time in order to generate a well developed wake region as seen in the previous runs but this would imply a simulation running time of almost 6 months.

As already discussed in the course of the previous runs, the interplanetary magnetic field drapes over the obstacle on the dayside and produces an induced magnetotail on the nightside of the planet consisting of 2 lobes with opposite polarity (see arrows) as shown in $|B|$. These features are more pronounced in Run 3 than in Run 1 due to the higher background values at high solar maximum. Due to the IMF angle of -142.0° in Run 3, the quasi-parallel shock occurs on the dusk side and the quasi-perpendicular shock on the dawn side of the planet while it is the opposite case in Run 1.

In summary, when comparing the simulation results based on solar minimum and maximum conditions, it is obvious that Venus is very dependent on the phase of solar cycle as we already know from spacecraft missions. Moreover, the orientation of the interplanetary magnetic field vector and thus, the direction of the solar wind electric field play important roles for the pickup process and escape mechanisms at Venus. All simulation runs (Run 1, Run 2 and Run 3) exhibit similar plasma boundaries, regions and features occurring in the global environment of Venus, which are in fairly good agreement with spacecraft observations. Thus, the simulation results demonstrate that the 3D hybrid model is able to provide an adequate picture of the global plasma processes at Venus.

4 Comparison of observations and simulations

In this chapter the simulation results are compared with the plasma and magnetic field measurements made on board VEX. In order to discuss the parameters as a function of spacecraft time, cuts through the simulation box were taken along the VEX trajectory of the concerned orbits. All data have been resampled with one-minute resolution. Additionally, the positions of the plasma boundaries are marked by dashed vertical lines, namely the bow shock and the upper and lower boundary of the transition zone. In the last subsection the atmospheric escape rates of oxygen derived from the simulations are compared with estimated loss rates obtained by theoretical models and spacecraft observations.

4.1 VEX orbit 85 vs. Run 1

A comparison between observations made on 15 July 2006 and simulation results of Run 1 are shown in Figures 4.1, 4.2, 4.4, 4.5 and 4.6.

Figure 4.1 displays the comparison of the solar wind bulk velocity (v_x , v_y , v_z and $|v_{sw}|$) derived from the simulation and observed by the IMA sensor. The Y- and Z-components of the measured bulk velocity are not well determined because the IMA sensor does not have a full 3D view, i. e. large part of the field of view is blocked by the spacecraft. Note that IMA lost the signal (ion beam) after around 02:30 UT because the sensor was looking into the wrong spatial direction. Thus, it is not possible to calculate a reliable integrated velocity on the outbound pass. Furthermore, the integrated bulk velocity inside the ionosphere (\sim 01:57 – 02:01 UT), exhibiting unrealistic high values, is determined only by the background noise because the physical and measured density is close to zero in this region and therefore, should be taken into account when comparing with the simulated velocity.

The simulation is more or less in agreement with the data, except for the transition zone and ionosphere where IMA does not resolve the double peak feature which is visible in the simulation. The source of this disagreement could be the location of accelerated shocked solar wind plasma after the terminator (see Figure 3.11, $|v_{sw}|$) as well as the polar projection in Figure 3.7). That means, in the simulation the spacecraft would transit this region of accelerated plasma during the inbound pass, traverse the ionosphere (sharp drop in bulk velocity) and then, cross the fast plasma flow once again during the outbound pass. Though we never observe proton bulk speeds larger than the solar wind speed in the transition zone. Probably the solar wind electric field is much weaker in reality because of the fluctuating magnetic field.

The positions of the plasma boundaries are well reproduced by the hybrid model, however, there are significant discrepancies regarding the absolute values of plasma parameters in the magnetosheath.

Figure 4.2 displays the comparison of the heavy ion velocity (v_x , v_y , v_z and $|v_{HI}|$) obtained by the simulation and measured by the IMA sensor. The peaks of the simulated heavy ion velocity in the mantle and magnetosheath region shown in the bottom panel could originate from pickup ions, tail rays or plasma clouds which the spacecraft would traverse on its orbit. It is very difficult to determine reliable heavy ion velocities with ASPERA. In the ionosphere what we actually measure is the ram velocity of the spacecraft (~ 9 km/s) which is shown in the bottom panel in Figure 4.3. After correction of the negative spacecraft potential (~ 11 eV \pm 2) derived from the ELS data (see third panel in Figure 4.3) one can estimate only an upper limit for the heavy ion velocity which seems to be not larger than 3 km/s for orbit 85.

The upper panel in Figure 4.4 shows the comparison of the heavy ion density obtained by the simulation and measured by the IMA sensor which shows a significant discrepancy in absolute values. Although the simulated and the observed densities exhibit a peak in the ionosphere, both densities clearly underestimate the real planetary density. In the simulated ionosphere the radial density gradient is extremely high and the spatial resolution of the simulation grid yields always mean values over 100 km in radial distance reducing the maximum values of the heavy ion density. Thus, the planetary densities produced in the hybrid model are about a factor of 100 less than the observed values (PVO measurements). The integrated density derived from IMA measurements gives only a lower estimate for the total heavy ion density for the terminator region because the sensor saturates whenever the count rates are larger than 10^4 per energy step (120ms), which is the case in the ionosphere.

The lower panel in Figure 4.4 compares the solar wind density extracted from the simulation with the fitted density measured by the ELS sensor which shows for the most part a good agreement between data and model (from 01:48 till 03:20 UT) regarding the plasma boundaries as well as the absolute value, while on the outbound pass the agreement is almost perfect. During the inbound pass, in the solar wind and magnetosheath regions, there is a large difference between the simulated and measured densities due to the quasi-parallel shock. Although the features are similar, the absolute values do not match the observations, maybe also due to limited field of view of the instrument.

Figure 4.5 compares the magnetic field components (B_x , B_y , B_z and $|B|$) extracted from the simulation with the measured value obtained by the Magnetometer along the spacecraft orbit. Most of the features are at least in qualitative agreement, i. e. plasma boundary positions are well reproduced by the simulation, especially on the outbound pass. However, there are some disagreements regarding the absolute value where the real physics is still more complex than our model.

The simulated B_z fluctuates around zero and is significantly in disagreement with the observed Z-component due to the fact, that in Run 1 the polar angle was chosen to be 90.0 degree, i. e. lying in the equatorial plane.

During the inbound pass the simulation does not exhibit the jump in the magnetic field, indicating the BS crossing which is visible in the data. By comparing the VEX trajectory in Figure 3.7 with the simulation results in the terminator plane (see Figure 3.10) one can see clearly that this originates from the quasi-parallel shock situation. In the simulation

we assumed a constant IMF angle of -22.5° (in VSO) but in reality the magnetic field orientation is strongly fluctuating. Our constant magnetic field boundary is an oversimplification.

Figure 4.6 compares the components of the convective electric field (E_x , E_y , E_z and $|E|$) extracted from the simulation with the observed values derived from the Magnetometer and ASPERA-4 ($\vec{E} = -\vec{v} \times \vec{B}$) along the VEX trajectory which also demonstrates that the hybrid model is able to reproduce the positions of the plasma boundaries. However, the absolute values from the simulation differ significantly from the observed values. One reason is that the Y- and Z-components of the bulk velocity cannot be well determined because the field of view of IMA is very restricted due to the spacecraft shadow. Another reason is that the IMF and polar angles are assumed to be completely homogeneous in the simulation while both angles are fluctuating in reality.

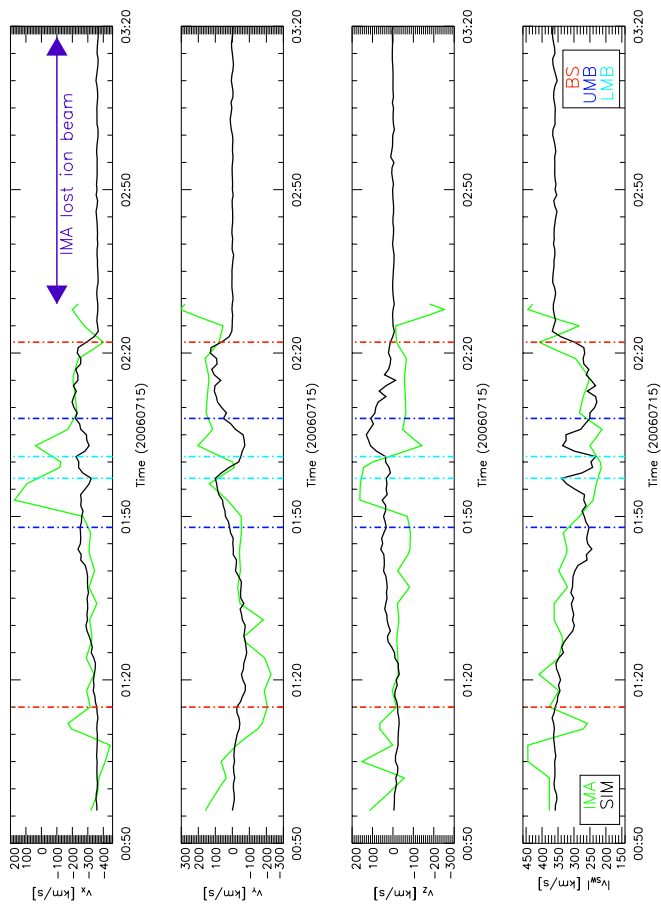


Figure 4.1: Comparison of the solar wind bulk velocity (v_x , v_y , v_z and $|v_{sw}|$) derived from the simulation Run 1 (black line) with IMA data (green line; integrated velocity) along VEX orbit 85 on 15 July 2006, from inbound to outbound. Additionally, the positions of the plasma boundaries (red: bow shock, dark blue: upper mantle boundary, light blue: lower mantle boundary (=ICB)) are marked by dashed vertical lines.

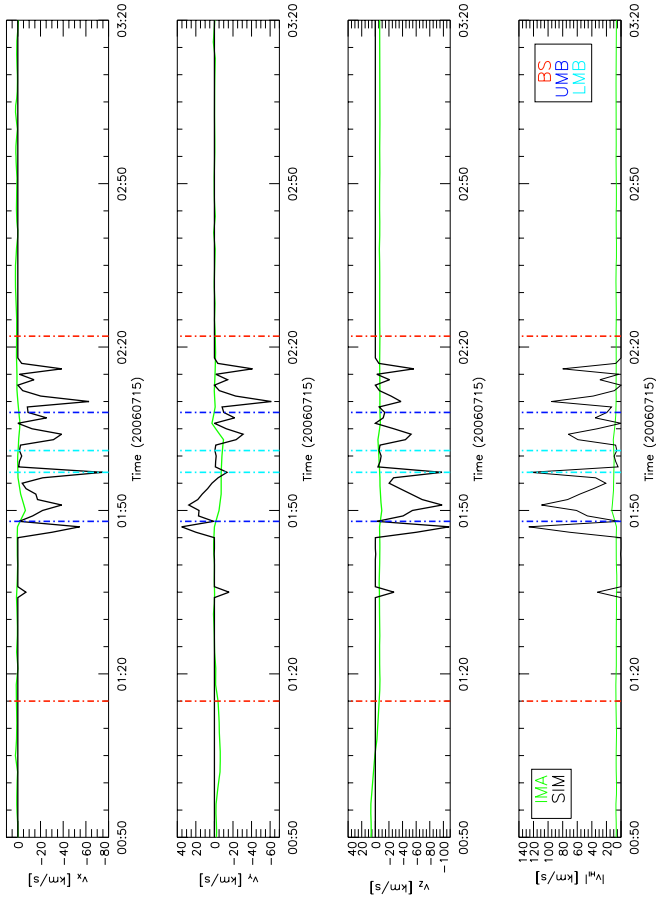


Figure 4.2: Comparison of the heavy ion velocity (v_x , v_y , v_z and $|v_{HI}|$) derived from the simulation Run 1 (black line) with IMA data (green line; integrated velocity) along VEX orbit 85 on 15 July 2006, from inbound to outbound. In addition, the positions of the plasma boundaries (red: bow shock, dark blue: upper mantle boundary, light blue: lower mantle boundary (=ICB)) are marked by dashed vertical lines.

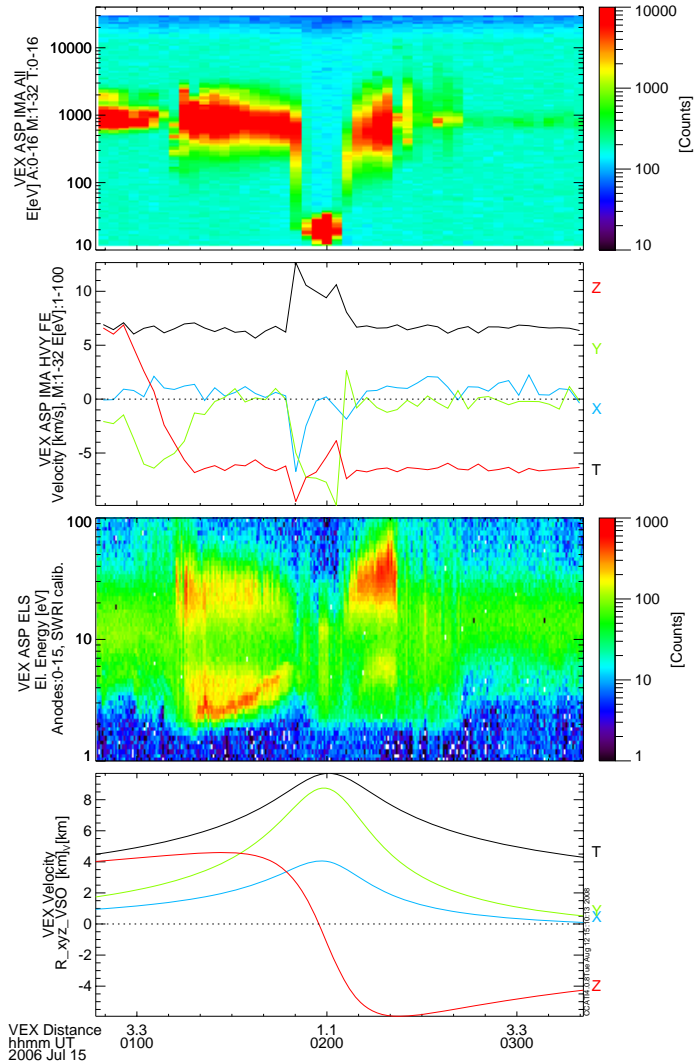


Figure 4.3: VEX orbit 85: 15 July 2006, 00:47 – 03:21 UT. The first panel shows the total counts of all ion channels of the IMA sensor. The second panel presents the integrated velocity (X-, Y-, Z- and Total-components) of the heavy ions. The third panel illustrates the total counts of energetic electrons measured by the ELS sensor. The fourth panel shows the X-, Y-, Z- and Total-components of the ram velocity of the VEX spacecraft.

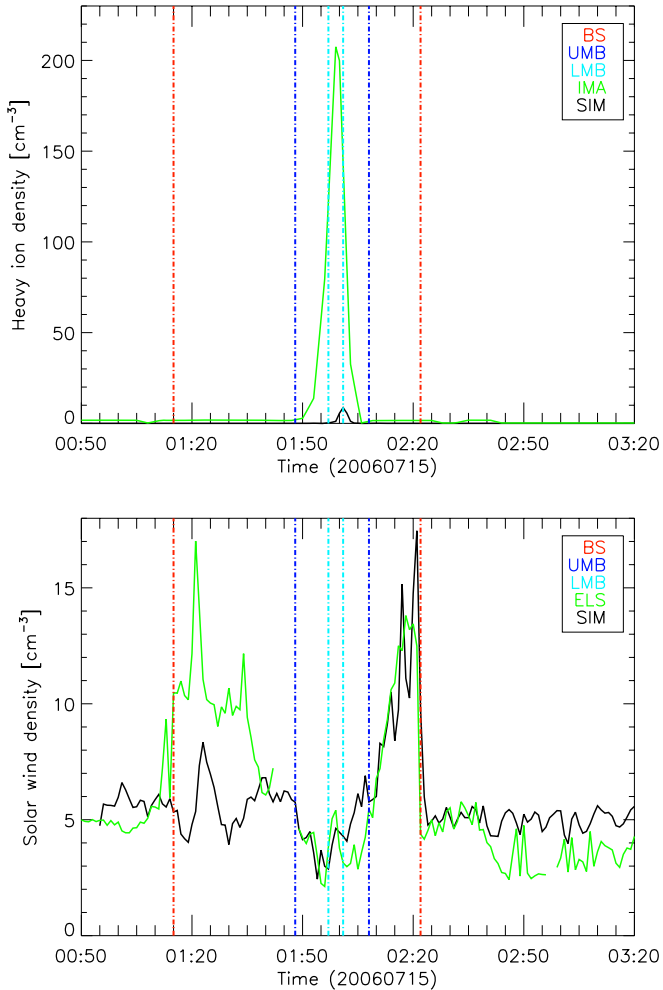


Figure 4.4: **Upper panel:** Comparison of the heavy ion density derived from the simulation Run 1 (black line) with IMA data (green line; integrated density) along VEX orbit 85 on 15 July 2006, from inbound to outbound. **Lower panel:** Comparison of the solar wind density from the simulation Run 1 (black line) with ELS data (green line; fitted density) along VEX orbit 85 on 15 July 2006, from inbound to outbound. Additionally, the positions of the plasma boundaries (red: bow shock, dark blue: upper mantle boundary, light blue: lower mantle boundary (=ICB)) are marked by dashed vertical lines.

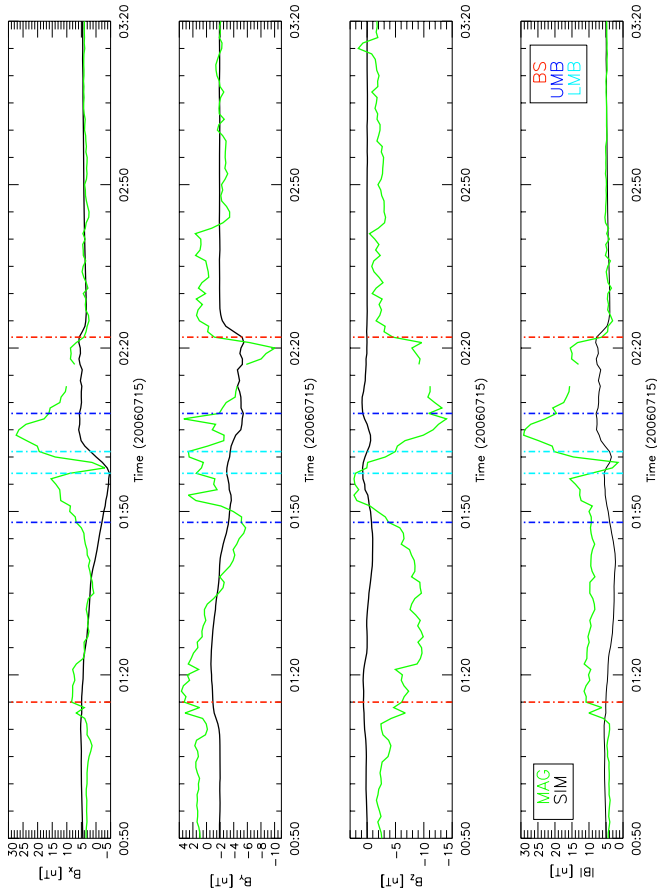


Figure 4.5: Comparison of the magnetic field parameter (B_x , B_y , B_z and $|B|$) derived from the simulation Run 1 (black line) with the Magnetometer data (green line) along VEX orbit 85 on 15 July 2006, from inbound to outbound. In addition, the positions of the plasma boundaries (red: bow shock, dark blue: upper mantle boundary, light blue: lower mantle boundary (=ICB)) are marked by dashed vertical lines.

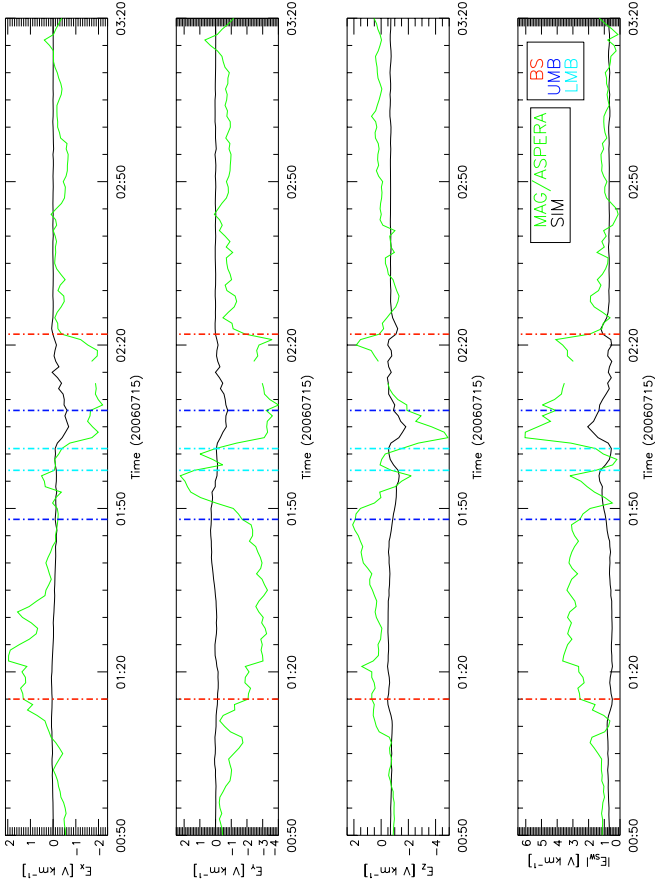


Figure 4.6: Comparison of the electric field parameter ($\vec{E} = -\vec{v} \times \vec{B}$; E_x , E_y , E_z and $|E|$) derived from the simulation Run 1 (black line) with the Magnetometer-ASPERA data (green line) along VEX orbit 85 on 15 July 2006, from inbound to outbound. Additionally, the positions of the plasma boundaries (red: bow shock, dark blue: upper mantle boundary, light blue: lower mantle boundary (=ICB)) are marked by dashed vertical lines.

4.2 VEX orbit 85 vs. Run 2

In Figures 4.7, 4.8, 4.9 and 4.10 the simulation results derived from Run 2 are compared with the VEX observations made on 15 July 2006 which is the same orbit as in Run 1. The main difference between both runs is the orientation of the SIM coordinate system and thus, the orientation of the interplanetary magnetic field vector which results in slightly different plasma configurations as will be shown below. Due to the polar angle of 90° in Run 1 the IMF lies in the equatorial plane, while the polar angle is 127.5° in Run 2 - causing the IMF to be orientated out of the equatorial plane pointing into the south hemisphere (as explained in subsection 3.2.1.2).

Figure 4.7 shows the comparison of the solar wind density derived from the simulation and measured by the ELS sensor. The model matches relatively well the data regarding the absolute values between 02:05 and 03:20 UT, whereas the bow shock crossing on the outbound pass occurs around 7 minutes later in the simulation than observed by VEX while it was in agreement in Run 1. In contrast to Run 1, there is a jump in the simulated solar wind density around 01:05 UT marking the inbound shock crossing since no quasi-parallel shock occurs in Run 2 on the dawn side of the planet due to the polar angle. However, the bow shock appears around 10 minutes earlier than seen by VEX. Thus, the bow shock positions are displaced by a few minutes in Run 2 because the shock moved a little bit further away from the planet on the dawn and dusk side (compare Figures 3.10 and 3.13 showing the terminator 2D cuts of Run 1 and 2) due to the rotated SIM coordinate system in Run 2. Another difference caused by the polar angle is that the simulated proton density is decreasing in the mantle region (inbound), reaching almost zero inside the ionosphere and then, increasing again in the transition region (outbound) which reflects the observations better than the simulated density of Run 1. However, the fitted electron density exhibits a peak inside the ionosphere which represents the supra-thermal plasma density.

Figure 4.8 compares the solar wind bulk velocity (v_x , v_y , v_z and $|v_{sw}|$) extracted from the simulation with the observed value obtained by the IMA sensor. As already explained in the previous section the Y- and Z-components are not well determined by IMA due to the spacecraft shadowing and thus, v_y and v_z are difficult to compare with the model. However, v_x of the simulation shows a quite good agreement with the observations regarding the absolute value which has improved especially in the mantle region and ionosphere compared to Run 1. Also the simulated $|v_{sw}|$ improved considerably compared with Run 1, particularly in the regions of the transition zone and ionosphere, where the velocity exhibits a more realistic behavior than the integrated IMA velocity. In the simulation the velocity drops significantly to lower values inside the ionosphere while the measured velocity shows too high values because it is calculated based on the background noise (see section 4.1). In general, the components of the solar wind bulk velocity derived from Run 2 agrees even better with the observations than Run 1 in terms of the absolute values, but the bow shock locations are shifted by a few minutes as already mentioned above.

Figure 4.9 displays the comparison of the magnetic field components (B_x , B_y , B_z and $|B|$) obtained by the simulation Run 2 and measured by the Magnetometer along the spacecraft orbit which provides a considerably better agreement between the model and data than compared to Run 1 (see Figure 4.5), apart from the discrepancy in the bow shock positions. Especially B_x and $|B|$ of the simulation agree almost perfect with the obser-

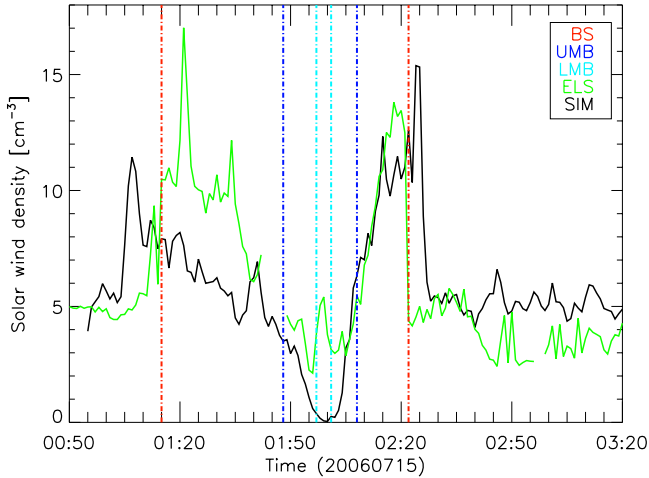


Figure 4.7: Comparison of the solar wind density from the simulation Run 2 (black line) with ELS data (green line; fitted density) along VEX orbit 85 on 15 July 2006, from inbound to outbound. Additionally, the positions of the plasma boundaries (red: bow shock, dark blue: upper mantle boundary, light blue: lower mantle boundary (=ICB)) are marked by dashed vertical lines.

variations, except for the ionospheric region, where the magnetic field intensity decreases down to $\sim 1\text{nT}$ whereas it increases up to $\sim 22\text{nT}$ in the simulation. Hence, the ionosphere seems to be unmagnetized on VEX orbit 85 while it seems to be magnetized in the simulation since no boundary conditions are implied on the electromagnetic fields (explained in subsection 2.2.4). From PVO observations we know, that the ionosphere is magnetized $\sim 95\%$ of the time at solar minimum due to the high ram pressure which exceeds the thermal pressure of the ionosphere, so that the magnetic field can diffuse into the ionosphere. Huddleston et al. (1996) investigated simultaneously acquired magnetic field measurements from PVO and Galileo spacecraft at the time of the Galileo Venus flyby and demonstrated that the solar wind magnetic field convected into the nightside ionosphere on timescales of 10 minutes or more. However, the ionosphere can also be unmagnetized ($\sim 5\%$) at solar minimum during extreme solar conditions, when the ionopause is located at higher altitudes able to withstand the solar wind dynamic pressure which is usually the case at solar maximum (Zhang et al. 2008b). Furthermore, the simulated B_y and B_z also improved slightly in terms of absolute values as well as spatial evolution compared with Run 1 due to the IMF vector being orientated out of the equatorial plane pointing into the south hemisphere instead of lying in the equatorial plane.

Figure 4.10 compares the components of the solar wind electric field (E_x , E_y , E_z and $|E|$) extracted from the simulation with the observed values obtained by the Magnetometer

and ASPERA-4 ($\vec{E} = -\vec{v} \times \vec{B}$). If one compares the total electric field (last panel) with that of the previous section (see Figure 4.6) one finds that the discrepancy in absolute values decreased providing a somewhat better agreement with the observations as a result of the rotated SIM coordinate system in Run 2. However, the uncertainties of the moment calculation as well as the homogeneous cone and clock angles used in the hybrid model have to be taken here into account, as already mentioned in section 4.1. When comparing the positions of the plasma boundaries, they are better reproduced by the simulation Run 1 while the bow shock locations are deferred in Run 2.

To summarize, the simulation results of Run 2 provides a better agreement with the VEX observations obtained on orbit 85 in terms of absolute values due to the rotation of the SIM coordinate system by using a different polar angle. However, the positions of the inbound and outbound bow shock are displaced by a few minutes in Run 2 while they match the data fairly good in Run 1 where the interplanetary magnetic field vector lies in the equatorial plane. Most probably, one would achieve optimal agreements between the model and data in terms of absolute values and plasma boundary locations if the hybrid code would be able to use fluctuating upstream parameters instead of treating them homogeneously.

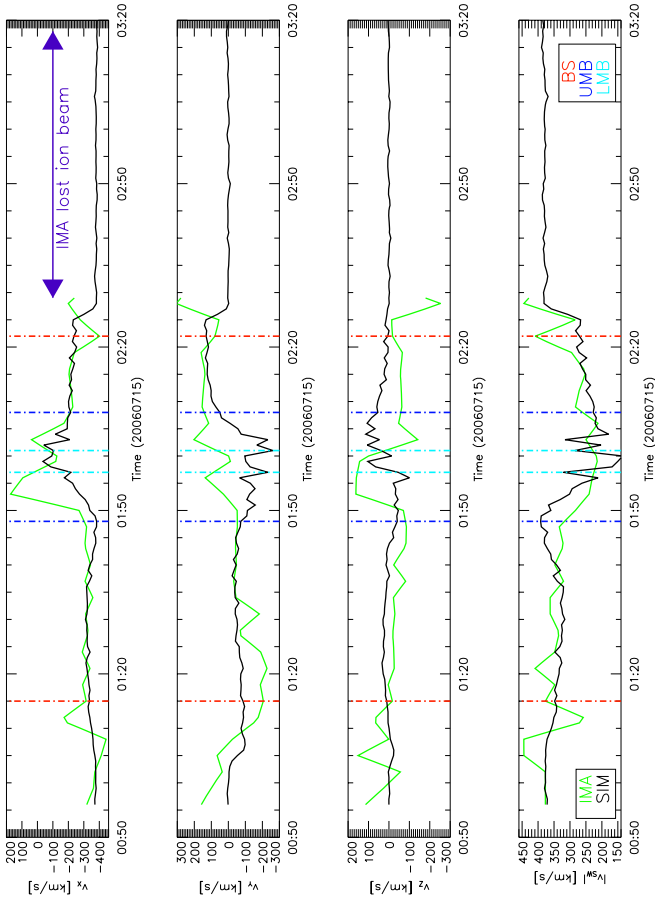


Figure 4.8: Comparison of the solar wind bulk velocity (V_x , V_y , V_z and $|V_{sw}|$) derived from the simulation Run 2 (black line) with IMA data (green line); integrated velocity) along VEX orbit 85 on 15 July 2006, from inbound to outbound. Additionally, the positions of the plasma boundaries (red: bow shock, dark blue: upper mantle boundary, light blue: lower mantle boundary (=ICB)) are marked by dashed vertical lines.

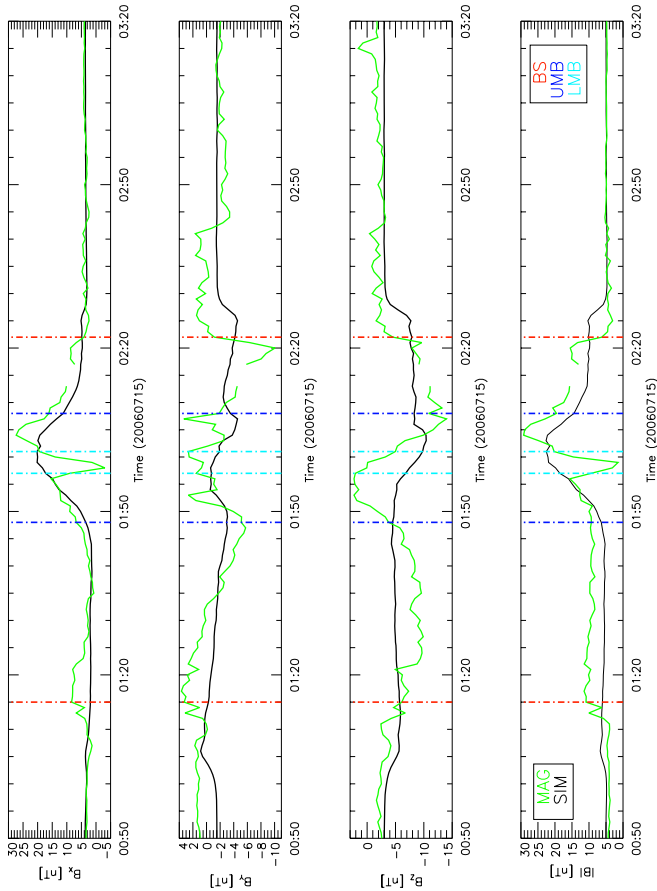


Figure 4.9: Comparison of the magnetic field parameter (B_x , B_y , B_z , and $|B|$) derived from the simulation Run 2 (black line) with the Magnetometer data (green line) along VEX orbit 85 on 15 July 2006, from inbound to outbound. In addition, the positions of the plasma boundaries (red: bow shock, dark blue: upper mantle boundary, light blue: lower mantle boundary (=ICB)) are marked by dashed vertical lines.

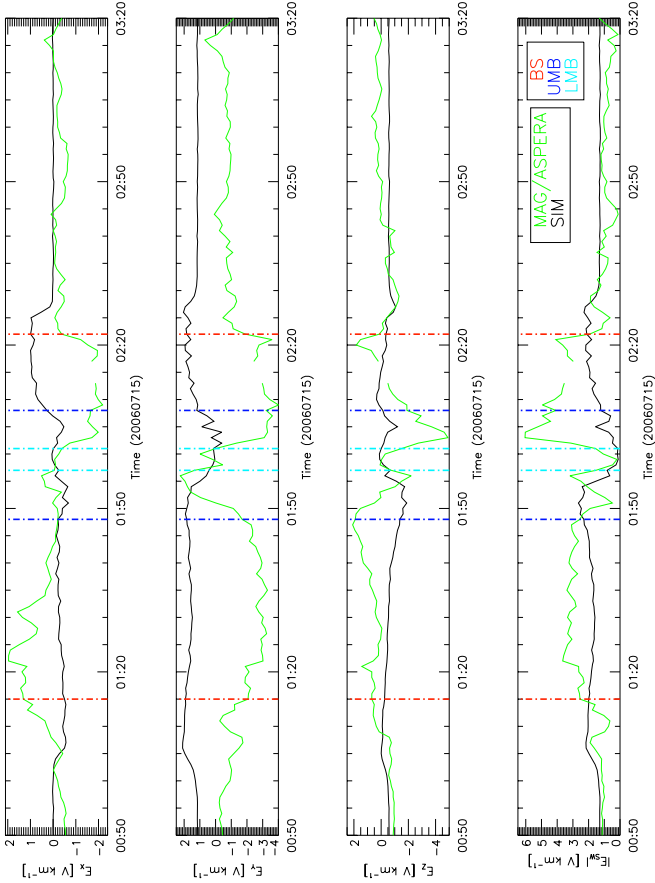


Figure 4.10: Comparison of the electric field parameter ($\vec{E} = -\vec{v} \times \vec{B}$; E_x , E_y , E_z and $|E|$) derived from the simulation Run2 (black line) with the Magnetometer-ASPERA data (green line) along VEX orbit 85 on 15 July 2006, from inbound to outbound. Additionally, the positions of the plasma boundaries (red: bow shock, dark blue: upper mantle boundary, light blue: lower mantle boundary (=ICB)) are marked by dashed vertical lines.

4.3 Critical review of the accuracy of the observational parameters

The accuracy of the magnetic field data is about 1 nT (Zhang et al. 2008a). The minimum field value we observe on Orbit 85 is 5 nT and thus, the maximal error in the field determination is 20 % corresponding to an angular error of about 11° . We regard the influence of the magnetic field error as a minor effect.

For the plasma densities we have used the densities derived from the ELS sensor which are strongly influenced by the spacecraft potential. The values observed in the solar wind have been cross-calibrated with observations by the ACE spacecraft which show an agreement within 30 %, which also is of the same magnitude as the variations in the different moment determination methods. For the densities observed in the magnetosheath we must assume that the spacecraft potential is the same as observed in the solar wind, in which case the error is of the same size like it is in the solar wind region. The ion densities observed below the magnetic barrier are less well defined, since they are influenced by the spacecraft potential, by the obstruction of the field of view of the sensor by the spacecraft body and the spacecraft ram velocity relative to the surrounding plasma velocity. We must assume that the error in the ionospheric ion density determination can be one order of magnitude.

The absolute velocity of protons in the solar wind is determined by the precision of the energy resolution of the IMA sensor which is 6 % corresponding to velocity resolution of 24 %. The main problem for the absolute velocity determination is the low energy limit of the proton observations which depends on the post-acceleration level of the sensor. The absolute velocity in the magnetosheath is less well defined because the heated proton distribution is only partially observed, on the one hand by the obstruction by the spacecraft body and on the other hand by the limited mass resolution of the IMA sensor. This error depends on the mean energy and temperature of the distribution. For the Orbit 85 we can assume that the error is less than 50 %. The velocity vector orientation error is determined by the angular resolution of the IMA sensor and the obstruction of the field of view. When the plasma flow is in the field of view of the plasma sensor the angular resolution is $11 \times 20^\circ$.

The velocity determination of the heavy ions in the ionosphere depends on the spacecraft potential, the obstruction by the spacecraft body and the spacecraft ram velocity. For Orbit 85 the error in the determination is higher than the difference between the observed velocity and the negative spacecraft ram velocity.

4.4 Atmospheric escape rates for oxygen

The thermal and non-thermal loss processes of oxygen and hydrogen have been discussed in subsection 1.1.7 pointing out that the non-thermal escape mechanism dominate at Venus. The main non-thermal loss processes of oxygen, namely the ion pickup, plasma clouds and momentum transport, are self-consistently included in the hybrid model. Thus, one can also compare the escape rates resulting from the simulation with measurements and estimations based on other models.

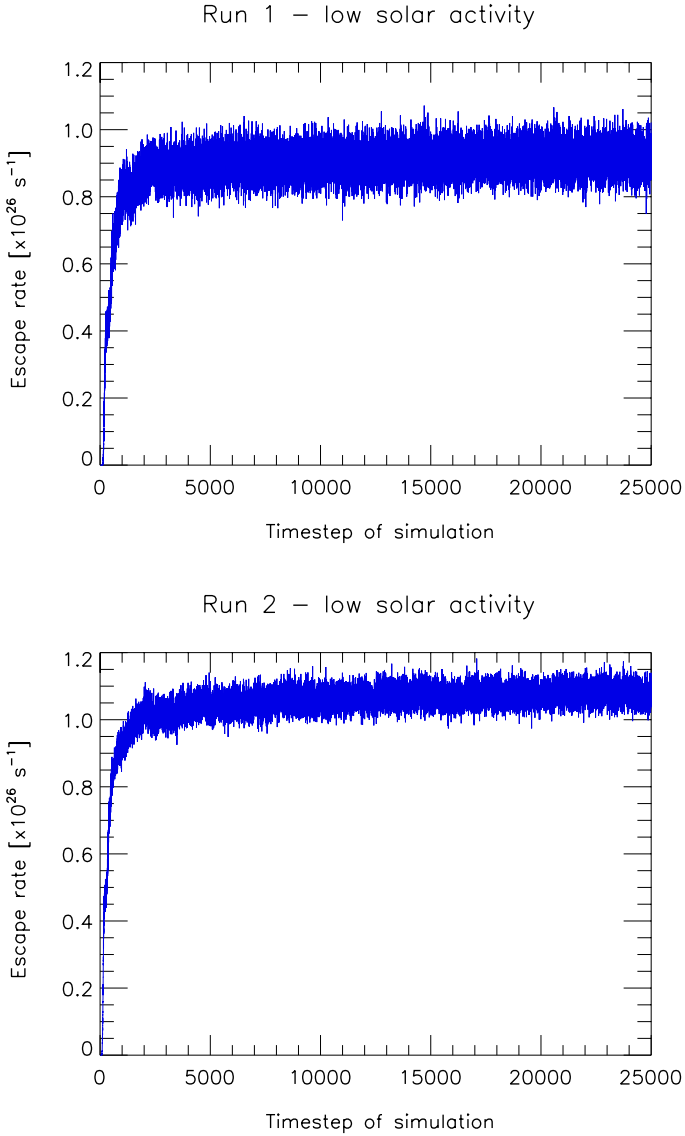


Figure 4.11: Atmospheric escape fluxes at solar minimum as a function of the timestep of simulation obtained by Run 1 and Run 2 based on VEX input parameters.

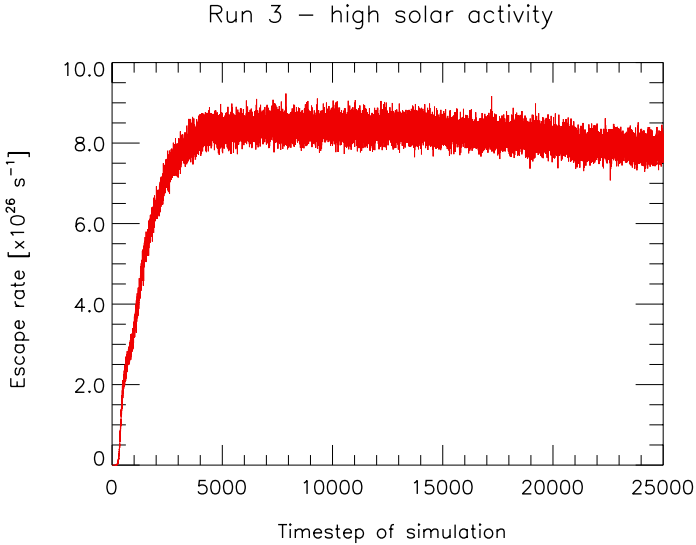


Figure 4.12: Atmospheric escape fluxes at solar maximum as a function of the timestep of simulation obtained by Run 3 based on PVO input parameters.

Lammer et al. (2006) provide a theoretical total oxygen escape to space from Venus for averaged solar activity of about $3.0 \times 10^{25} \text{ s}^{-1}$ based on Monte Carlo particle simulations and gas dynamic test particle models. This value includes the estimated mean loss rates from pickup ions ($\sim 1.6 \times 10^{25} \text{ s}^{-1}$), sputtered atoms ($\sim 6.0 \times 10^{24} \text{ s}^{-1}$) and detached plasma clouds ($\sim 0.5\text{-}1.0 \times 10^{25} \text{ s}^{-1}$).

However, the estimated loss rates by plasma clouds should be treated with great care because they are based on several assumptions with respect to the sizes, shapes and distributions of the plasma clouds which cannot be well-determined by single-spacecraft observations. Brace et al. (1982) investigated early Electron Temperature Probe (OETP) measurements onboard PVO during high solar activity in order to study the escape fluxes caused by plasma clouds. They estimated a total ion (O^+ and H^+) escape rate of about $\sim 7.0 \times 10^{26} \text{ s}^{-1}$ as an upper limit based on the plasma clouds' measured transit times, their probability of occurrence, their statistical distribution and their average electron density. Assuming that the stoichiometric ratio $Q(\text{H}^+)/Q(\text{O}^+)$ is 2:1 (Barabash et al. 2007b), which means two hydrogen atoms would leave one oxygen atom in the atmosphere, would result in a total oxygen loss rate of $\sim 2.3 \times 10^{26} \text{ s}^{-1}$ obtained by the study of Brace et al. (1982). Terada et al. (2002) concluded from their global 2D hybrid simulations that Venus loses oxygen ions in the order of 10^{25} ions/s due to plasma clouds which are triggered by the Kelvin-Helmholtz instability.

Recently, Barabash et al. (2007a) gave an initial estimation of the oxygen escape rate at Venus based on the ASPERA-4 measurements and concluded that the lower limit is about 10^{25}s^{-1} . They demonstrated that the dominant escaping ions are O^+ , He^+ and H^+ which leave Venus through the plasma sheet and in a boundary layer of the induced magnetosphere. It is quite difficult to determine an absolute value for the escape rate because there are several instrumental restrictions. One of the main problems is the saturation of the IMA sensor because too high ion fluxes are detected and thus, a special technique has to be applied in order to reconstruct the original flux. Another problem is that the field of view of IMA is very restricted due to the spacecraft shadow as already explained in subsection 4.1. Additionally, the VEX moves relatively fast compared to the heavy ion velocity and therefore, one has also to use a relative correction for the ram velocity of the spacecraft. Moreover, one should only consider orbits which show quite stable solar wind conditions in order to calculate a reliable direction of the convective electric field provided by ASPERA-4 and MAG data. In the study of Barabash et al. (2007a) only 131 orbits were selected out of around 700. In order to provide trustable estimations one needs better statistics at different solar conditions.

The simulation Run 1 and Run 2 (orbit No. 85) for solar minimum conditions yield an oxygen escape rate of about $0.9 \times 10^{26}\text{s}^{-1}$ and $1.1 \times 10^{26}\text{s}^{-1}$ (see Figure 4.11), respectively, which establish only lower limits because the dayside ionospheric densities produced in the simulation ($\sim 10^2\text{cm}^{-3}$) are about a factor of 100 less than the observed values ($\sim 10^4\text{cm}^{-3}$). In the simulated ionosphere the radial density gradient is extremely high and the spatial resolution of the simulation grid yields always mean values over 100 km in radial distance reducing the maximum values of the heavy ion density observed in the simulation.

Figure 4.12 shows an atmospheric escape rate of about $8.0 \times 10^{26}\text{s}^{-1}$ derived from the simulation Run 3 based on PVO input parameters, and provides of course also just a lower value for high solar activity. The oxygen escape fluxes obtained by the simulation runs for solar minimum and maximum provide a mean value of $\sim 4.5 \times 10^{26}\text{s}^{-1}$ for averaged solar conditions which is about 15 times larger than the theoretical estimation from Lammer et al. (2006) but one has to consider the insecure estimations from the detached plasma clouds as mentioned above.

However in summary, the 3D hybrid model yields an escape rate estimation within the limits of observations and theoretical calculations, and thus, is able to provide an insight into the loss processes of oxygen at Venus induced by the solar wind. It should be noted that our atmospheric model is an approximation to the real system since only the solar EUV radiation is considered as a source for the dayside ion production while electron impact and charge exchange are neglected. These latter two ionization processes can be neglected for the dayside ionosphere because photoionization is the dominant mechanism Bauske et al. (1998) while they play an important role for the nightside ionosphere since photoionization does not occur behind the obstacle. As explained in subsection 2.2.6, the ion production on the nightside has been approximated in a quite simple way: for the solar zenith angles $> \pm 87^\circ$ and the nightside of the obstacle, the ion production is assumed to be independent of the solar zenith angle setting it to an altitude dependent value only. This yields about 10 % of the dayside ion production rate which is only a rough approximation to the ionization processes taking place at the nightside. However, this production rate is an adequate representation for the weak ionosphere on the nightside.

5 Summary and conclusions

In the framework of this thesis the global plasma environment of Venus was investigated by using a three-dimensional electromagnetic hybrid model, treating the electrons as a massless, charge-neutralizing fluid, whereas a completely kinetic approach is used to cover ion dynamics. The use of a hybrid model rather than a MHD model seems to be mandatory since the mean gyroradii of the solar wind protons are comparable with the characteristic length scales of the subsolar region and the mean gyroradii of the pickup ions are comparable with the characteristic length scales of the planet's radius. The Venusian atmosphere is modeled under the assumption of an effective ionization rate mainly caused by solar EUV radiation. The production rate is a function of the altitude above the surface and of the solar zenith angle on the dayside, but depends only on the altitude on the nightside. Two different electron populations are incorporated in the hybrid code, in order to take into account the significantly different temperatures of the solar wind and ionospheric electrons. Using a curvilinear grid in the vicinity of the planet allows a high resolution of the plasma structures near the planetary surface.

The common features of the solar wind - atmosphere interaction of an unmagnetized planet are fairly well reproduced by the hybrid code. The simulated bow shock, exhibiting shocklet structuring (kinetic nature), is formed in front of the planet and is equal in shape, size and position with the observed bow shock. Behind the obstacle a plasma wake is formed, filled with planetary ions and split into a central tail (plasma sheet) with high density and several rays with smaller density. Due to the lack of an intrinsic magnetic field the interplanetary magnetic field (IMF) lines are draping around the planet, generating a magnetic barrier on the dayside as well as an induced magnetotail, consisting of two lobes of opposite polarity separated by a plasma sheet, on the nightside. The most pronounced characteristics are asymmetries with respect to the convection electric field affecting the heavy ion pickup region, magnetic field intensity and the shock geometry. The very same global structures are found by Bößwetter et al. (2004) studying the Martian plasma interaction and by Simon et al. (2006b) investigating Titan's plasma environment outside of Saturn's magnetosphere applying modified versions of the present 3D hybrid model. A first determination of the tail boundaries (mantle region) indicates a very broad transition zone from solar wind to planetary ions, which also is confirmed by the simulation results.

Additionally, the shapes and average positions of the plasma boundaries at Venus at solar minimum based on the ASPERA-4 observations were determined and discussed in section 3.1. It was concluded, that the bow shock location is quite stable whereas the upper and lower boundary of the transition zone exhibit a highly variable behavior on the nightside. The variations occurring in the bow shock positions can be ascribed to the fluctuations of the magnetic field strength due to its dependency on the upstream Mach number though this was not analyzed here. Furthermore, the terminator bow shock loca-

tion was found to be independent of the dynamic pressure of the solar wind, at least at low solar activity, which is in agreement with previous studies based on PVO observations. In addition, it was demonstrated that the terminator shock position does not show yet a dependency on the solar EUV flux because the EUV radiation shows only small variations over the period of observations as expected at low solar activity.

Emphasis has been placed on the comparison of the plasma and magnetic field observations made onboard the Venus Express spacecraft with the results of the hybrid simulation. This comparison between measurements and simulations indicates that the hybrid approach is capable of providing an adequate picture of the global plasma processes at Venus.

To summarize, by means of the VEX orbit No.85 two simulation runs were carried out with different orientations of the IMF vector and then, were compared with the Magnetometer and ASPERA-4 measurements. In the first run, IMF lies in the equatorial plane ($\theta=90^\circ$) whereas it is orientated out of the equatorial plane pointing into the south hemisphere of Venus ($\theta=127.5^\circ$) in the second run. The hybrid model demonstrated that the orientation of the magnetic field plays an important role for the pickup and escape processes at Venus since it determines the direction of the solar wind electric field. For the specific orbit presented in this study, it turned out that the second run matches the observations fairly good in terms of absolute values. However, the bow shock locations are shifted by a few minutes compared to the crossings observed by the plasma and magnetic field instruments while the other boundaries are well-reproduced. The positions of the simulated plasma boundaries are in good agreement with the observations in the first run but show significant discrepancies between the observed compression of the plasma and the magnetic field on the dusk side (in the sense of orbital motion) of the orbit.

Possible reasons for the disagreements between the model and data are on the one hand, the calculated input parameters because there are still uncertainties in the estimation of the plasma moments. The main difficulties are caused by the saturation of the detectors when too high ion fluxes are recorded and by IMA being shadowed by the VEX spacecraft. Parts of the field of view of IMA are blocked by the spacecraft body implying that the quality of the data depends very much on the spacecraft attitudes, which is especially important for statistical studies, moment calculation and escape flux estimations. On the other hand, the atmospheric model has also to be refined. A multi-species ionosphere and exosphere as well as a further enhancement of the grid cell resolution near the Venusan surface would provide most probably more realistic planetary densities and thus, would lead to more reliable atmospheric escape rates. Another reason for the disagreements between simulations and measurements can be ascribed to fluctuations in the upstream solar wind parameters which are assumed to be completely homogeneous in the simulation. For instance, in the hybrid model the magnetic field is assumed to be free of any fluctuations, while it is strongly fluctuating in the real system. The quasi-parallel side of the shock is a complex structure where ions propagate in the upstream direction along the magnetic field lines reaching large distances from the shock front. These ions affect the incoming solar wind flow through a number of plasma instabilities and wave generation mechanisms, giving rise to a structured foreshock region. At a quasi-parallel shock $\vec{v} \times \vec{B}$ is small, such that fluctuations of the magnetic field cause forces within the plasma which are stronger than the $\vec{v} \times \vec{B}$ force and can lead to the excitation of waves. However, this turbulent and complex quasi-parallel shock scenario is oversimplified in the simula-

tions because the simulation uses a constant IMF angle. Consequently, the incongruities between the model and data are higher on the quasi-parallel side of the bow shock, as it is the case on the inbound pass of Orbit 85.

Comparable studies were done by Kallio et al. (2006) and Jarvinen et al. (2008) for instance. Kallio et al. (2006) investigated the global plasma environment of Venus for solar minimum conditions (based on PVO measurements) with a quasi-neutral hybrid (QNH) model which is similar to the hybrid approach presented in this work. The QNH model is also able to reproduce the basic observed plasma and magnetic field regions and boundaries near Venus. However, their grid resolution is not fine enough to model the position and shape of the bow shock, multiple-shocklets, the inner structure of the magnetic barrier, tail rays and filaments. Nevertheless, they also find a north-south asymmetry in the direction of the convective electric field due to mass loading of the solar wind by heavy ions as stated in subsection 3.2.1 explaining the simulation results carried out for low and high solar activity. Additionally, they also observe a dawn-dusk asymmetry and conclude that this asymmetry is associated with the IMF x-component because they use a Parker spiral IMF where the IMF x-component is larger in magnitude than the magnetic field components perpendicular to the flow. They also yield an asymmetry in the magnetic field strength along the solar wind electric field because of the mass loading effect but it is less pronounced than in the simulation results presented in this study. As in this case study, Kallio et al. (2006) also use homogeneous upstream solar wind parameters. But since Venus shows a strong dependence on the phase of the solar cycle it is necessary to study the solar wind-ionosphere interaction with varying plasma and magnetic field parameters in order to carry out more realistic investigations. In addition, they obtain a total escape rate of oxygen ions from the simulation box of about $2.2 \times 10^{24} \text{s}^{-1}$. This value lies beyond the recently estimated lower limit based on ASPERA-4 observations (Barabash et al. 2007a) and is much lower compared to the simulated escape rate obtained by this hybrid model. The reason is the coarse grid resolution used in the QNH approach which inhibits the evolution of a self-consistent ionosphere.

Jarvinen et al. (2008) presented a direct comparison between the magnetic field measurements derived from OMAG onboard PVO with a hybrid simulation code which is the same model as used by Kallio et al. (2006) discussed above. They studied the statistics of the solar wind and IMF conditions at Venus based on the large long-term dataset of PVO and then, used these results as input parameters for their simulations. The results of this comparison between the simulation and observations along the PVO spacecraft trajectory demonstrated that their hybrid model is able to reproduce the global structures and basic trends seen in the data. However, the spatial resolution of the grid is not fine enough in the vicinity of the ionospheric obstacle (as already mentioned above) and thus, showing discrepancies between the model and data since non-realistic features are generated in the simulation cells just above the obstacle. They concluded that the hybrid code would need to be parallelized first and run on a supercomputer in order to carry out simulations in a feasible total running time with a finer constant sized grid because the computing expense related to the number of particles in the simulation box is inversely proportional to the cell volume.

To conclude, the hybrid code presented in this work is able to reproduce more features of the solar wind- atmosphere interaction at Venus than other current hybrid models, such as Kallio et al. (2006) and Jarvinen et al. (2008) and thus, gives a more comprehensive

picture of the Venusian global plasma environment. The two main important advantages of our model are associated with the spatial resolution and the provision for the different electron pressure terms.

The simulations are performed on a curvilinear grid obtaining a considerably improved spatial resolution of about 100-150 km/cell in the vicinity of the obstacle and about 250-300 km/cell beyond the distorted grid. Therefore, our model is capable to reproduce not only the basic structures of the solar wind interaction regions but also the position and shape of the bow shock, the multiple-shocklet structuring and the tail rays on the nightside ionosphere. These features are not generated by the hybrid model of Kallio et al. (2006) since they use a coarse equidistant grid providing a spatial resolution of 605 km everywhere in the simulation box which also makes it impossible to include a self-consistent ionosphere.

The consideration of the different electron temperatures in the solar wind and ionosphere by using two different electron pressure terms is the other advantage of our hybrid code. These electron pressure forces in combination with the convective electric field play a decisive part in the formation of the ICB. As demonstrated in subsection 3.2.1.1, the ICB develops in the hemisphere where both forces are antiparallel leading to a sharply pronounced boundary layer which inhibits the mixing of the plasmas (protons and heavy ions). On the opposite hemisphere no ICB emerges due to the parallelism of the motional electric field and the electron pressure forces. For instance, in the hybrid approach of Kallio et al. (2006), the electrons are assumed to be cold and therefore, their model is not able to generate the ICB.

The current VEX mission provides new in-situ measurements with sophisticated instruments and fills in the gaps left by the PVO mission, especially at the time of low solar activity. The thesis has attempted to answer open questions on the global plasma environment on Venus as well as the dynamics and processes involved in the solar wind-atmosphere interaction by means of a hybrid model and observations made by the ASPERA - 4 and MAG experiments. The results presented in this thesis are in good agreement with previous studies based on PVO observations regarding the physics of the plasma boundaries and the atmospheric escape processes at Venus. However, the comparison between the model and data also pointed out that further investigations based on good statistics and improved models are needed in order to answer the questions which have not been resolved yet. Thus, the final section provides an overview of possible improvements with respect to the hybrid model.

Outlook

One of the technical limitations is associated with the spatial resolution. Although we use a curvilinear grid to enhance the spatial resolution near the planetary surface, it is not high enough to resolve the ionopause since the ionosphere is just a few bins in size. The hybrid code used in the thesis is currently in the process of being parallelized. By means of this MPI (message-passing interface) parallelization one can improve the spatial grid resolution in order to resolve small scale structures of the solar wind interaction region, such as for example the ionopause. Moreover, the computing time can be significantly reduced so that a quasi-stationary state is reached within a week while it takes almost 3 months for the current hybrid code in the case of low solar activity and roughly 6 months in the case of high solar activity. Consequently, one could perform many more simulations by varying the input parameters obtained by observations in order to evaluate and improve the accuracy of the hybrid code. Then, this model can be used to estimate the plasma boundary locations and escape fluxes from the planet under different conditions from today. Additionally, the number of macroparticles used in the simulation can be increased with a multi-processor computer. Under these conditions, it would be possible to incorporate chemical reactions in the lower atmosphere instead of removing the particles artificially when hitting the inner boundary of the simulation box and thus, improving the ionospheric densities produced in the simulation. Furthermore, one should consider a self-consistent implementation of additional ionization processes such as the electron impact ionization and charge exchange as already realized by Modolo et al. (2006) for investigating the solar wind plasma interaction with the Martian exosphere. These two ion sources are quite important for the ionospheric nightside of Venus, especially at low solar activity, since the horizontal plasma transport from the dayside due to pressure gradients is significantly reduced at these times.

Bibliography

- Bagdonat, T., 2005, Hybrid Simulation of Weak Comets, Ph.D. thesis, Technische Universität Braunschweig
- Bagdonat, T., Motschmann, U., 2002a, 3D Hybrid Simulation Code Using Curvilinear Coordinates, *Journal of Computational Physics*, 183, 470–485
- Bagdonat, T., Motschmann, U., 2002b, From a Weak to a Strong Comet - 3d Global Hybrid Simulation Studies, *Earth Moon and Planets*, 90, 305–321
- Barabash, S., Fedorov, A., Sauvaud, J. J., Lundin, R., Russell, C. T., Futaana, Y., Zhang, T. L., Andersson, H., Brinkfeldt, K., Grigoriev, A., Holmström, M., Yamauchi, M., Asamura, K., Baumjohann, W., Lammer, H., Coates, A. J., Kataria, D. O., Linder, D. R., Curtis, C. C., Hsieh, K. C., Sandel, B. R., Grande, M., Gunell, H., Koskinen, H. E. J., Kallio, E., Riihelä, P., Säles, T., Schmidt, W., Kozyra, J., Krupp, N., Fränz, M., Woch, J., Luhmann, J., McKenna-Lawlor, S., Mazelle, C., Thocaven, J.-J., Orsini, S., Cerulli-Irelli, R., Mura, M., Milillo, M., Maggi, M., Roelof, E., Brandt, P., Szego, K., Winningham, J. D., Frahm, R. A., Scherrer, J., Sharber, J. R., Wurz, P., Bochsler, P., 2007a, The loss of ions from Venus through the plasma wake, *Nature*, 450, 650–653
- Barabash, S., Sauvaud, J.-A., Gunell, H., Andersson, H., Grigoriev, A., Brinkfeldt, K., Holmström, M., Lundin, R., Yamauchi, M., Asamura, K., Baumjohann, W., Zhang, T. L., Coates, A. J., Linder, D. R., Kataria, D. O., Curtis, C. C., Hsieh, K. C., Sandel, B. R., Fedorov, A., Mazelle, C., Thocaven, J.-J., Grande, M., Koskinen, H. E. J., Kallio, E., Säles, T., Riihela, P., Kozyra, J., Krupp, N., Woch, J., Luhmann, J., McKenna-Lawlor, S., Orsini, S., Cerulli-Irelli, R., Mura, M., Milillo, M., Maggi, M., Roelof, E., Brandt, P., Russell, C. T., Szego, K., Winningham, J. D., Frahm, R. A., Scherrer, J., Sharber, J. R., Wurz, P., Bochsler, P., 2007b, The Analyser of Space Plasmas and Energetic Atoms (ASPERA-4) for the Venus Express mission, *Planet. Space Sci.*, 55, 1772–1792
- Bauer, S. J., 2001, *Die Planetenatmosphären, Lehrbuch der Experimentalphysik: Erde und Planeten*, de Gruyter, ISBN 3-11-016837-5
- Baumjohann, W., Treumann, R. A., 1996, *Basic space plasma physics*, London: Imperial College Press, [c1996
- Bauske, R., Nagy, A. F., Gombosi, T. I., De Zeeuw, D. L., Powell, K. G., Luhmann, J. G., 1998, A three-dimensional MHD study of solar wind mass loading processes at Venus: Effects of photoionization, electron impact ionization, and charge exchange, *J. Geophys. Res.*, 103, 23 625–23 638

- Birdshall, C. K., Langdon, A. B., 1985, *Plasma Physics via Computer Simulations*, McGraw-Hill Book Company, New York
- Bößwetter, A., Bagdonat, T., Motschmann, U., Sauer, K., 2004, Plasma boundaries at Mars: a 3-D simulation study, *Annales Geophysicae*, 22, 4363–4379
- Bößwetter, A., Simon, S., Bagdonat, T., Motschmann, U., Fränz, M., Roussos, E., Krupp, N., Woch, J., Schüle, J., Barabash, S., Lundin, R., 2007, Comparison of plasma data from ASPERA-3/Mars-Express with a 3-D hybrid simulation, *Annales Geophysicae*, 25, 1851–1864
- Brace, L. H., Kliore, A. J., 1991, The structure of the Venus ionosphere, *Space Sci. Rev.*, 55, 81–163
- Brace, L. H., Theis, R. F., Hoegy, W. R., 1982, Plasma clouds above the ionopause of Venus and their implications, *Planet. Space Sci.*, 30, 29–37
- Brecht, S. H., Ferrante, J. R., 1991, Global hybrid simulation of unmagnetized planets - Comparison of Venus and Mars, *J. Geophys. Res.*, 96, 11 209–+
- de Pater, I., Lissauer, J. J., 2001, *Planetary Sciences*, Cambridge University Press, Cambridge, ISBN 0 521 48219 4
- Dubinin, E., Modolo, R., Fraenz, M., Woch, J., Duru, F., Akalin, F., Gurnett, D., Lundin, R., Barabash, S., Plaut, J. J., Picardi, G., 2008, Structure and dynamics of the solar wind/ionosphere interface on Mars: MEX-ASPERA-3 and MEX-MARSIS observations, *Geophys. Res. Lett.*, 35, 11 103–+
- Fränz, M., Dubinin, E., Roussos, E., Woch, J., Winningham, J. D., Frahm, R., Coates, A. J., Fedorov, A., Barabash, S., Lundin, R., 2007, Plasma moments in the environment of Mars: Mars Express ASPERA-3 observations, *Space Sci. Rev.*, pp. 10.1007/s11 214–006–9115–9
- Hedin, A. E., Niemann, H. B., Kasprzak, W. T., Seiff, A., 1983, Global empirical model of the Venus thermosphere, *J. Geophys. Res.*, 88, 73–83
- Huddleston, D. E., Russell, C. T., Kivelson, M. G., Luhmann, J. G., 1996, Time delays in the solar wind flow past Venus: Galileo-Pioneer Venus correlations, *J. Geophys. Res.*, 101, 4539–4546
- Israelevich, P. L., Gombosi, T. I., Ershkovich, A. I., DeZeeuw, D. L., Neubauer, F. M., Powell, K. G., 1999, The induced magnetosphere of comet Halley, 4, Comparison of in situ observations and numerical simulations, *J. Geophys. Res.*, 104, 28 309–+
- Jarvinen, R., Kallio, E., Sillanpää, I., Janhunen, P., 2008, Hybrid modelling the Pioneer Venus Orbiter magnetic field observations, *Advances in Space Research*, 41, 1361–1374
- Kallio, E., Luhmann, J. G., Lyon, J. G., 1998, Magnetic field near Venus - A comparison between Pioneer Venus Orbiter magnetic field observations and an MHD simulation, *J. Geophys. Res.*, 103, 4723–+

- Kallio, E., Jarvinen, R., Janhunen, P., 2006, Venus solar wind interaction: Asymmetries and the escape of O⁺ ions, *Planet. Space Sci.*, 54, 1472–1481
- Kivelson, M. G., Russell, C. T., 1995, *Introduction to space physics*, Cambridge University Press, Cambridge
- Knudsen, W. C., 1992, *The Venus ionosphere from in situ measurements*, Washington DC American Geophysical Union Geophysical Monograph Series, 66, 237–263
- Kulikov, Y. N., Lammer, H., Lichtenegger, H. I. M., Terada, N., Ribas, I., Kolb, C., Langmayr, D., Lundin, R., Guinan, E. F., Barabash, S., Biernat, H. K., 2006, Atmospheric and water loss from early Venus, *Planet. Space Sci.*, 54, 1425–1444
- Lammer, H., Lichtenegger, H. I. M., Biernat, H. K., Erkaev, N. V., Arshukova, I. L., Kolb, C., Gunell, H., Lukyanov, A., Holmstrom, M., Barabash, S., Zhang, T. L., Baumjohann, W., 2006, Loss of hydrogen and oxygen from the upper atmosphere of Venus, *Planet. Space Sci.*, 54, 1445–1456
- Leftwich, T. E., von Frese, R. R. B., Kim, H. R., Noltimier, H. C., Potts, L. V., Roman, D. R., Tan, L., 1999, Crustal analysis of Venus from Magellan satellite observations at Atalanta Planitia, Beta Regio, and Thetis Regio, *J. Geophys. Res.*, 104, 8441–8462
- Luhmann, J. G., Cravens, T. E., 1991, Magnetic fields in the ionosphere of Venus, *Space Sci. Rev.*, 55, 201–274
- Luhmann, J. G., Russell, C. T., 1997, Venus: Magnetic field and magnetosphere, in *Encyclopedia of Planetary Sciences*, (Eds.) J. H. Shirley, R. W. Fainbridge, pp. 905–907, Chapman and Hall, New York
- Luhmann, J. G., Tatrallyay, M., Pepin, R. O., 1992, Venus and Mars: Atmospheres, ionospheres, and solar wind interactions; *Proceedings of the Chapman Conference, Balatonfured, Hungary, June 4-8, 1990*, Washington DC American Geophysical Union Geophysical Monograph Series, 66
- Markiewicz, W. J., Titov, D. V., Limaye, S. S., Keller, H. U., Ignatiev, N., Jaumann, R., Thomas, N., Michalik, H., Moissl, R., Russo, P., 2007, Morphology and dynamics of the upper cloud layer of Venus, *Nature*, 450, 633–636
- Marov, M. Y., Grinspoon, D. H. (Eds.), 1998, *The planet Venus*
- Miller, K. L., Knudsen, C. W., Spenser, K., Whitten, R. C., Novak, V., 1980, Solar zenith angle dependence of ionospheric ion and electron temperatures and density on Venus, *J. Geophys. Res.*, 85, 7759–7764
- Modolo, R., Chanteur, G. M., Dubinin, E., Matthews, A. P., 2006, Simulated solar wind plasma interaction with the Martian exosphere: influence of the solar EUV flux on the bow shock and the magnetic pile-up boundary, *Annales Geophysicae*, 24, 3403–3410
- Moore, K. R., Thomas, V. A., McComas, D. J., 1991, Global hybrid simulation of the solar wind interaction with the dayside of Venus, *J. Geophys. Res.*, 96, 7779–7791

- Murawski, K., Steinolfson, R. S., 1996a, Numerical modeling of the solar wind interaction with Venus, *Planet. Space Sci.*, 44, 243–252
- Murawski, K., Steinolfson, R. S., 1996b, Numerical simulations of mass loading in the solar wind interaction with Venus, *J. Geophys. Res.*, 101, 2547–2560
- Nagy, A. F., Kim, J., Cravens, T. E., 1990, Hot hydrogen and oxygen atoms in the upper atmospheres of Venus and Mars, *Annales Geophysicae*, 8, 251–256
- Nimmo, F., 2002, Why does Venus lack a magnetic field?, *Geology*, 30, 987–990
- Omidi, N., Winske, D., 1990, Steepening of kinetic magnetosonic waves into shocklets - Simulations and consequences for planetary shocks and comets, *J. Geophys. Res.*, 95, 2281–2300
- Phillips, J. L., McComas, D. J., 1991, The magnetosheath and magnetotail of Venus, *Space Sci. Rev.*, 55, 1–80
- Roussos, E., Müller, J., Simon, S., Bößwetter, A., Motschmann, U., Krupp, N., Fränz, M., Woch, J., Khurana, K. K., Dougherty, M. K., 2008, Plasma and fields in the wake of Rhea: 3D hybrid simulation and comparison with Cassini data, *Annales Geophysicae*, 26, 619–637
- Russell, C. T., 2000, The solar wind interaction with earth's magnetosphere: A tutorial. <<http://www-ssc.igpp.ucla.edu/ssc/tutorial/>>
- Russell, C. T., Chou, E., Luhmann, J. G., Gazis, P., Brace, L. H., Hoegy, W. R., 1988, Solar and interplanetary control of the location of the Venus bow shock, *J. Geophys. Res.*, 93, 5461–5469
- Russell, C. T., Luhmann, J. G., Strangeway, R. J., 2006, The solar wind interaction with Venus through the eyes of the Pioneer Venus Orbiter, *Planet. Space Sci.*, 54, 1482–1495
- Schunk, R. W., Nagy, A. F., 2004, Ionospheres, *Ionosphere*
- Shimazu, H., 2001, Three-dimensional hybrid simulation of solar wind interaction with unmagnetized planets, *J. Geophys. Res.*, 106, 8333–8342
- Simon, S., Bagdonat, T., Motschmann, U., Glassmeier, K.-H., 2006a, Plasma environment of magnetized asteroids: A 3D hybrid simulation study, *Annales Geophysicae*, 24, 407–414
- Simon, S., Bößwetter, A., Bagdonat, T., Motschmann, U., Glassmeier, K.-H., 2006b, Plasma environment of Titan: a 3-D hybrid simulation study, *Annales Geophysicae*, 24, 1113–1135
- Simon, S., Boesswetter, A., Bagdonat, T., Motschmann, U., 2007, Physics of the Ion Composition Boundary: a comparative 3-D hybrid simulation study of Mars and Titan, *Annales Geophysicae*, 25, 99–115

- Slavin, J. A., Holzer, R. E., 1981, Solar wind flow about the terrestrial planets. I - Modeling bow shock position and shape, *J. Geophys. Res.*, 86, 11 401–11 418
- Slavin, J. A., Elphic, R. C., Russell, C. T., Scarf, F. L., Wolfe, J. H., Mihalov, J. D., Intriligator, D. S., Brace, L. H., Taylor, H. A., Daniell, R. E., 1980, The solar wind interaction with Venus - Pioneer Venus observations of bow shock location and structure, *J. Geophys. Res.*, 85, 7625–7641
- Slavin, J. A., Holzer, R. E., Spreiter, J. R., Stahara, S. S., 1984, Planetary Mach cones - Theory and observation, *J. Geophys. Res.*, 89, 2708–2714
- Spenner, K., Knudsen, W. C., Miller, K. L., Novak, V., Russell, C. T., Elphic, R. C., 1980, Observation of the Venus mantle, the boundary region between solar wind and ionosphere, *J. Geophys. Res.*, 85, 7655–7662
- Spreiter, J. R., Stahara, S. S., 1992, Computer modeling of solar wind interaction with Venus and Mars, Washington DC American Geophysical Union Geophysical Monograph Series, 66, 345–383
- Stevenson, D. J., 2003, Planetary magnetic fields, *Earth and Planetary Science Letters*, 208, 1–11
- Svedhem, H., Titov, D. V., McCoy, D., Lebreton, J.-P., Barabash, S., Bertaux, J.-L., Drossart, P., Formisano, V., Häusler, B., Korabely, O., Markiewicz, W. J., Nevejans, D., Pätzold, M., Piccioni, G., Zhang, T. L., Taylor, F. W., Lellouch, E., Koschny, D., Witasse, O., Eggel, H., Warhaut, M., Accomazzo, A., Rodriguez-Canabal, J., Fabrega, J., Schirrmann, T., Clochet, A., Coradini, M., 2007, Venus Express – The first European mission to Venus, *Planet. Space Sci.*, 55, 1636–1652
- Tanaka, T., 1993, Configurations of the solar wind flow and magnetic field around the planets with no magnetic field: Calculation by a new MHD simulation scheme, *J. Geophys. Res.*, 98, 17 251–17 262
- Tanaka, T., Murawski, K., 1997, Three-dimensional MHD simulation of the solar wind interaction with the ionosphere of Venus: Results of two-component reacting plasma simulation, *J. Geophys. Res.*, 102, 19 805–19 822
- Taylor, F. W., 2006, Venus before Venus Express, *Planet. Space Sci.*, 54, 1249–1262
- Terada, N., Machida, S., Shinagawa, H., 2002, Global hybrid simulation of the Kelvin-Helmholtz instability at the Venus ionopause, *J. Geophys. Res. (Space Physics)*, 107, 1471–+
- Terada, N., Shinagawa, H., Machida, S., 2004, Global hybrid model of the solar wind interaction with the Venus ionosphere: ion escape processes, *Advances in Space Research*, 33, 161–166
- Torr, M. R., Torr, D. G., 1985, Ionization frequencies for solar cycle 21 - Revised, *J. Geophys. Res.*, 90, 6675–6678

- Trotignon, J. G., Mazelle, C., Bertucci, C., Acuña, M. H., 2006, Martian shock and magnetic pile-up boundary positions and shapes determined from the Phobos 2 and Mars Global Surveyor data sets, *Planet. Space Sci.*, 54, 357–369
- Verigin, M. I., Gringauz, K. I., Gombosi, T., Breus, T. K., Bezrukikh, V. V., Remizov, A. P., Volkov, G. I., 1978, Plasma near Venus from the Venera 9 and 10 wide-angle analyzer data, *J. Geophys. Res.*, 83, 3721–3728
- Vignes, D., Mazelle, C., Reme, H., Acuña, M. H., Connerney, J. E. P., Lin, R. P., Mitchell, D. L., Cloutier, P., Crider, D. H., Ness, N. F., 2000, The solar wind interaction with Mars: Locations and shapes of the Bow Shock and the magnetic pile-up boundary from the observations of the MAG/ER experiment onboard Mars Global Surveyor, *Geophys. Res. Lett.*, 27, 49–52
- Williams, D. R., 2005, National space science data center. <<http://nssdc.gsfc.nasa.gov/planetary/factsheet/venusfact.html>>
- Wu, C. C., 1992, MHD flow past an obstacle - Large-scale flow in the magnetosheath, *Geophys. Res. Lett.*, 19, 87–90
- Zhang, T.-L., Luhmann, J. G., Russell, C. T., 1990, The solar cycle dependence of the location and shape of the Venus bow shock, *J. Geophys. Res.*, 95, 14961–14967
- Zhang, T. L., Luhmann, J. G., Russell, C. T., 1991, The magnetic barrier at Venus, *J. Geophys. Res.*, 96, 11145–11153
- Zhang, T. L., Russell, C. T., Luhmann, J. G., Spreiter, J. R., Stahara, S. S., 1993, On the spatial range of validity of the gas dynamic model in the magnetosheath of Venus, *Geophys. Res. Lett.*, 20, 751–754
- Zhang, T. L., Khurana, K. K., Russell, C. T., Kivelson, M. G., Nakamura, R., Baumjohann, W., 2004, On the venus bow shock compressibility, *Adv. Space Res.*, 33, 1920–1923
- Zhang, T. L., Baumjohann, W., Delva, M., Auster, H.-U., Balogh, A., Russell, C. T., Barabash, S., Balikhin, M., Berghofer, G., Biernat, H. K., Lammer, H., Lichtenegger, H., Magnes, W., Nakamura, R., Penz, T., Schwingenschuh, K., Vörös, Z., Zambelli, W., Fornacon, K.-H., Glassmeier, K.-H., Richter, I., Carr, C., Kudela, K., Shi, J. K., Zhao, H., Motschmann, U., Lebreton, J.-P., 2006, Magnetic field investigation of the Venus plasma environment: Expected new results from Venus Express, *Planet. Space Sci.*, 54, 1336–1343
- Zhang, T. L., Delva, M., Baumjohann, W., Volwerk, M., Russell, C. T., Barabash, S., Balikhin, M., Pope, S., Glassmeier, K.-H., Kudela, K., Wang, C., Vörös, Z., Zambelli, W., 2008a, Initial Venus Express magnetic field observations of the Venus bow shock location at solar minimum, *Planet. Space Sci.*, 56, 785–789
- Zhang, T. L., Delva, M., Baumjohann, W., Volwerk, M., Russell, C. T., Barabash, S., Balikhin, M., Pope, S., Glassmeier, K.-H., Wang, C., Kudela, K., 2008b, Initial Venus Express magnetic field observations of the magnetic barrier at solar minimum, *Planet. Space Sci.*, 56, 790–795

Acknowledgements

First of all, I would like to thank my three supervisors at the Max Planck Institut für Sonnensystemforschung Dr. Markus Fränz, Dr. Norbert Krupp and Dr. Joachim Woch for guiding me through my PhD project. I very appreciate the wonderful working environment inside the planetary plasma group where I always felt comfortable about collaborating with everybody. Apart from many useful scientific discussions they show a good sense of humor providing an extremely friendly atmosphere. Special thanks to Dr. Markus Fränz for all his patience, valuable discussions and interest for my work. I am very grateful for his great support and efforts throughout my PhD time, for helping me with IDL and Linux problems and for always being in a good temper. Thanks to him I learned a lot about analyzing and processing data as well as programming in IDL.

I also want to thank my supervisor at the Technical University of Braunschweig Prof. Dr. Uwe Motschmann for many useful discussions and for helping me to improve the oral presentation techniques as well as scientific paper writing. Thanks to him I have learned how to perform numerical simulations and to deal with the difficult issues associated with it. The hybrid model was a quite challenging task for me because I was thrown in at the deep end in this respect. I am very thankful that he and my other supervisors trusted me to work on a subject which was completely new for me and thus, giving me the chance to extend my knowledge.

I would like to express my gratitude to my colleagues Dr. Elias Roussos, Dr. Alexander Bößwetter and Dr. Sven Simon for their great efforts and mental support with respect to my simulation work. Thanks to their wonderful assistance and many valuable discussions I have learned a lot about carrying out simulations, interpreting the results and comparing them with in-situ measurements. Without their help I would not have been successful in performing good hybrid simulations.

I would like to thank the Directors of MPS, Prof. Dr. Sami Solanki and Prof. Dr. Ulrich Christensen as well as the International Max Planck Research School (IMPRS) for financing this work and for giving me the great opportunity to work in an exciting scientific environment. Special thanks deserves Dr. Dieter Schmitt, the coordinator of the IMPRS, for his support and great efforts in organizing all the seminars and retreats which contributed to the broadening of our knowledge. Many thanks also to Sybilla Siebert-Rust and Claudia Rudolph for all their cordiality, kindness and for helping me with my non-scientific matters making my life in Lindau easier.

I am also very thankful to Prof. em. Dr. Reinhart Leitinger for supporting me during my undergraduate studies and supervising my diploma thesis at the Karl-Franzens Universität in Graz. Thank you for inspiring me and believing in me. Furthermore, I am very grateful to Prof. em. Dr. Gerd Hartmann who has encouraged me to apply for the IMPRS and has been incredibly supportive and helpful throughout my PhD.

I would like to thank my colleagues Dr. Elena Kronberg and Dr. Aikaterini Radioti for sharing the office in my first year, giving me a warm welcome and for many cheerful moments. Thank you so much for your affectionate friendships! Special thanks to Sofie Spjuth and Aline de Lucas who became very good friends during my time in Lindau. I really appreciate your cordial and honest friendships.

Most of all, I want to express my special thanks to my whole family for all their great support, encouragement, patience, understanding and love. I am very proud of my parents, Helmut and Gerti, as well as my brother Tomi, who are always there for me and supporting me in all my decisions. Thank you so much for everything!

I am very thankful to Sabine, Anita, Shahin, Stefan and Martin for their amazing friendships which have not changed or weakened over the 1000 km distance between us. To move away and leave behind family and friends was truly not an easy decision for me but all of them supported me in every step I have made. To tell the truth, without you all I would not have come so far in order to achieve my aims and dreams. I also want to thank Bobby for his friendship, help and good advices in order to find a job after my PhD. Very special recognition deserves Sabine who is like a rock for me! Thank you for always supporting me, sharing good and bad times with me and for all the great moments we have shared. Thank you so much for this awesome and unique friendship which means a lot to me!

Finally, I am deeply grateful to Florian for heartening me whenever needed, especially in the final stage of my PhD. Thank you for all your love, patience and encouragement. I feel very confident that our future will be wonderful!

Curriculum Vitae

Persönliche Daten

Name: Cornelia Martinecz
Geburtsdatum: 6. April 1981
Geburtsort: Bad Radkersburg, Österreich
Staatsangehörigkeit: Österreich

Schulausbildung

1987 – 1991: Volksschule Bad Radkersburg, Österreich
1991 – 1995: Hauptschule Bad Radkersburg, Österreich
1995 – 1999: Bundesoberstufenrealgymnasium Bad Radkersburg, Österreich

Studium

01.10.1999: Beginn des Meteorologie- und Geophysikstudiums an der Karl-Franzens-Universität Graz
19.02.2002: 1.Diplomprüfung in Meteorologie und Geophysik an der Karl-Franzens-Universität Graz
19.05.2004: 2.Diplomprüfung in Geophysik an der Karl-Franzens-Universität Graz zur Erlangung des akad. Grades **Magistra rer. nat.** Titel der Diplomarbeit: *A mapping procedure for the F2 layer peak height*
2004 – 2005: Doktoratstudium Physik (Vorstudien), im Fachbereich Geophysik am Institut für Physik der Karl-Franzens-Universität Graz
2006 – 2008: Doktoratstudium Physik an der 'International Max Planck Research School' (IMPRS) in Katlenburg-Lindau und Technischen Universität von Braunschweig.

Wissenschaftliche Veröffentlichungen allgemeiner Art

Publikationen

C. Martinecz and R. Leitinger, Improved maps for the peak of the ionosphere October 18-22 2004: Proceedings of the Beacon Satellite Symposium 2004, Abdus Salam ICTP Trieste, Italy.

E. Roussos, M. Fränz, E. Dubinin, **C. Martinecz**, J. Woch, U. Motschmann, D. J. Win-ningham, R. Frahm, S. Barabash, and R. Lundin, 2008, Energetic electron asymmetries in the Martian magnetosphere: ASPERA-3 observations, *Planet. Space Sci.*, 56, 836-839

Tagungsbeiträge

C. Martinecz and R. Leitinger, Improved maps for the F2 peak of the ionosphere, 24th Course of the International School of Geophysics: 'Ionospheric Physics and Applications: present and future', Erice, Italy, September 24-29, 2004. (Vortrag).

C. Martinecz and R. Leitinger, Improved maps for the F2 peak of the ionosphere, Beacon Satellite Symposium, Abdus Salam ICTP, Trieste, Italy, October 18-22, 2004. (Poster).

C. Martinecz and R. Leitinger, Improved maps for the electron density and height of the F2 peak of the ionosphere, 65th annual meeting of the 'Deutschen Geophysikalischen Gesellschaft', Graz, Austria, February 20-25, 2005. (Poster).

C. Martinecz and R. Leitinger, Improving maps for the peak of the F2 layer, General As-sembly of the European Geosciences Union, Vienna, Austria, April 24-29, 2005. (Poster).